Masterarbeit

Analytical and numerical calculation of $t\bar{t}\gamma$ and $t\bar{t}Z$ cross-sections with anomalous couplings

von
Klaus Klopfer

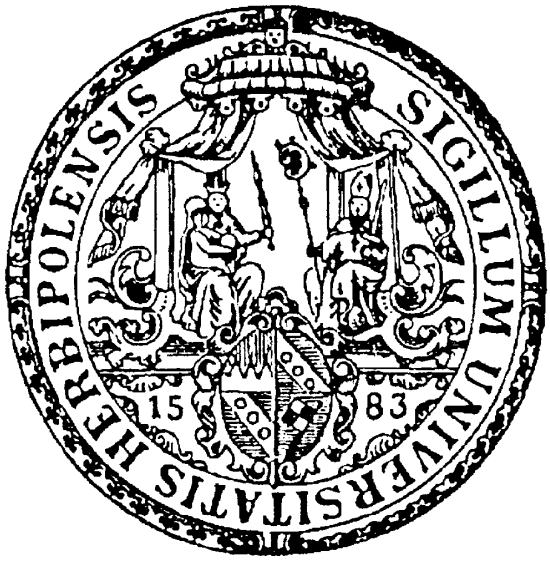

vorgelegt am
13. Oktober 2010
bei
Prof. Dr. Thorsten Ohl

Institut für Theoretische Physik II
Universität Würzburg

Kurzzusammenfassung

In dieser Masterarbeit wird der γtt und Ztt Vertex einschließlich anomaler Kopplungen, hervorgerufen durch eichinvariante Dimension-6 Operatoren, in den Prozessen $GG \to t\bar{t}\gamma$ und $GG \to t\bar{t}Z$ untersucht. Zwei wesentliche Ziele werden in dieser Arbeit verfolgt: Zum einen wird die Frage untersucht, welchen Einfluss die anomalen Kopplungen auf den Wirkungsquerschnitt haben und ob durch Messungen auf die unbekannten Kopplungsparameter zurückgeschlossen werden kann. Zum anderen werden die Ergebnisse der semi-analytischen Rechnung mit denen des `WHIZARD` Programmpaketes verglichen.

Für die semi-analytische Rechnung wird zunächst die Phasenraumintegration für Endzustände mit drei Teilchen besprochen. Die für die numerische Integration problematische Struktur der Propagatorennenner der Feynmanamplituden und die damit verbundene mangelnde Konvergenz des Phasenraumintegrals erfordert den Einsatz von Mehrkanal Monte Carlo Integrationstechniken.

Die Analyse der anomalen Top Quark-Photon Kopplungen zeigt, dass eine Bestimmung dieser Kopplungsparameter durch die Untersuchung des Prozesses $GG \to t\bar{t}\gamma$ bei einer Schwerpunktsenergie von 7 TeV am LHC eine große Herausforderung darstellt. Zwar kann auf Partonlevel eine Strategie formuliert werden, die es erlaubt, durch Messung der Abweichung des totalen Wirkungsquerschnittes mit anomalen Kopplungen von dem des Standardmodells bei verschiedenen Schwerpunktsenergien die Kopplungen zu bestimmen. Jedoch ist die festgestellte Abweichung zu klein, als dass sie nach der Faltung mit den PDFs noch feststellbar wäre. Weitere Untersuchungen von differentiellen Wirkungsquerschnitten, mit dem Ziel geeignetere Observablen zu finden, sind folglich wünschenswert.
Für den Ztt Vertex ist die Situation aussichtsreicher. Es werden zwei unabhängige Methoden vorgestellt, mit denen grundsätzlich zwei der vier anomalen Top Quark-Z-Boson Kopplungen ermittelt werden können. Einschränkend muss jedoch angemerkt werden, dass die zu erwartende experimentelle Unsicherheit bestenfalls die Angabe von recht hohen oberen Schranken für die Parameter erwarten lässt.

Der Vergleich der semi-analytischen Rechnung mit `WHIZARD` zeigt gute Übereinstimmung der Ergebnisse für den Wirkungsquerschnitt. Diese weichen maximal um wenige Standardabweichungen voneinander ab. Eine genaue quantitative Analyse offenbart leichte Konvergenzprobleme der semi-analytischen Rechnung, weshalb bei einem Vergleich der Mittelwerte von Stichproben mit häufig wiederholter Berechnung mit denselben Parametern eine signifikante Abweichung feststellbar ist. Überdies zeigt sich, dass der Fehler der numerischen Integration von `WHIZARD` leicht unterschätzt wird.

Contents

1 Introduction

The Large Hadron Collider (LHC) circulated its first beams after the maintenance and repair period on 20 November 2009 [1]. Three days later the first proton-proton collision was reported at a center-of-mass energy of $\sqrt{s} = 900$ GeV [2]. After the winter shutdown, the beam energy was gradually increased, until on 19 March 2010 the CERN (European Organization for Nuclear Research) Press Office announced an alltime record with a center-of-mass energy of $\sqrt{s} = 7$ TeV [3]. It is planned to run at this beam energy continuously, except for a short technical stop at the end of 2010, until the shutdown in 2012, which is forseen to further upgrade the accelerator.

With a circumference of 27 km and a center-of-mass energy up to 14 TeV the LHC is the largest and highest energetic particle collider world-wide. Its luminosity is designed to be 10^{34} cm^{-2}s^{-1}. The high luminosity and most of all the high center-of-mass energy open up completely new perspectives in the field of particle physics. Among the primary goals of the LHC experiments are the search for the Higgs boson, the exploration of new physics beyond the Standard Model (SM) at the scale of TeV, such as supersymmetry signals, as well as the investigation of the origin of the electroweak symmetry breaking (EWSB) [4–6]. The study of the top quark, being the heaviest fundamental fermion known, plays a central role in all of these goals:

- High-precision measurements of top quark properties significantly facilitate the search for the Higgs boson. Firstly, the top quark is involved in two possible production channels of the Higgs boson. The gluon-gluon fusion channel comes with a top quark loop, in the second channel the Higgs boson is produced via associated production (see figure 1.1(a)). Since both channels require high energetic gluons in the final state, a precise knowledge of the gluon distribution function at high energies is desired. As will be stated later on, the main channel for top-antitop quark pair production involves high energetic gluons as well. The precise measurement of the top-antitop quark pair production cross-section allows to draw a conclusion on the gluon distribution functions and thus constrains the prediction of these two Higgs production channels. Secondly, one can derive correlations between the mass of the W-boson, the mass of the top quark and the mass of the Higgs boson due to virtual loop corrections. Figure 1.1(b) illustrates the prediction of the mass of the Higgs boson based on current experimental estimates.
- As numerous particles originating from new physics are expected to decay into top quarks, high advanced techniques of the reconstruction of top quark events are inevitable. Furthermore, SM top quark events will be the dominant background for these processes.
- Moreover, the top quark being the only known fundamental fermion with a mass on the electroweak scale, its study may provide a very good probe of the sector of the EWSB [4, 5].

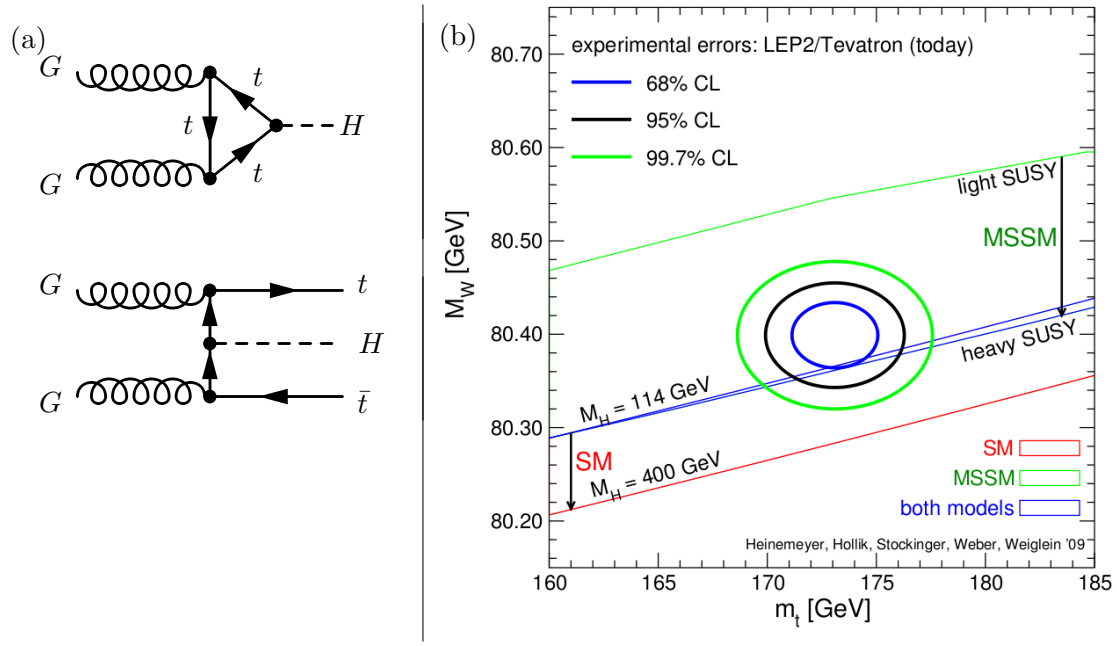

Figure 1.1: (a) Feynman graphs for the Higgs production processes involving top quarks to leading order. (b) Prediction of the Higgs boson mass M_H based on current experimental estimates of the top quark mass m_t and of the mass of the W-boson M_W. The concentrical ellipses indicate the region in the m_t-M_W-plane where both masses are expected to be found at different confidence levels (CL). Along the sloping lines a m_t-M_W-pair results in the same value for the Higgs boson mass. E. g. a Higgs boson with a mass below 114 GeV is excluded at a CL of 68%.

The precise knowledge of the interactions of the top quark with the gauge bosons is compulsory in order to accomplish the above mentioned studies. Any deviation from the Standard Model expectations is either an indication of an anomaly in the SM or of new physics on a higher energy scale. While considerable effort has already been made on the determination of the Wtb interaction [7–9], the Gtt, Ztt and γtt couplings have been rarely considered [10–12].

Particle physics analyzes usually require the use of Monte Carlo event generators. Particularly in the early stage of the LHC Monte Carlo studies are inevitable for a full understanding of the detector components [5]. Moreover, the phenomenology of modified theoretical physics models can be investigated with simulated events. In this way, the question how new model parameters, such as anomalous couplings, could be measured is addressed inter alia. Among the principal general-purpose Monte Carlo generators employed in LHC studies are `PYTHIA` [13] and `HERWIG` [14]. These tools provide the generation of events for processes of the SM and several models beyond the SM making use of hard-coded libraries of leading order on-shell matrix elements. The hard-coding makes them somewhat impractical in view of the large number of proposed new-physics models. Furthermore, the above mentioned programs are rather limited regarding multi-particle elementary processes and the handling of off-shell amplitudes. Hence, in the last few years considerable effort has been made to develop automated general-purpose event generators, such as `MadGraph/MadEvent` [15], `CompHEP/CalcHEP` [16, 17] and `Sherpa` [18]. Following a similar approach, the new event generation package `WHIZARD` [19] comes with the necessary techniques to deal with the problems mentioned before in a fully automated way. Thus, it

may be considered as a worthy competitor in the family of Monte Carlo event generators for hadron colliders like the LHC and, additionally, for future linear colliders, such as the International Linear Collider (ILC).

The major aim of this thesis is twofold: On the one hand, the general γtt and Ztt vertices including anomalous top quark interactions generated by dimension-six gauge-invariant effective operators (see section 3.3) are analyzed. The possibility of determining the involved anomalous coupling parameters is discussed for the process $GG \to t\bar{t}$ with additional photon or Z boson radiation, respectively. On the other hand, the results obtained by semi-analytical calculations are compared to the ones produced by `WHIZARD`.

This document is structured as follows: The next chapter introduces some experimental aspects of top quark physics, such as top quark production and decay. Chapter 3 then outlines the theoretical framework of top quark physics putting special emphasis on top quark anomalous couplings in section 3.3. After that, the `WHIZARD` program package is presented in chapter 4. Having discussed the procedure of calculating total reaction cross-sections in chapter 5, the subsequent chapter 6 deals with the three particle phase space. The general γtt and Ztt vertices are finally analyzed in chapters 7 and 8, respectively. The rather qualitative comparison of the results of the semi-analytical calculation with `WHIZARD` therein is eventually supplemented with a more quantitative one in chapter 9 before coming to a conclusion in chapter 10.

2 The top quark

This chapter deals with experimental aspects of top quark physics. In the first section properties of the top quark, that is its mass, charge, spin and lifetime, as known from measurements are described briefly. Subsequently, the top quark production (section 2.2) and decay (section 2.3) are discussed. Finally, potential ways of determining the top quark pair production cross-section is presented in section 2.4.

2.1 Top quark properties

The top quark was discovered at Fermilab in 1995 [20, 21]. It is the heaviest quark known with a mass of $(172.0 \pm 0.9(\text{statistics}) \pm 1.3(\text{systematics}))$ GeV [22], which is comparable to the mass of the atomic nucleus of gold. It is hoped to determine the top quark mass with an accuracy of about 1 GeV combining results of the two general purpose particle detectors of LHC, the ATLAS and the CMS detector [23].

In the SM the top quark has electric charge +2/3 e. However, some exotic models [24] predict a different type of quark in this mass range with electric charge -4/3 e. In order to reconstruct the top quark charge in the semi-leptonic top quark pair channel one has to, firstly, find the correct pairing of the bottom quark and the charged lepton originating from the same top quark, secondly, reconstruct the bottom quark charge and, thirdly, determine the charge of the involved lepton. Recent Tevatron measurements [25, 26] strongly favor the 2/3 charged top quark of the SM at confidence levels above 90%.

Though not yet verified directly, measurements at Tevatron strongly indicate a spin-1/2 top quark [27], compatible with the SM. Since the spin of the decay products is known, the conservation of total momentum allows to draw the conclusion that the top quark is a fermion. A half-integral spin value of 3/2 or larger is excluded because the measured top quark pair production cross-section at Tevatron is not compatible with this assumption. The direct determination of the top quark spin is foreseen at LHC experiments making use of polarization and spin correlation effects [4, 6].

2.2 Top quark production

In principal there are two mechanisms of producing a top quark: The production of top-antitop quark pairs via strong interaction is presented in the following subsection, the electroweak single top quark production in subsection 2.2.2.

2.2.1 Top quark pair production

Top-antitop quark pairs can be produced via two different reactions: The gluon-gluon fusion contributes the main part (~ 90 %) of the top quark pair production at the center-of-mass energies reached at the LHC. The Feynman graphs to leading order are shown in figure 2.1. In the s-channel (diagram **A**) two initial state gluons merge to a virtual gluon, in the t- and u-channel (diagram **B** and **C**, respectively) they exchange a top quark. The quark-antiquark annihilation (diagram **D**), which dominates at Tevatron, only accounts for approximately 10% of the total production at the LHC.

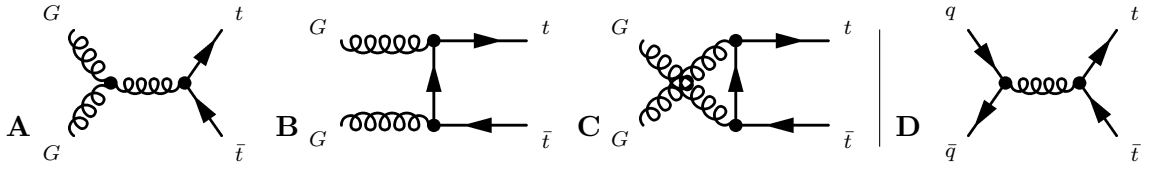

Figure 2.1: Feynman graphs to leading order contributing to the top quark pair production at hadron colliders. The diagrams involved in the gluon-gluon fusion are shown on the left (**A**-**C**), whereas the diagram on the right (**D**) refers to the quark-antiquark annihilation.

The LHC is often called a top quark factory because of its immense top quark production. The cross-section of the top-antitop quark pair production is predicted to be $\sigma(t\bar{t}) = (833 \pm 100)$ pb by the next-to-leading order (NLO) calculation including NLL soft gluon resumation at a center-of-mass energy of $\sqrt{s} = 14$ TeV [28]. This is approximately 100 times as large as the value of Tevatron. The reason for that is mainly the higher center-of-mass energy at the LHC. Already at low luminosity in the early years of the LHC millions of $t\bar{t}$ pairs will thus be produced.

2.2.2 Single top quark production

Single top quarks are generated in electroweak processes, in which the top quark couples with a W-boson and a b-quark. In leading order (LO) a categorization into three different mechanisms is possible [4, 23]: The t-channel processes, $qG \to q' + t\bar{b}$ and $qb \to q't$, have the largest contribution of approximately 76% at the LHC. The Wt-associated production, $Gb \to Wt$, accounts for about 20%, whereas the s-channel, $q\bar{q}' \to W \to t\bar{b}$ only contributes about 3% of the total single top quark production at the LHC. In spite of the small cross-section of the s-channel graph, this is still an particularly interesting channel because it is directly sensitive to additional heavy W' bosons, which would lead to further s-channel diagrams. In general the analysis of single top quark events is of special interest because their cross-sections are proportional to the square of the CKM matrix element $|V_{tb}|$. Hence no assumptions neither on the number of generations in the SM (see also section 3.1) nor on the unitarity are needed to determine $|V_{tb}|$ [22].

2.3 Top quark decay

Referring to the SM the lifetime of the top quark is only $\sim 10^{-25}$ s because of its huge mass. As this is about one magnitude shorter than the timescale for strong interactions, the top quark decays as a "bare quark" without hadronization. The dominant decay channel is $t \to Wb$ (branching ratio $0.99^{+0.09}_{-0.08}$ [22]). The W-boson itself can either decay hadronically

($W \rightarrow q\bar{q}$, branching ratio $\approx 68\%$) or leptonically ($W \rightarrow e\bar{\nu}_e$, $W \rightarrow \mu\bar{\nu}_\mu$ or $W \rightarrow \tau\bar{\nu}_\tau$, branching ratio each $\approx 11\%$) [22]. Therefore there are three decay channels of top-antitop quark pairs [5]:

- *Fully hadronic*: Both W-bosons decay hadronically ($t\bar{t} \rightarrow qq\bar{q}\bar{q}b\bar{b}$). Two jets from b-quark and four light jets, which arise from the two W-bosons, are generated. However, there is a lot of background from QCD events with similar signature as well as combinatorial background, which makes the analysis of this decay channel very challenging. The fully hadronic decays amount to about 46% of the $t\bar{t}$ decays.
- *Semi-leptonic*: One of the W-bosons decays hadronically and one into a lepton-neutrino pair ($t\bar{t} \rightarrow l\nu q\bar{q}b\bar{b}$). This channel is often called the "golden channel" because of its characteristic signature: The high energetic and isolated lepton can be used both to trigger the event and to select the event by defining efficient cuts to suppress the background. Moreover, if *b-tagging* abilities are available to distinguish between the b-jets and the light jets from the W-boson decay, the combinatorial background may be reduced significantly as well. About 44% of the $t\bar{t}$ events are represented by the semi-leptonic channel. The background is discussed beneath.
- *Fully leptonic*: Both W-bosons decay leptonically ($t\bar{t} \rightarrow ll\nu\nu b\bar{b}$). As there are two neutrinos in the final state, the possibility of reconstructing this event is limited. The fully leptonic channel totals up to about 10% of the $t\bar{t}$ decays.

The background of the semi-leptonic channel is dominated by QCD multi-jet events if at least one of the jets is misidentified as an isolated lepton [5]. The remaining background mostly arises from W-boson+jets and Z-boson+jets events. *B-tagging* could efficiently suppress the greater part of these events. However, in the early years of the LHC *b-tagging*-abilities will not be available. Finally, the background coming from fully hadronic and fully leptonic events should be mentioned.

2.4 Determination of top quark pair production cross-section

As lots of $t\bar{t}$ events are expected to be produced at the LHC, the measurement of the top quark pair production cross-section will be accomplished with the first data samples available. In this section two complementary prospects for measuring the total $t\bar{t}$ cross-section [5], which are most promising in the early stage of the LHC, are presented. Although these methods address the determination of the cross-section in the semi-leptonic channel for $t\bar{t}$ events, the general approach is similar for related events.

Likelihood fit method

In the likelihood fit method the invariant mass of the three jets of the hadronically decaying top quark, denoted as three-jet invariant mass M_{jjj}, is considered. Firstly, the three-jet invariant mass distribution is determined by calculating M_{jjj} for all events that pass the selection criteria. For the event selection criteria is referred to Ref. [5]. The number of signal as well as background events is then determined by a maximum likelihood fit with a Gaussian signal on top of the background modeled by a Chebychev polynomial (see figure 2.2). Eventually, the cross-section can be estimated from the ratio of signal to background events taking into account the event selection efficiency and the hadronic

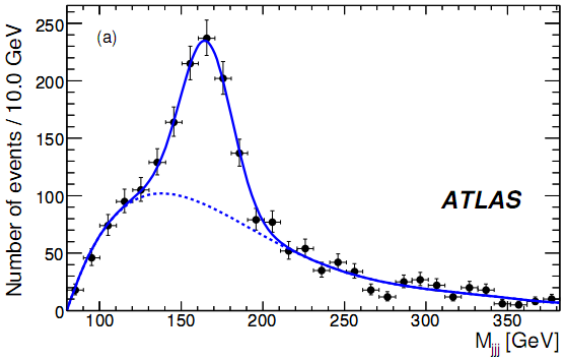

Figure 2.2: Distribution of the three-jet invariant mass M_{jjj} (Monte Carlo simulation). The background is modeled by a Chebychev polynomial (dotted line), the signal events by a Gaussian on top of it (full line). [5]

top reconstruction efficiency. Whereas the likelihood fit method is rather insensitive to background normalization and efficiencies, the shape of the three-jet invariant mass has to be fairly well understood.

Counting method

If the background events of the process are well known, the cross-section σ can be calculated using the equation:

$$\sigma = \frac{N_{\text{obs}} - N_{\text{bg}}}{\mathcal{L} \cdot \varepsilon} = \frac{N_{\text{sig}}}{\mathcal{L} \cdot \varepsilon} \tag{2.1}$$

Herein $\mathcal{L}$ denotes the integrated luminosity, N_{obs} the number of observed events passed the selection cuts of $t\bar{t}$ events, N_{bg} the number of background events estimated from Monte Carlo or data samples. The difference $N_{\text{obs}} - N_{\text{bg}}$ is the number of events of the actual signal N_{sig}. The total efficiency ε includes the geometrical acceptance, the trigger efficiency and the event selection efficiency. Therefore it can be expressed as $\varepsilon = \varepsilon_{\text{trig}}\ \varepsilon_{\text{sel}}$, the product of the trigger efficiency and the event selection efficiency. One of the biggest uncertainties of this method is the required precise understanding of all backgrounds and their normalization. On the other hand, it does not rely on the knowledge of the top mass distribution nor is it dependent on the reconstruction of parts of the $t\bar{t}$ event.

3 Theoretical framework of top quark physics

3.1 The top quark in the Standard Model

The Standard Model of particle physics (SM) is the theory of the fundamental dynamics of elementary particles in the framework of a relativistic quantum field theory. The interactions are described by a SU(3)×SU(2)×U(1) gauge theory, where the SU(3) component refers to the strong interaction, detailed in the theory of quantum chromodynamics (QCD), and the SU(2)×U(1) part to the electroweak interactions. The corresponding conserved quantum numbers are color charge, weak isospin I_{W} and weak hypercharge Y_{W}, respectively. The latter ones are related to electric charge Q by

$$Q = T_3 + Y_{\mathrm{W}}, \tag{3.1}$$

where T_3 is the third component of weak isospin. The fundamental fermionic constituents of the SM are quarks and leptons. Being spin-1/2 particles, they respect the Fermi-Dirac statistics. Each particle has a corresponding antiparticle. One distinguishes up-type quarks with electric charge +2/3 and down-type quarks with electric charge -1/3. The leptons have either electric charge -1 (electron-like) or 0 (neutrinos). Whereas quarks are color charged SU(3) triplets and thus participate in the strong interaction, leptons are SU(3) singlets and do not interact via the strong interaction. Left-handed fermion fields transform as doublets under SU(2), right-handed fields are SU(2) singlets. One set of up- and down-type quark together with one pair of leptons are grouped together to form a generation, of which three redundant copies exist in the SM, the only difference being the greater mass in higher generations. The properties of the left-handed fermions of the SM are summarized in table 3.1. The top quark being an up-type quark, has electric charge +2/3 and +1/6 weak hypercharge. It is the member of the weak isospin doublet containing the bottom quark with $T_3 = +1/2$.

Besides of the fermions, the SM includes spin-1 gauge bosons, which act as force mediating particles. There are eight massless gluons mediating the strong interaction. The Z- and W^+/W^--boson are the mediators of the weak interaction and are massive. Whereas the Z-boson carries no electric charge and couples to left- and right-handed particles and antiparticles, the $W^{\pm}$-bosons have electric charge ± 1, respectively, and only interact with left-handed particles or right-handed antiparticles. Finally, the mediator of the electromagnetic force is the massless photon A, sometimes also denoted by the symbol γ. As will shortly be pointed out in the next paragraph, the $W^{\pm}/Z$-bosons do not represent the originally degrees of freedom of the SU(2)×U(1) gauge group. Table 3.2 lists the properties of the bosons contained in the SM.

Moreover, the SM contains one spin-0 boson, the Higgs boson, which plays a unique role. In the minimal model there is a single complex Higgs doublet ϕ. The Higgs field acquiring

Name (symbol)	Electric charge	Weak isospin	Weak hypercharge
leptons (l)			
electron (e^-) muon (μ^-) tau (τ^-)	-1	$-\frac{1}{2}$	$-\frac{1}{2}$
positron (e^+) anti-muon (μ^+) anti-tau (τ^+)	$+1$	0	$+1$
electron neutrino (ν_e) muon neutrino (ν_μ) tau neutrino (ν_τ)	0	$+\frac{1}{2}$	$-\frac{1}{2}$
quarks (q)			
up quark (u) charm quark (c) top quark (t)	$+\frac{2}{3}$	$+\frac{1}{2}$	$+\frac{1}{6}$
up antiquark ($\bar{u}$) charm antiquark ($\bar{c}$) top antiquark ($\bar{t}$)	$-\frac{2}{3}$	0	$-\frac{2}{3}$
down quark (d) strange quark (s) bottom quark (b)	$-\frac{1}{3}$	$-\frac{1}{2}$	$+\frac{1}{6}$
down antiquark ($\bar{d}$) strange antiquark ($\bar{s}$) bottom antiquark ($\bar{b}$)	$+\frac{1}{3}$	0	$+\frac{1}{3}$

Table 3.1: Quantum numbers of the left-handed fermions of the SM.

boson		interaction	spin	mass (GeV)
photon	γ	electromagnetic	1	0
Z-boson	Z	weak	1	91.1876 ± 0.0021
$W^\pm$-boson	$W^\pm$	weak	1	80.399 ± 0.023
gluon	G	strong	1	0
Higgs-boson	H		0	>114.4

Table 3.2: Properties of the bosons of the SM. The values for the masses are adopted from Ref. [22].

a non-vanishing vacuum expectation value

$$\langle \phi \rangle = \frac{1}{\sqrt{2}} \begin{pmatrix} 0 \\ v \end{pmatrix} \tag{3.2}$$

with $v = 246$ GeV, the electroweak SU(2)×U(1) symmetry is spontaneously broken down to the U(1) symmetry of electromagnetism. As a result, three massless Goldstone bosons are created, which are integrated in three of the gauge fields of the electroweak sector through the Higgs mechanism. The upshot is that these fields become the *massive* $W^{\pm}/Z$-bosons of the weak interaction, while the photon A stays massless. In terms of the original *massless* gauge fields of the unbroken SU(2)×U(1) symmetry, W^1, W^2, W^3 and B, the boson fields after spontaneous symmetry breaking are defined as

$$A \equiv B \cos\theta_{\mathrm{W}} + W^3 \sin\theta_{\mathrm{W}} \tag{3.3}$$

$$Z \equiv -B \sin\theta_{\mathrm{W}} + W^3 \cos\theta_{\mathrm{W}} \tag{3.4}$$

$$W^{\pm} \equiv \frac{1}{\sqrt{2}} \left(W^1 \mp \mathrm{i} W^2 \right), \tag{3.5}$$

with θ_{W} being the weak mixing angle. Additionally, the coupling of the Higgs field to fermions, the so-called Yukawa coupling, also gives rise to the masses of the fermions. The masses of the fermions are thus proportional to the Yukawa coupling strength.

After electroweak symmetry breaking the Lagrangian of the electroweak section for the fermion fields reads [22]

$$\begin{aligned} \mathcal{L}_{\mathrm{fermion}} = & \sum_i \overline{\psi}_i \left(\mathrm{i}\, \partial\!\!\!/ - m_i - \frac{g\, m_i H}{2 M_W} \right) \psi_i \\ & - \frac{g}{2\sqrt{2}} \sum_i \overline{\psi}_i\, \gamma^\mu \left(1 - \gamma^5\right) \left(T^+ W_\mu^+ + T^- W_\mu^- \right) \psi_i \\ & - e \sum_i q_i \overline{\psi}_i \gamma^\mu \psi_i A_\mu \\ & - \frac{g}{2\cos\theta_{\mathrm{W}}} \sum_i \overline{\psi}_i \gamma^\mu \left(g_{\mathrm{V}}^i - g_{\mathrm{A}}^i \gamma^5 \right) \psi_i Z_\mu, \end{aligned} \tag{3.6}$$

with the weak mixing angle $\theta_{\mathrm{W}} \equiv \arctan(g'/g)$ and the positron electric charge $e = g \sin\theta_{\mathrm{W}}$. g and g' are the gauge coupling constants of the SU(2) and U(1) group, respectively. The sum over i runs over all fermions. Moreover, T^+ and T^- refer to the weak isospin raising and lowering operators. The last term in (3.6) includes the vector and axial-vector couplings

$$g_{\mathrm{V}}^i \equiv T_{i\,3} - 2 q_i \left(\sin\theta_{\mathrm{W}} \right)^2, \tag{3.7a}$$

$$g_{\mathrm{A}}^i \equiv T_{i\,3}. \tag{3.7b}$$

The Lagrangian of the QCD part is [22]

$$\mathcal{L}_{\mathrm{QCD}} = \sum_q \overline{\psi}_{q,a} \left(\mathrm{i} \gamma^\mu \partial_\mu \delta_{ab} - g_s \gamma^\mu t_{ab}^C G_\mu^C - m_q \delta_{ab} \right) \psi_{q,b} - \frac{1}{4} G_{\mu\nu}^A G^{A\,\mu\nu}, \tag{3.8}$$

with the strong coupling constant g_s and the quark masses m_q, the index q being the quark flavor. The quark field spinors $\psi_{q,a}$ carry an additional color index a, running over

the three colors. The sum over repeated indices is understood. The t^C_{ab} are the generators of the SU(3) group. Eventually, the field tensor $G^A_{\mu\nu}$ reads

$$G^A_{\mu\nu} = \partial_\mu G^A_\nu - \partial_\nu G^A_\mu - g_s f^{ABC} G^B_\mu G^C_\nu, \tag{3.9a}$$

$$\text{with} \quad \left[t^A, t^B\right] = \mathrm{i} f^{ABC}\, t^C, \tag{3.9b}$$

where G^C_μ refer to the gluon fields, with C running from 1 to 8 over all kinds of gluons, and f^{ABC} correspond to the structure constants of the SU(3) group.

3.2 Dependence of the coupling constant on the energy scale

Demanding that physical results must be independent of the chosen renormalization scale μ, a differential equation, the so-called renormalization group equation,

$$\mu^2 \frac{\mathrm{d}g(\mu)}{\mathrm{d}\mu^2} = \beta\, g(\mu)^2 \tag{3.10}$$

is obtained. Its solution describes the dependence of the coupling constant g on μ:

$$g(\mu) = \frac{g(\mu_0)}{1 + g(\mu_0)\beta \ln \frac{\mu_0^2}{\mu^2}} \tag{3.11}$$

Herein $g(\mu_0)$ is the given coupling constant at a scale μ_0. The behavior of the coupling thus depends on the sign of the β-function: If β is positive (like e. g. in QED), the coupling is weak at low energy scales but strong at high scales. However, in QCD having $\beta < 0$, the coupling strength is weak in the ultraviolet and becomes strong in the infrared. Consequently, particles participating in the strong interaction may be considered as non-interacting particles at a high energy scale. Such behavior is referred to as *asymptotic freedom*. On the other hand, the coupling becomes strong for long distances.

3.3 Top quark anomalous couplings

As motivated in chapter 1, high-precision measurements of the interactions of the top quark with the gauge bosons may provide hints on physics beyond the SM. Such analyzes require an adequate parameterization of the most general top quark couplings. Emphasis should particularly be put on the avoidance of redundant parameters, as these would lead to an unnecessary complication of the analysis. The aim of this section is to sketch the procedure of obtaining most general expressions for top quark vertices without redundant coupling parameters.

Effects that arise from interactions of new physics at a high scale Λ can be described by a low energy effective Lagrangian as an expansion in $1/\Lambda$ [29]

$$\mathcal{L}_{\text{eff}} = \sum_{n=0}^{\infty} \frac{1}{\Lambda^n} \mathcal{L}_n = \mathcal{L}_0 + \frac{1}{\Lambda}\mathcal{L}_1 + \frac{1}{\Lambda^2}\mathcal{L}_2 + \ldots, \tag{3.12}$$

where $\mathcal{L}_0$ denotes the standard Lagrangian unaffected by high energy contributions. The Lagrangians $\mathcal{L}_n$ contain operators of dimension $(4+n)$ and are composed of only low-energy fields. As the higher order terms are suppressed by powers of Λ, it is sufficient to consider only a small number of these. Assuming that the SM describes physics well in the energy range below Λ, all $\mathcal{L}_n$ must respect the symmetries and conservation laws of the SM, that is, in particular, they are SU(3)×SU(2)×U(1) invariant. If one further imposes conservation of baryon and lepton number as in the SM, no dimension-five operator can be constructed [29]. Furthermore, neglecting terms of order $1/\Lambda^3$ and higher, we are left with the effective Lagrangian

$$\mathcal{L}_{\text{eff}} = \mathcal{L}_0 + \frac{1}{\Lambda^2}\mathcal{L}_2. \tag{3.13}$$

Hence, the problem of finding the most general but non-redundant expression for the top quark couplings has reduced to, firstly, writing down all dimension-six gauge-invariant operators and, secondly, removing all the redundant ones. A list of all these operators can be found in Ref. [29], where some of the operators related by the equation of motion are already skipped. In fact, gauge symmetry is the fundamental principle to further remove excessive terms. As was shown [30–32], in the end only those terms that would also be present in an on-shell interaction remain, provided that all new couplings arise from dimension-six gauge-invariant operators. In other words, the interaction between two off-shell fermions and an off-shell gauge boson can be parameterized in full generality by an effective Lagrangian with all involved particles being on-shell. In order to clarify this phenomenon, which might seem somewhat curious, the basic idea of constructing this on-shell effective Lagrangian is outlined in the following. For this purpose, consider an effective Lagrangian involving a scalar Klein-Gordon field ϕ with mass m_ϕ, a Dirac field ψ and its conjugate $\overline{\psi}$. In particular, look at the terms with ∂^2 acting on the ϕ field, which in n^{th} order take the form

$$\epsilon^n f(\psi,\phi)\partial^2\phi. \tag{3.14}$$

Herein ϵ is a small parameter, such as the couplings, and $f(\psi,\phi)$ some function of the fields ψ, ϕ and derivatives. Performing a non-linear redefinition of the ϕ field

$$\phi \to \phi' = \phi + \Delta\phi \tag{3.15a}$$
$$\Delta\phi = -\epsilon^n f(\psi,\phi) \tag{3.15b}$$

such a term can be replaced order by order in ϵ by a term with a $-m_\phi^2$ in favor of the ∂^2 plus additional terms with more ϕ fields and a higher power in ϵ. The way how this works can most easily be seen in the path integral formalism considering the generating functional

$$Z(\eta,\overline{\eta},j) = \frac{\int \mathcal{D}\psi\mathcal{D}\overline{\psi}\mathcal{D}\phi\ \exp\left[\mathrm{i}\,S(\psi,\phi) + \mathrm{i}\int \mathrm{d}^4x\ \left(\overline{\psi}(x)\eta(x) + \overline{\eta}(x)\psi(x) + \phi(x)j(x)\right)\right]}{\int \mathcal{D}\psi\mathcal{D}\overline{\psi}\mathcal{D}\phi\ \exp[\mathrm{i}\,S(\psi,\phi)]} \tag{3.16}$$

with the source fields $j(x)$ and $\eta(x)$, the latter being Grassmann-valued. For example the 3-

point correlation function of the fields $\psi(x_1)\phi(x_2)\overline{\psi}(x_3)$ is then given by

$$\begin{aligned}\left\langle 0\middle|\mathrm{T}\,\psi(x_1)\phi(x_2)\overline{\psi}(x_3)\middle|0\right\rangle &= \lim_{j,\eta,\overline{\eta}\to 0}\frac{\delta}{\mathrm{i}\delta\overline{\eta}(x_1)}\frac{\delta}{\mathrm{i}\delta j(x_2)}\frac{\delta}{\mathrm{i}\delta\eta(x_3)}Z(\eta,\overline{\eta},j)\\ &= \frac{\int\mathcal{D}\psi\mathcal{D}\overline{\psi}\mathcal{D}\phi\ \psi(x_1)\phi(x_2)\overline{\psi}(x_3)\exp[\mathrm{i}\,S(\psi,\phi)]}{\int\mathcal{D}\psi\mathcal{D}\overline{\psi}\mathcal{D}\phi\ \exp[\mathrm{i}\,S(\psi,\phi)]}.\end{aligned} \tag{3.17}$$

Applying the field-redefinition (3.15) the altered generating functional Z' reads

$$\begin{aligned}Z'(\eta,\overline{\eta},j) &= \frac{\int\mathcal{D}\psi\mathcal{D}\overline{\psi}\mathcal{D}\phi'\ \exp\left[\mathrm{i}\,S(\psi,\phi')+\mathrm{i}\int\mathrm{d}^4x\ \left(\overline{\psi}(x)\eta(x)+\overline{\eta}(x)\psi(x)+\phi'(x)j(x)\right)\right]}{\int\mathcal{D}\psi\mathcal{D}\overline{\psi}\mathcal{D}\phi'\ \exp[\mathrm{i}\,S(\psi,\phi')]}\\ &= \frac{\int\mathcal{D}\psi\mathcal{D}\overline{\psi}\mathcal{D}\phi\ \exp\left[\mathrm{i}\,S(\psi,\phi+\Delta\phi)+\mathrm{i}\int\mathrm{d}^4x\ \left(\overline{\psi}(x)\eta(x)+\overline{\eta}(x)\psi(x)+(\phi(x)+\Delta\phi(x))j(x)\right)\right]}{\int\mathcal{D}\psi\mathcal{D}\overline{\psi}\mathcal{D}\phi\ \exp[\mathrm{i}\,S(\psi,\phi+\Delta\phi)]}.\end{aligned} \tag{3.18}$$

Note the change $\mathcal{D}\phi'\to\mathcal{D}\phi$ from the first to the second line in expression (3.18). Naively one might expect the integration measure $\mathcal{D}\phi'$ to be affected by the field-redefinition, too, as the change of variables (3.15) produces a Jacobian

$$D = \det\frac{\delta\phi'(x)}{\delta\phi(y)} = \det\left(\delta(x-y)+\epsilon\frac{\delta\Delta\phi(x)}{\delta\phi(y)}\right). \tag{3.19}$$

However, a more rigorous treatment of the integration measure of generating functionals is necessary. For that reason consider the path integral in the Hamiltonian (canonical) representation. As the transformation (3.15) is canonical, the integration measure of the canonical representation is invariant under this transformation. However, when switching to the Lagrangian representation of the path integral, one collects an additional factor, a functional $g(\phi)$ [33]. This suggests the integration measure of the Lagrangian representation to be rather understood as $\mathcal{D}\phi\cdot g(\phi)$, where $g(\phi)$ is supposed to transform under a change in variables such a way that it cancels the invoked Jacobian (3.19) and the invariance of the integration measure under field redefinition is guaranteed.
Moving the attention back to the expression of Z' in the second line of (3.18), the 3-point function in terms of the new variables is obtained in analogy to (3.17)

$$\begin{aligned}\left\langle 0\middle|\mathrm{T}\,\psi(x_1)\phi'(x_2)\overline{\psi}(x_3)\middle|0\right\rangle &= \lim_{j,\eta,\overline{\eta}\to 0}\frac{\delta}{\mathrm{i}\delta\overline{\eta}(x_1)}\frac{\delta}{\mathrm{i}\delta j(x_2)}\frac{\delta}{\mathrm{i}\delta\eta(x_3)}Z'(\eta,\overline{\eta},j)\\ &= \frac{\int\mathcal{D}\psi\mathcal{D}\overline{\psi}\mathcal{D}\phi\ \psi(x_1)\left(\phi(x_2)+\Delta\phi(x_2)\right)\overline{\psi}(x_3)\exp[\mathrm{i}\,S(\psi,\phi+\Delta\phi)]}{\int\mathcal{D}\psi\mathcal{D}\overline{\psi}\mathcal{D}\phi\ \exp[\mathrm{i}\,S(\psi,\phi+\Delta\phi)]}.\end{aligned} \tag{3.20}$$

Employing the linearity of the integral the expression is transformed into

$$\begin{aligned}\left\langle 0\middle|\mathrm{T}\,\psi(x_1)\phi'(x_2)\overline{\psi}(x_3)\middle|0\right\rangle &= \frac{\int\mathcal{D}\psi\mathcal{D}\overline{\psi}\mathcal{D}\phi\ \psi(x_1)\phi(x_2)\overline{\psi}(x_3)\exp[\mathrm{i}\,S(\psi,\phi+\Delta\phi)]}{\int\mathcal{D}\psi\mathcal{D}\overline{\psi}\mathcal{D}\phi\ \exp[\mathrm{i}\,S(\psi,\phi+\Delta\phi)]}\\ &\quad+\frac{\int\mathcal{D}\psi\mathcal{D}\overline{\psi}\mathcal{D}\phi\ \psi(x_1)\Delta\phi(x_2)\overline{\psi}(x_3)\exp[\mathrm{i}\,S(\psi,\phi+\Delta\phi)]}{\int\mathcal{D}\psi\mathcal{D}\overline{\psi}\mathcal{D}\phi\ \exp[\mathrm{i}\,S(\psi,\phi+\Delta\phi)]}\\ &= \left\langle 0\middle|\mathrm{T}\,\psi(x_1)\phi(x_2)\overline{\psi}(x_3)\middle|0\right\rangle+\left\langle 0\middle|\mathrm{T}\,\psi(x_1)\Delta\phi(x_2)\overline{\psi}(x_3)\middle|0\right\rangle.\end{aligned} \tag{3.21}$$

The first term in the last line is just the new 3-point interaction. To interpret the second term, it is now time to take a closer look at the function $f(\psi,\phi)$ in expression (3.15b) of $\Delta\phi$. Without loss of generality, $f(\psi,\phi)$ can be factorized into $f(\psi,\phi)=\phi^k\tilde{f}(\partial)\psi^l\bar{\psi}^l$, where $\tilde{f}(\partial)$ is some function only depending on derivatives and $k,l\in\mathbb{N}$. Then the correlation function $\langle 0|\mathrm{T}\,\psi(x_1)\Delta\phi(x_2)\overline{\psi}(x_3)|0\rangle$ can be associated with the graph

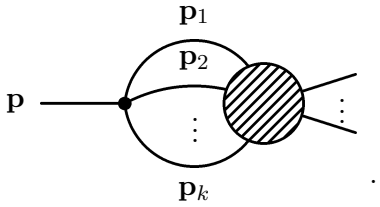

Thus, this term will be proportional to

$$\langle 0|\mathrm{T}\,\psi(x_1)\Delta\phi(x_2)\overline{\psi}(x_3)|0\rangle \propto \left[\left(\mathbf{p}_1^2-m_\phi^2\right)\left(\mathbf{p}_2^2-m_\phi^2\right)\cdots\left(\mathbf{p}_k^2-m_\phi^2\right)\right]^{-1}, \tag{3.22}$$

with $\mathbf{p}=\mathbf{p}_1+\mathbf{p}_2+\cdots+\mathbf{p}_k$. To see if such a term changes the physics, it is straightforward to calculate the S-matrix elements by use of the Lehmann-Symanzik-Zimmermann (LSZ)-reduction formula

$$\begin{aligned}
&\langle \mathbf{q}_{1,\phi},\ldots,\mathbf{q}_{a,\phi};\mathbf{q}_{1,\psi},\ldots,\mathbf{q}_{b,\psi};\mathrm{out}|\mathbf{p}_{1,\phi},\ldots,\mathbf{p}_{c,\phi};\mathbf{p}_{1,\psi},\ldots,\mathbf{p}_{b,\psi};\mathrm{in}\rangle\\
&=\text{disconnected}\ +\left(\frac{\mathrm{i}}{\sqrt{Z_\phi}}\right)^{a+c}\left(\frac{\mathrm{i}}{\sqrt{Z_\psi}}\right)^{2b}\int\left(\prod_{i=1}^{c}\mathrm{d}^4x_{j,\phi}e^{-\mathrm{i}\,p_{j,\phi}\,x_{j,\phi}}\right)\\
&\left(\prod_{j=1}^{b}\mathrm{d}^4x_{i,\psi}e^{-\mathrm{i}\,p_{j,\psi}\,x_{j,\psi}}\right)\left(\prod_{j=1}^{a}\mathrm{d}^4y_{j,\phi}e^{+\mathrm{i}\,q_{j,\phi}\,y_{j,\phi}}\right)\left(\prod_{j=1}^{b}\mathrm{d}^4y_{j,\psi}e^{+\mathrm{i}\,q_{j,\psi}\,y_{j,\psi}}\right)\\
&\left(\prod_{j=1}^{c}(\Box_{x_{j,\phi}}+m_\phi^2)\right)\left(\prod_{j=1}^{b}(\mathrm{i}\partial_{x_{j,\psi}}-m_\psi)\right)\left(\prod_{j=1}^{a}(\Box_{y_{j,\phi}}+m_\phi^2)\right)\left(\prod_{j=1}^{b}(\mathrm{i}\partial_{y_{j,\psi}}+m_\psi)\right)\\
&\langle 0;\mathrm{out}|\mathrm{T}\,\phi(x_{1,\phi})\cdots\phi(x_{c,\phi})\phi(y_{1,\phi})\cdots\phi(y_{a,\phi})\psi(x_{1,\psi})\cdots\psi(x_{b,\psi})\overline{\psi}(y_{1,\psi})\cdots\overline{\psi}(x_{b,\psi})|0;\mathrm{in}\rangle.
\end{aligned} \tag{3.23}$$

It is then easily seen that the corresponding S-matrix element to the graph sketched above is proportional to

$$\propto\frac{\mathbf{p}^2-m_\phi^2}{\left(\mathbf{p}_1^2-m_\phi^2\right)\left(\mathbf{p}_2^2-m_\phi^2\right)\cdots\left(\mathbf{p}_k^2-m_\phi^2\right)} \tag{3.24}$$

Taking then additionally the limit $\mathbf{p}^2\to m_\phi^2$, i. e. going on-shell, the vanishing numerator causes the change of the S-matrix elements to be absent in the case $k\geq 2$ because all the factors in the denominator stay finite. The S-matrix elements are thus not affected by the field-redefinition if $f(\psi,\phi)$ is quadratic or higher degree in ϕ. Hence, the original term in the Lagrangian (3.14) can be replaced with

$$-\epsilon^n f(\psi,\phi)m_\phi^2\phi \tag{3.25}$$

without changing the physics. However, for $k=1$, i. e. if $f(\psi,\phi)$ is linear in ϕ, the denominator of the propagator is canceled exactly by the factor in the numerator. The change in the S-matrix elements stays finite after taking the limit $\mathbf{p}^2\to m_\phi^2$. So a separate

treatment of these terms in the effective Lagrangian is required [30]. Nevertheless, we are allowed to perform a transformation (3.15a) with

$$\Delta\phi = \epsilon\, h(-\partial^2)(\partial^2 + m^2)\phi, \tag{3.26}$$

where h is some matrix function. The S-matrix elements are not affected by this change of variables because the factor $(\partial^2 + m^2)$ cancels the denominator and thus the change in the S-matrix elements vanishes in the LSZ reduction.

Consider now a term in the original Lagrangian of the form

$$\tilde{\epsilon}^n f(\psi, \phi)\partial\psi. \tag{3.27}$$

It follows analogously that such a term can be replaced by the nonlinear field-redefinition [32]

$$\overline{\psi} \to \overline{\psi}' = \overline{\psi} + \Delta\overline{\psi} \tag{3.28a}$$

$$\Delta\overline{\psi} = -\tilde{\epsilon}^n f(\psi, \phi). \tag{3.28b}$$

in favor of the term

$$-\tilde{\epsilon}^n f(\psi, \phi) m_\psi \psi. \tag{3.29}$$

In conclusion, the interaction of two off-shell fermions with an off-shell gauge boson can be described in full generality by an on-shell effective Lagrangian.

In the following the general γtt and Ztt Lagrangians including anomalous couplings originating from dimension-six gauge-invariant operators are reproduced [31]:

$$\mathcal{L}_{\gamma tt} = -eQ_\mathrm{t}\bar{t}\left[\gamma^\mu f_\mathrm{V}^\mathrm{A} + \frac{v}{\Lambda^2}\mathrm{i}\,\sigma^{\mu\nu}\mathbf{k}_\nu\left(d_\mathrm{V}^\mathrm{A} + \mathrm{i}\,d_\mathrm{A}^\mathrm{A}\gamma_5\right)\right] tA_\mu \tag{3.30}$$

$$\mathcal{L}_{Ztt} = \frac{g}{2\cos\theta_\mathrm{W}}\bar{t}\Bigg[\gamma^\mu\left(g_\mathrm{V} - g_\mathrm{A}\gamma_5\right) - \frac{v^2}{\Lambda^2}\left[\gamma^\mu\left(X_\mathrm{L}^\mathrm{Z}P_\mathrm{L} + X_\mathrm{R}^\mathrm{Z}P_\mathrm{R}\right) + \frac{\mathrm{i}\,\sigma^{\mu\nu}\mathbf{k}_\nu}{m_Z}\left(d_\mathrm{V}^\mathrm{Z} + \mathrm{i}\,d_\mathrm{A}^\mathrm{Z}\gamma_5\right)\right]\Bigg] tZ_\mu \tag{3.31}$$

Note that the expressions above differ slightly from Ref. [31] regarding the factor Q_t in $\mathcal{L}_{\gamma tt}$ and the SM term in $\mathcal{L}_{Ztt}$. The top quark photon interaction in (3.30) additionally involves the parameter f_V^A, which should not be understood as an anomalous coupling in the sense of the other parameters but rather as a rescaling of the top quark charge with $f_\mathrm{V}^\mathrm{A} = 1$ in the SM. All the other anomalous coupling parameters vanish in the SM.

4 WHIZARD

4.1 The WHIZARD program package

WHIZARD [19] is a generic Monte Carlo integration and event generation package for multi-particle processes. Three main features are provided: The generation of tree level matrix elements accomplished by the built-in programme O'Mega [34], the phase space integration using the adaptive multi-channel Monte Carlo integrator VAMP [35] and the generation of weighted as well as unweighted events. Since the matrix elements are calculated as helicity amplitudes, analyzes of spin and color correlations are possible. Additionally, for hadronic processes an interface to the LHAPDF library [36] for convoluting the partonic cross-section with PDFs as well as interfaces to PYTHIA [13] and HERWIG [14] for showering, fragmenting and hadronizing the final state are available. Moreover, the analysis of linear collider physics is supported by the inclusion of beamstrahlung (CIRCE [37]) and initial state radiation spectra for electrons and photons.

Among the currently supported physics models are the SM, optionally including anomalous couplings for gauge bosons or the top quark, the (Next-to-)Minimal Supersymmetric Standard Model, Little Higgs models and Z' models. Further models can be added. The new version 2.0 of WHIZARD was released in April 2010. The latest distribution can be downloaded at http://projects.hepforge.org/whizard/.

The overall architecture of WHIZARD is shown diagrammatically in figure 4.1. WHIZARD, O'Mega and VAMP were developed independently, each implemented in a programming language that was considered most suited for its purpose. The components are described separately in the following sections.

4.2 O'Mega (Optimized Matrix Element Generator)

The *Optimized Matrix Element Generator* O'Mega [34] constructs an optimized algebraic expression for a given scattering amplitude in a given model. O'Mega is implemented in the functional programming language O'CAML. Provided that a description of a target programming language is given, the amplitude can be computed in any language. Starting from a model description and a set of external particles the corresponding scattering amplitude is computed as a function of external momenta, spins and other quantum numbers.

As the complexity of a tree level scattering amplitude grows rapidly for processes with many particles in the final state due to the combinatorial explosion of the number of contributing Feynman diagrams, it is necessary to employ sophisticated methods in order to be able to calculate the amplitudes efficiently, though. In particular, in gauge theories the crucial point is to group terms efficiently in order to employ large numerical cancellations

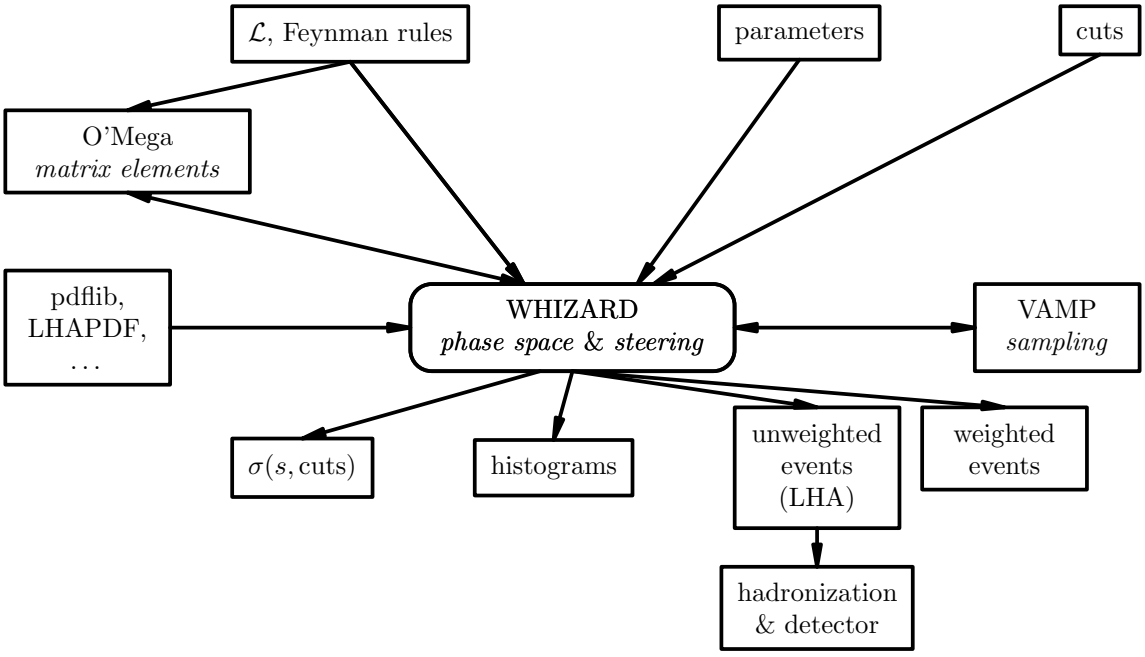

Figure 4.1: The overall architecture of WHIZARD. [19]

among terms from individual Feynman diagrams which are gauge dependent. O'Mega satisfies these requirements by computing helicity amplitudes by internally representing the scattering matrix element as a directed acyclical graph, where each subexpression appears only once. As a result the calculation effort does not grow with the factorial of the number of particles but only with an exponential. The implemented algorithm is presented in detail in [34].

4.3 VAMP

VAMP [35] is an acronym for *VEGAS AMPlified: Anisotropy, Multi-channel sampling and Parallelization*. As the name suggests, VAMP is an adaptive multi-dimensional Monte Carlo implementation in Fortran95 based on the classic VEGAS algorithm [38, 39]. Its main features are the support for stratified sampling in higher dimensions and for multi-channel sampling with individual adaptive grids. As a result, VAMP performs better than VEGAS for a class of integrals with nonfactorizable singularities as frequently appearing in particle physics. Furthermore, by separating the state from the function with a Fortran95 abstract type it is possible to run multiple instances of VEGAS in parallel. To better understand the advantages of the VAMP integrator the basic concepts of the adaptive Monte Carlo multi-channel sampling is outlined in the following.

The Monte Carlo method is the integration technique of choice for high dimensional integrals (dimension $d \gtrsim 3$) [35]. The integral

$$I(f) = \int_M \mathrm{d}\vec{x}\ f(\vec{x}) \tag{4.1}$$

of a function f on a manifold M with a set of integration variables $\vec{x}$ can be estimated by

$$E(f) = \left\langle \frac{f}{g} \right\rangle_g = \frac{1}{N} \sum_{i=1}^{N} \frac{f(\vec{x}_i)}{g(\vec{x}_i)}. \tag{4.2}$$

Herein $g(\vec{x})$ is the probability density of the randomly distributed $\vec{x}_i$ and N refers to the number of sampling points. Moreover, the standard derivation

$$\sigma_V(f) = \sqrt{V(f)} \quad \text{with} \quad V(f) = \frac{1}{N-1} \left(\left\langle \left(\frac{f}{g} \right)^2 \right\rangle_g - \left\langle \frac{f}{g} \right\rangle_g^2 \right) \tag{4.3}$$

gives an estimate of the error of $E(f)$, which is, in particular, proportional to $\sim 1/\sqrt{N}$ for a large number of sampling points. The aim of an adaptive Monte Carlo algorithm is to optimize the probability density $g(\vec{x})$ such that the variance $V(f)$ is minimal. One possibility of doing so is the so-called *importance sampling*, which the `VEGAS` algorithm is based on [38]. In this method the sampling points are concentrated in the regions of f that mostly contribute to the integral. Another approach is the *stratified sampling* technique, which is used by `VAMP`. The goal of this approach is to partition the integration region such that the variation of function values within each region is small [40].

In contrast to the classic `VEGAS` algorithm, `VAMP` comes additionally with a multi-channel sampling strategy. The use of this advanced technique is briefly motivated in the following. In general, the Monte Carlo integration technique works well for rather smooth integrands. However, difficulties are encountered if the integrand fluctuates wildly over the integration domain. This is usually the case for the phase space integration of differential cross-sections in particle physics due to the involved propagators, which may have almost vanishing denominators in specific phase space regions. These sharp peaks in the integrand will be called quasi-singularities in the following. If the quasi-singularities factorize, it is straightforward to find substitutions that "flatten" the integrand. As a simple example may serve the integral

$$I_{\text{ex.}} = \int_{\epsilon}^{b} \mathrm{d}x \; \frac{f(x)}{x}, \tag{4.4}$$

with $\epsilon \sim 0$, $b > \epsilon > 0$. Assuming that the pole at $x = 0$ is not killed by $f(x)$, the integrand obviously has a singularity at this point. This will give rise to difficulties in sampling. To overcome this problem one can perform the substitution $x \to x' = \ln x$, by which the integral (4.4) is transformed into

$$I_{\text{ex.}} = \int_{\ln \epsilon}^{\ln b} \mathrm{d}x \; \left| \frac{\partial x'}{\partial x} \right| f\big(x(x')\big) = \int_{\ln \epsilon}^{\ln b} \mathrm{d}x' \; f\big(e^{x'}\big). \tag{4.5}$$

In this way the quasi-singularity is removed from the integrand. Thus the Monte Carlo integration of (4.5) will perform significantly better than that of (4.4).
Of course, it is not convenient to manually tune the integrand by searching for favorable substitutions as in the example above. Instead, `VEGAS` is able to find a suitable probability density g through an iterative adaptive phase such that the variance $V(f)$ is minimized.

The crucial point now is that the VEGAS algorithm works only efficiently for integrands with factorizable quasi-singularities, that is to say with integrands whose characteristic structures are aligned with the coordinate axis [41]. However, if the integrand is a sum of terms, each with factorizable quasi-singularities that factorize in a *different* coordinate system, this algorithm will fail. This is because it is not possible to find one single substitution for which the quasi-singularities of all terms factorize at the same time. Consider for example the functions

$$f_1(x,y) = \frac{1}{(x-y)^2+\epsilon} \tag{4.6a}$$

$$f_2(x,y) = \frac{1}{(\sqrt{x^2+y^2}-r)^2+\epsilon}, \tag{4.6b}$$

where ϵ is a small parameter. Each function is factorizable in a specific coordinate system and can then be sampled by VEGAS efficiently. However, this is not the case for the sum $f_1(x,y) + f_2(x,y)$ because there is no parameterization where both terms factorize simultaneously. A way out of this difficulty may provide the *multi-channel sampling* approach [42]. This method makes use of the fact that there are more distinct ways of mapping random numbers into $\vec{x}$, that is to say there are different channels. Each of the N_c channels comes with a different probability density $g_i(\vec{x})$, which is non-negative and normalized to unity

$$\int_M \mathrm{d}\vec{x}\; g_i(\vec{x}) = 1. \tag{4.7}$$

The total probability density $g(\vec{x})$ can then be written as the linear combination

$$g(\vec{x}) = \sum_{i=1}^{N_c} \alpha_i g_i(\vec{x}), \tag{4.8}$$

where the probabilities α_i for channel i obey the conditions

$$0 \leq \alpha_i \leq 1 \tag{4.9a}$$

$$\sum_{i=1}^{N_c} \alpha_i = 1 \tag{4.9b}$$

and thus guarantee the normalization of $g(\vec{x})$ to unity, too. With the total probability density (4.8) the original integral (4.1) can be rewritten as

$$I(f) = \int \mathrm{d}\vec{x}\; f(\vec{x}) = \sum_{i=1}^{N_c} \alpha_i \int \underbrace{\mathrm{d}\vec{x}\; g_i(\vec{x})}_{=\mathrm{d}\vec{\xi}_i} \frac{f(\vec{x})}{\sum_{j=1}^{N_c} \alpha_j g_j(\vec{x})} = \sum_{i=1}^{N_c} \alpha_i \int_0^1 \mathrm{d}\vec{\xi}_i\; \frac{f(\vec{x}(\vec{\xi}_i))}{\sum_{j=1}^{N_c} \alpha_j g_j(\vec{x}(\vec{\xi}_i))} \tag{4.10}$$

It is convenient to use the same integration domain for all ξ_i, which is chosen to be the d-dimensional (d: dimension of the integral) unit hypercube. That is why the integration limits are stated explicitly for the last integral in (4.10). The estimate of the integral is

found to be [35]

$$E(f) = \sum_{i=1}^{N_c} \alpha_i \left\langle \frac{f(\vec{x}(\vec{\xi}_i))}{\sum_{j=1}^{N_c} \alpha_j g_j(\vec{x}(\vec{\xi}_i))} \right\rangle_{g_i} . \tag{4.11}$$

To minimize the variance of this estimate the single probability densities $g_i(\vec{x})$ as well as the probabilities α_i are optimized in the subsequent adaption process. For the latter `VAMP` employs the numerical procedure suggested in [42], the optimization of the $g_i(\vec{x})$ for each parameter set is accomplished by the original `VEGAS` algorithm.

Although the multi-channel approach involves additional computational effort compared to the classic `VEGAS` algorithm for the calculation of all the distinct mappings as well as for the optimization of the α_i, the `VAMP` algorithm shows significant performance enhancements for a large class of integrals [35].

5 Calculation of total reaction cross-sections

5.1 The factorization theorem

In the parton model the constituents of hadrons are partons, that is gluons and quarks, which form an extended object by their mutual interaction. In general, proton-proton scattering cannot be calculated by perturbative QCD in a series in the strong coupling constant α_s because it is not an expansion in a small parameter at a low energy scale or long distances. However, at high energies or short distances α_s becomes small and parton-parton interaction may be neglected (cf. section 3.2). The idea of separating the short distance from the long distance dynamics is employed in the factorization theorem [43] of perturbative QCD. This theorem's statement is that the parton model cross-section $\hat{\sigma}$ for deeply inelastic scattering is given by:

$$\hat{\sigma}(s) = \underbrace{\sum_{i,j}}_{\text{sum over types of partons}} \underbrace{\int_0^1 \int_0^1 \mathrm{d}x_1 \mathrm{d}x_2 f_i(x_1,\mu) f_j(x_2,\mu)}_{\text{soft interaction}} \underbrace{\sigma\big(p_i(x_1) p_j(x_2) \to X; \mu\big)}_{\text{hard interaction}} \tag{5.1}$$

Equation (5.1) can be interpreted as follows [43, 44]:
Consider the reaction of two protons moving rapidly towards each other at a very high center-of-mass energy $\sqrt{s}$ compared to the proton mass, as in a proton-proton collision at the LHC. In the center-of-mass frame the protons are Lorentz contracted in the direction of the collision axis and the internal interactions are lengthened by time dilation. Thus, the lifetime of the virtual partonic state becomes much longer than the time it takes the protons to traverse each other. During this time each can be described by a single virtual state of a certain number of constituents, which do not interact. The protons are "frozen". As a consequence, each parton can be associated with a definite momentum. As hard interactions inside each proton are suppressed at large momentum scales, the momentum of the constituents cannot acquire a large transverse component but is almost collinear with the momentum of the proton. Hence, to leading order the momentum of each constituent is a certain longitudinal fraction x of the momentum of the proton, where $0 \leq x \leq 1$. As a further implication of time dilation there is no interference between the soft interactions before and after the hard scattering process. Taking all this into consideration, the factorization of soft and hard interactions of equation (5.1) may be read the following way: The hard scattering cross-section σ calculated for free initial state partons p_i and p_j with definite longitudinal momentum fractions x_1 and x_2, respectively, multiplies the probabilities $f_i(x_1,\mu)$ and $f_j(x_2,\mu)$ for finding a parton with fraction $x_{1/2}$ inside the proton, is finally integrated over all values of $x_{1/2}$ and, if applicable, summed over all possible types (i. e. gluon, (anti-)up quark, ...) of initial partons.

The functions $f_i(x,\mu)$ are referred to as parton distribution functions (PDFs). As they involve the long-distance dynamics, the PDFs are not calculable and have to be determined from experiment. Nevertheless, once measured, predictions for other processes

can be made because, being insensitive to short-distance interactions, they are universal [45]. The calculation of the hard scattering cross-section σ is discussed in the following section.

The hard scattering cross-section σ and the PDFs depend on the renormalization scale μ_R and the factorization scale μ_F. The latter is introduced by the factorization ansatz. In practice of using, both quantities are often set to the same relevant scale $\mu = \mu_F = \mu_R$, which is usually taken to be the top quark mass in top quark studies [46]. The cross-section would be independent of μ for the complete perturbation series. As such a calculation cannot be accomplished, a μ-dependence remains in the results, which has to be tested by varying the scale in a certain range.

5.2 The hard scattering cross-section

The total reaction cross-section of a hard scattering $2 \to n$ process can be calculated in perturbation theory according to the formula

$$\sigma = \underbrace{\frac{1}{F}}_{\text{flux factor}} \underbrace{\int \prod_{i=1}^{n} \frac{\mathrm{d}^3 p_i}{2E_i} \, \delta^{(4)}\left(\mathbf{p}_a + \mathbf{p}_b - \sum_{j=1}^{n} \mathbf{p}_j\right)}_{\text{phase space integral}} \underbrace{|\overline{\mathcal{M}}|^2}_{\text{squared matrix element}} \quad . \tag{5.2}$$

Herein $\mathbf{p}_a$ and $\mathbf{p}_b$ denote the definite four-momenta of the incoming, $\mathbf{p}_i$ $(i = 1, \ldots, n)$ those of the outgoing particles. $|\overline{\mathcal{M}}|^2$ is the absolute squared value of the Feynman amplitude, where averaging over polarizations of the initial state particles and summation over polarizations of the final state particles is implied.

In detail the calculation of the hard scattering cross-section includes the following technical steps:

- Determination of all Feynman graphs that contribute to the process of interest
- Applying the Feynman rules to translate the graphs into an analytical expression for all amplitudes $\mathcal{M}_i$
- Calculation of the squared amplitude $|\mathcal{M}|^2 = |\sum_i \mathcal{M}_i|^2$, including:
  - Average over the polarization of incoming particles; average over color of incoming particles if applicable
  - Summation over polarization and, if applicable, color of the outgoing particles
  - Calculation of the color factor to the square of each individual diagram if applicable
  - Calculation of the traces of the Dirac matrices. In this work, this step is done with the `FeynCalc` package (version 5.1) [47] for the computer algebra system `Mathematica` [48].
  - Contraction of all Lorentz indices and analytical simplification of the obtained expression. This is done with `FeynCalc` / `Mathematica` as well in this work.
- Insert scalar products in terms of parameters of the phase space parameterization
- Perform the phase space integral. Whereas for processes with a final state with two particles the phase space integration can be performed analytically, the integral for a three-particle final state is more involved and is thus replaced by an numerical

estimate employing the adaptive Monte Carlo algorithm `VEGAS`, which is part of the `CUBA` library (version 1.7) [41]. For performance reasons the numerical integration is implemented in the programming language `C`.

- Multiply with the flux-factor

The general structure of a matrix element $\mathcal{M}$ for processes with photon or gluon radiation and its peculiarities is considered in section 5.3. The expression for the flux factor is given in section 5.4. Finally, the treatment of the phase space of a three-particle final state deserves particular attention and is thus discussed separately in chapter 6.

5.3 Matrix element for processes with photon / gluon radiation

The general form of the Feynman amplitude for processes with final state photon or gluon radiation will be discussed in this section. For this purpose, first of all the amplitude of a general process $x \to f\bar{f}$ with two fermions in the final state with momenta $\mathbf{p}_f$ and $\mathbf{p}_{\overline{f}}$ is considered.

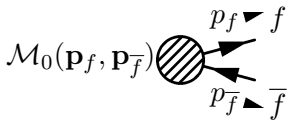

The Feynman-amplitude of this process takes the simple form

$$\mathcal{M} = \overline{u}_r(\mathbf{p}_f)\mathcal{M}_0(\mathbf{p}_f, \mathbf{p}_{\overline{f}})v_s(\mathbf{p}_{\overline{f}}). \tag{5.3}$$

How does this amplitude change for the same process but with additional final state photon radiation $x \to f\bar{f}\gamma$? In the following discussion it is assumed that the photon can only be radiated either by the fermion or the anti-fermion. Therefore, there are the two graphs

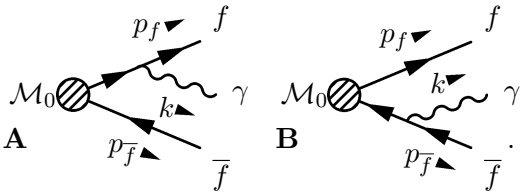

Obeying the Feynman rules the corresponding amplitude reads

$$\mathcal{M} = \epsilon^*_\mu(\mathbf{k})\mathcal{M}^\mu(\mathbf{k}) = -\mathrm{i}\,e\,Q_f\;\overline{u}_r(\mathbf{p}_f)\Bigg[\underbrace{\Gamma^\mu \mathrm{i}\frac{\not{p}_f + \not{k} + m_f}{(\mathbf{p}_f+\mathbf{k})^2 - m_f^2}\mathcal{M}_0(\mathbf{p}_f+\mathbf{k}, \mathbf{p}_{\overline{f}})}_{\mathbf{A}} + \underbrace{+\,\mathcal{M}_0(\mathbf{p}_f, \mathbf{p}_{\overline{f}}+\mathbf{k})\mathrm{i}\frac{-\not{p}_{\overline{f}} - \not{k} + m_f}{(\mathbf{p}_{\overline{f}}+\mathbf{k})^2 - m_f^2}\Gamma^\mu}_{\mathbf{B}}\Bigg]\epsilon^*_\mu(\mathbf{k})v_s(\mathbf{p}_{\overline{f}}) \tag{5.4}$$

with the general $f\bar{f}\gamma$ vertex $(-\mathrm{i}\, e\, Q_f\, \Gamma^\mu)$ and the charge of the fermion Q_f in units of the electron charge. Note the minus signs at the momenta in the numerator of the second propagator, which respect the opposite direction of momentum and fermion line.

Structure of propagators in bremsstrahlung diagrams

As seen in expression (5.4), the propagators involved in amplitudes with photon / gluon radiation have the generic structure

$$\frac{\not{\mathbf{p}}_f + \not{\mathbf{k}} + m_f}{(\mathbf{p}_f + \mathbf{k})^2 - m_f^2}. \tag{5.5}$$

For on-shell particles in the final state, i. e. $\mathbf{p}_f^2 = m_f^2$ and $\mathbf{k}^2 = 0$, the form (5.5) reduces to

$$\frac{\not{\mathbf{p}}_f + \not{\mathbf{k}} + m_f}{2\ \mathbf{p}_f \cdot \mathbf{k}} = \frac{\not{\mathbf{p}}_f + \not{\mathbf{k}} + m_f}{2E_f E_\mathrm{k}(1 - v_f \cos\theta_{\mathbf{p},\mathbf{k}})} \tag{5.6}$$

$$\text{with} \quad v_f = \frac{|\vec{p}_f|}{E_f} = \sqrt{1 - \frac{m_f^2}{E_f^2}}. \tag{5.7}$$

In the transformation done in 5.6 the dot product of the four-vectors in the denominator is written out explicitly. From the latter expression in 5.6 the divergent behavior can easily be extracted. It shows that the cross-section of bremsstrahlung diagrams is ...

infrared-divergent. As will be discussed in chapter 6, the cross-section σ has the proportionality $\sigma \propto \lim\limits_{a\to 0} \int_a^{E_\mathrm{max}} \frac{dE_\mathrm{k}}{E_\mathrm{k}} \propto \Big(\text{const.} - \lim\limits_{a\to 0} \ln a\Big)$. Hence, σ is logarithmic divergent in the soft photon / gluon limit, that is to say in the limit where the energy of the radiated particle tends to zero. In this study we are only interested in physically measurable particles. Therefore, we demand the radiated particle to have a minimal energy $E_k > E_\mathrm{min} > 0$ and thereby circumvent this problem. However, it is noted for completeness that, if the amplitude was considered including all radiative corrections, additional IR-divergent terms originating from vertex corrections would contribute. These counterterms have the same asymptotic behavior and thus cancel the divergent terms [44].

collinear divergent for massless fermions ($m_f \to 0$). The fermion mass vanishing, the velocity v_f (5.7) approaches 1. Thus, the denominator tends to 0 for $|\cos\theta_{\mathbf{p},\mathbf{k}}| \to 1$; the cross-section is collinear divergent. As in this work the bremsstrahlung of the top quark is discussed, the fermion mass $m_f = m_\mathrm{t}$ is fairly greater than 0. Yet, this divergent behavior makes an impact on the convergence of the numerical integration when studying the limit $\sqrt{s} \gg m_f$.

If the decay width of the fermion is considered, the extra term $\mathrm{i}\, m_f \Gamma_f$ is added in the denominator of the propagator. In this work the convention is followed that this term is only added if the momentum $\mathbf{p}$ involved in the propagator is spacelike ($\mathbf{p}^2 > 0$) with the objective of keeping unitarity. This means that the extra term reads rather $\mathrm{i}\, m_f \Gamma_f \theta(\mathbf{p}^2)$. It is important to mention that this additional term violates gauge invariance. To see this, it is useful to check the Ward identity [49] for the amplitude $\mathcal{M}^\mu(\mathbf{k})$ of the example

calculation (5.4) explicitly for $\Gamma^\mu = \gamma^\mu$:

$$\mathbf{k}_\mu \mathcal{M}^\mu(\mathbf{k}) \propto \overline{u}(\mathbf{p}_f) \not{\mathbf{k}} \frac{\not{\mathbf{p}}_f + \not{\mathbf{k}} + m_f}{2\ \mathbf{p}_f \cdot \mathbf{k} + \mathrm{i}\ m_f \Gamma_f} \mathcal{M}_0\ v(\mathbf{p}_{\overline{f}}) + \overline{u}(\mathbf{p}_f) \mathcal{M}_0 \frac{-\not{\mathbf{p}}_{\overline{f}} - \not{\mathbf{k}} + m_f}{2\ \mathbf{p}_{\overline{f}} \cdot \mathbf{k} + \mathrm{i}\ m_f \Gamma_f} \not{\mathbf{k}}\ v(\mathbf{p}_{\overline{f}}) \tag{5.8}$$

Employing the anticommutation relation of Dirac matrices, $\{\gamma^\mu, \gamma^\nu\} = 2g^{\mu\nu}$, equation (5.8) transforms into

$$\begin{aligned} \mathbf{k}_\mu \mathcal{M}^\mu(\mathbf{k}) \propto \overline{u}(\mathbf{p}_f) \frac{(-\not{\mathbf{p}}_f + m_f)\not{\mathbf{k}} + \not{\mathbf{k}}^2 + 2\ \mathbf{p}_f \cdot \mathbf{k}}{2\ \mathbf{p}_f \cdot \mathbf{k} + \mathrm{i}\ m_f \Gamma_f} \mathcal{M}_0\ v(\mathbf{p}_{\overline{f}}) + \\ + \overline{u}(\mathbf{p}_f) \mathcal{M}_0 \frac{-\not{\mathbf{k}}^2 - 2\ \mathbf{p}_{\overline{f}} \cdot \mathbf{k} + \not{\mathbf{k}}(\not{\mathbf{p}}_{\overline{f}} + m_f)}{2\ \mathbf{p}_{\overline{f}} \cdot \mathbf{k} + \mathrm{i}\ m_f \Gamma_f} v(\mathbf{p}_{\overline{f}}). \end{aligned} \tag{5.9}$$

As the four-vectors $\mathbf{p}_f$ and $\mathbf{p}_{\overline{f}}$ satisfy the Dirac equations $0 = \overline{u}(\mathbf{p}_f)(-\not{\mathbf{p}}_f + m_f)$ and $(\not{\mathbf{p}}_{\overline{f}} + m_f)v(\mathbf{p}_{\overline{f}}) = 0$, respectively, and by use of $\not{\mathbf{k}}^2 = \mathbf{k}^2 = 0$, one obtains

$$\mathbf{k}_\mu \mathcal{M}^\mu(\mathbf{k}) \propto \overline{u}(\mathbf{p}_f) \frac{2\ \mathbf{p}_f \cdot \mathbf{k}}{2\ \mathbf{p}_f \cdot \mathbf{k} + \mathrm{i}\ m_f \Gamma_f} \mathcal{M}_0\ v(\mathbf{p}_{\overline{f}}) - \overline{u}(\mathbf{p}_f) \mathcal{M}_0 \frac{2\ \mathbf{p}_{\overline{f}} \cdot \mathbf{k}}{2\ \mathbf{p}_{\overline{f}} \cdot \mathbf{k} + \mathrm{i}\ m_f \Gamma_f} v(\mathbf{p}_{\overline{f}}). \tag{5.10}$$

Without considering the decay width, the numerator and denominator in the first and second term cancel each and the expression on the right hand side of expression (5.10) vanishes. However, for non-vanishing decay width it does not. Hence, one has

$$\mathbf{k}_\mu \mathcal{M}^\mu(\mathbf{k}) \neq 0 \text{ for } \Gamma_f > 0, \tag{5.11}$$

that is to say the Ward identity does not hold; gauge invariance is violated. As a consequence, the simple photon / gluon polarization sum $\sum_{\text{pol.}} \epsilon^{\mu *} \epsilon^\nu \to -g^{\mu\nu}$ must be replaced with the physical polarization sum

$$\sum_{\text{pol.}} \epsilon^{\mu *} \epsilon^\nu \to -g^{\mu\nu} - \frac{\mathbf{k}^\mu \mathbf{k}^\nu - (\mathbf{k} \cdot \mathbf{n})(\mathbf{k}^\mu \mathbf{n}^\nu + \mathbf{k}^\nu \mathbf{n}^\mu)}{(\mathbf{k} \cdot \mathbf{n})^2} \tag{5.12}$$

with $\mathbf{n}^\mu = (1, \vec{0})$ to substract the contributions of unphysical polarizations.

5.4 Flux factor

The flux factor F in equation (5.2) is given by

$$F = 2\sqrt{\lambda(s, m_a^2, m_b^2)}\ (2\pi)^{3n-4} = 4\sqrt{(\mathbf{p}_a \cdot \mathbf{p}_b)^2 - m_a^2 m_b^2}\ (2\pi)^{3n-4}, \tag{5.13}$$

where m_a and m_b is the mass of the initial state particle p_a and p_b, respectively, and

$$\lambda(x, y, z) = x^2 + y^2 + z^2 - 2xy - 2xz - 2yz. \tag{5.14}$$

the kinematical function.

6 Three particle phase space

6.1 Prerequisites

The *momentum space* of a n-particle final state is $3n$-dimensional. Due to constraints such as conservation laws the number of independent parameters is reduced to $3n-4$ (see section 6.2). This lower dimensional sub-space of the momentum space, which in general may have a rather complicated shape, is referred to as the n-particle *phase space* (see figure 6.1). The *phase space parameterization* maps these two spaces to each other. Such a parameterization should meet the following requirements:

- Coverage of the whole phase space: Due to the usually complicated shape of the phase space this requirement is of particular importance. In addition, double counting of phase space regions must be avoided.
- Possibility to apply cuts on parameters of interest: For comparison of the theoretical results with experimental data cuts on specific parameters are required. In this study a cut on the energy of the radiated photon is used in particular.
- Allowing convenient integration: Eventually, the phase space integration has to be performed to obtain the total reaction cross-section. Therefore, the parameterization of the phase space should ideally provide the possibility of performing the integration analytically. However, an analytical integration cannot be done in general for the matrix elements considered and is replaced by a numeric estimate instead. Yet, the parameterization should allow a highly performant numerical integration.

6.2 Determination of the number of independent parameters

Before writing down a phase space parameterization, the dimension of the phase space, i. e. the number of independent final state parameters, has to be known (see also Ref. [50]). As there are 4 degrees of freedom per particle, namely its energy and components of the

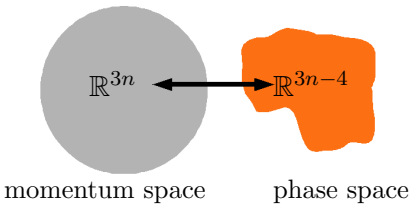

Figure 6.1: The *phase space* is the lower dimensional sub-space of the *momentum space*. Due to constraints the phase space may have a rather complicated shape. The two spaces are mapped to each other by the *phase space parameterization*.

		$n=3$	$n=2$
4 degrees of freedom per particle (E,p_x,p_y,p_z)	$n \cdot 4$	12	8
- relation energy - momentum (for each particle)	$-n \cdot 1$	$-$ 3	$-$ 2
- conservation of energy / momentum	$-$ 4	$-$ 4	$-$ 4
- rotational symmetry around beam axis	$-$ 1	$-$ 1	$-$ 1
= essential final state variables	$\mathbf{3n-5}$	**4**	**1**

Table 6.1: Determination of the number of independent parameters for a n-particle, 3-particle and 2-particle final state, respectively. As shown, the phase space is $3n-5$-dimensional for a final state with rotational symmetry around the beam axis and on-shell particles.

three-dimensional momentum vector, altogether $4n$ parameters of the n-particle final state have to be determined. For on-shell final state particles the energy of each particle can be expressed in terms of the corresponding three-momentum. Thus $3n$ degrees of freedom remain to span the $3n$-dimensional momentum space. Exploiting the total conservation of energy and three-momentum this number can be reduced by 4, so that $3n-4$ independent essential phase space parameters are left. For collider experiments one can further get rid of one additional degree of freedom taking into account the rotational symmetry around the beam axis. Therefore, in the end there are $3n-5$ essential final state variables for a n-particle final state or, in concrete terms, 4 essential final state variables for a 3-particle final state. Table 6.1 sums up the determination of the number of independent parameters.

6.3 Parameterization of the 3-particle phase space

In general there are different ways of writing down an explicit parameterization of the phase space. As will be seen in section 7.2, a highly performant numerical phase space integration requires different parameterizations for a single process. In this paragraph the explicit parameterizations of a 3-particle final state that are employed in this work are presented.

For this purpose the generic process $p_a p_b \to p_1 p_2 p_3$

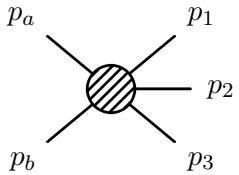

is considered. The corresponding four-vectors are denoted by

$$\mathbf{p}_a = \begin{pmatrix} E_a \\ \vec{p}_a \end{pmatrix},\ \mathbf{p}_b = \begin{pmatrix} E_b \\ \vec{p}_b \end{pmatrix},\ \mathbf{p}_1 = \begin{pmatrix} E_1 \\ \vec{p}_1 \end{pmatrix},\ \mathbf{p}_2 = \begin{pmatrix} E_2 \\ \vec{p}_2 \end{pmatrix} \text{ and } \mathbf{p}_3 = \begin{pmatrix} E_3 \\ \vec{p}_3 \end{pmatrix},$$

respectively. As determined in the previous section, 4 parameters are sufficient to span the phase space of a final state with 3 on-shell particles. Three different parameterizations are used throughout this work.

Parameterization 1 utilizes the following parameters:

E_3 energy of particle p_3

θ angle between $\vec{p}_a$ and $\vec{p}_1$

θ' angle between $\vec{p}_1$ and $\vec{p}_3$

ϕ angle between the planes spaned by ($\vec{p}_a$,$\vec{p}_1$) and ($\vec{p}_1$,$\vec{p}_3$)

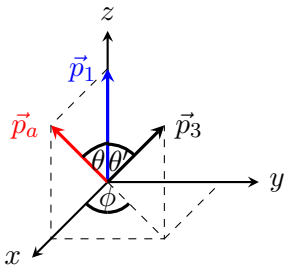

Throughout this work all quantities are defined in the center-of-momentum system (COM) if not stated otherwise. **Parameterization 2** involves E_1, the energy of particle p_1, rather than E_3. The other three parameters are the same as in parameterization 1. **Parameterization 3** is obtained out of parameterization 2 by replacing all indices 1 with 2, i. e. involves the parameters:

E_2 energy of particle p_2

$\widetilde{\theta}$ angle between $\vec{p}_a$ and $\vec{p}_2$

$\widetilde{\theta'}$ angle between $\vec{p}_2$ and $\vec{p}_3$

$\widetilde{\phi}$ angle between the planes spaned by ($\vec{p}_a$,$\vec{p}_2$) and ($\vec{p}_2$,$\vec{p}_3$)

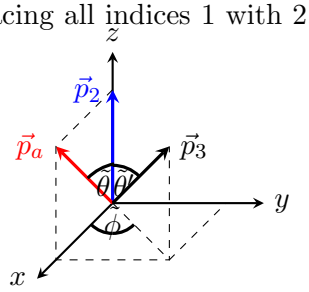

In order to see that the above stated sets of parameters are maps of the full 3-particle phase space, it is shown in the following that the four parameters of each set are sufficient to express all the involved four-vectors. For parameterization 1 and 2 the coordinate system is chosen, without loss of generality, such that the three-vector of particle p_1 is parallel to the z-axis and $\vec{p}_a$ is located in the x-z-plane requiring one parameter θ (see graphic above). Furthermore, the orientation of the three-vector of particle p_3 relative to $\vec{p}_1$ and $\vec{p}_a$ is described by three-dimensional spherical coordinates, i. e. θ' and ϕ as defined above come into play. Since all the particles are assumed to be on-shell, the norm of the three-vectors $|\vec{p}_1|$ and $|\vec{p}_3|$ can be determined employing the energy-momentum-relation $|\vec{p}_i|^2 = E_i^2 - m_i^2$ ($i = 1, 3$). Finally, respecting the total conservation of energy and momentum

$$\mathbf{p}_a + \mathbf{p}_b = \mathbf{p}_1 + \mathbf{p}_2 + \mathbf{p}_3, \tag{6.1}$$

the remaining four-vector of particle p_2 is determined. Therefore, the four-vectors of all the particles read:

$$\mathbf{p}_1 = \begin{pmatrix} E_1 \\ 0 \\ 0 \\ |\vec{p}_1| \end{pmatrix}; |\vec{p}_1| = \sqrt{E_1^2 - m_1^2} \tag{6.2a}$$

$$\mathbf{p}_{a/b} = \begin{pmatrix} E_{a/b} \\ \pm\,|\vec{p}|\sin\theta \\ 0 \\ \pm\,|\vec{p}|\cos\theta \end{pmatrix}; |\vec{p}| = E_{a/b} = \frac{\sqrt{s}}{2} \tag{6.2b}$$

$$\mathbf{p}_3 = \begin{pmatrix} E_3 \\ |\vec{p}_3|\sin\theta'\cos\phi \\ |\vec{p}_3|\sin\theta'\sin\phi \\ |\vec{p}_3|\cos\theta' \end{pmatrix}; |\vec{p}_3| = \sqrt{E_3^2 - m_3^2} \tag{6.2c}$$

$$\mathbf{p}_2 = \mathbf{p}_a + \mathbf{p}_b - \mathbf{p}_1 - \mathbf{p}_3 = \begin{pmatrix} \sqrt{s} - E_1 - E_3 \\ -\vec{p}_1 - \vec{p}_3 \end{pmatrix} \tag{6.2d}$$

As is obvious from equations (6.2), E_1 or E_3 has to be eliminated to be left only with the four parameters of parameterization 1 or 2, respectively. This is achieved be demanding particle p_2 to be on-shell, too, i. e.

$$\mathbf{p}_2^2 \stackrel{!}{=} m_2^2. \tag{6.3}$$

It shows, however, that solving equation (6.3) for E_1 or E_3, respectively, is not as straightforward as one might expect. Actually, this is the point where the non-trivial shape of the phase space originates from. The solution depends on the masses of the final state particles. It is particularly important if they are massive or massless. Thus, solving equation (6.3) is discussed in great detail in the following subsections, starting with the most general case, in which all the final state particles may have different masses. After that, relevant special cases of actual occurring physical processes are taken into consideration.

The expressions of the four-vectors in terms of variables of parameterization 3 are obtained out of parameterization 2 by replacing the variables of particle p_1 by the corresponding ones of particle p_2 and vice versa. The formulas are therefore not stated explicitly.

6.3.1 Three particles with different masses

As mentioned above, the excess variable in expressions (6.2) can be eliminated employing the on-shell condition (6.3). In the most general case of three final state particles with masses m_1, m_2, $m_3 > 0$, this equation reads for parameterization 1

$$\begin{aligned}\mathbf{p}_2^2 - m_2^2 = (\mathbf{p}_a + \mathbf{p}_b - \mathbf{p}_1 - \mathbf{p}_3)^2 - m_2^2 = \\ = s - 2\sqrt{s}E_1 - 2\sqrt{s}E_3 + 2E_1E_3 - 2\sqrt{E_1^2 - m_1^2}\sqrt{E_3^2 - m_3^2}\cos\theta' + \\ + m_1^2 + m_3^2 - m_2^2 = 0.\end{aligned} \tag{6.4}$$

With the aim of solving for E_1, equation (6.4) is transformed into

$$s - 2\sqrt{s}E_1 - 2\sqrt{s}E_3 + 2E_1E_3 + m_1^2 + m_3^2 - m_2^2 = 2\sqrt{E_1^2 - m_1^2}\sqrt{E_3^2 - m_3^2}\cos\theta', \tag{6.5}$$

and after squaring this expression into

$$\left(s - 2\sqrt{s}E_1 - 2\sqrt{s}E_3 + 2E_1E_3 + m_1^2 + m_3^2 - m_2^2\right)^2 = 4\left(E_1^2 - m_1^2\right)\left(E_3^2 - m_3^2\right)\cos\theta'^2. \tag{6.6}$$

The former step is of particular importance because by raising the cosine to the second power the information of the sign of this term is lost. Additional solutions, which do not satisfy the original equation (6.4), are created thereby. Since (6.6) is a quadratic equation in E_1, two solutions, namely

$$E_{1,1} = \frac{A + \sqrt{\Delta}\,|\cos\theta'|}{B} \tag{6.7a}$$

$$E_{1,2} = \frac{A - \sqrt{\Delta}\,|\cos\theta'|}{B}, \tag{6.7b}$$

are obtained, with

$$A = -\left(E_3 - \sqrt{s}\right)\left(-m_1^2 + m_2^2 - m_3^2 + 2E_3\sqrt{s} - s\right), \tag{6.8a}$$

$$B = -2\left(E_3 - \sqrt{s}\right)^2 + 2(E_3^2 - m_3^2)\cos\theta'^2, \tag{6.8b}$$

$$\begin{aligned}\Delta = \left(E_3^2 - m_3^2\right)\Big[m_1^4 + 4E_3\left(m_1^2 + m_2^2 - m_3^2 - s\right)\sqrt{s} + \left(-m_2^2 + m_3^2 + s\right)^2 + \\ 4E_3^2\left(s + m_1^2\left(-1 + \cos\theta'^2\right)\right) - 2m_1^2\left(m_2^2 + s + m_3^2(-1 + 2\cos\theta'^2)\right)\Big].\end{aligned} \tag{6.8c}$$

Both solutions are real valued only if the discriminant Δ is not negative:

$$\Delta \overset{!}{\geq} 0 \tag{6.9}$$

This condition implies automatically the physically maximal possible energy of particle p_3 dependend on $\cos\theta'$ and on the masses m_1 to m_3. This specific maximal energy will be denoted by $E_{3,\max}$ and is, according to condition (6.9), given by

$$\begin{aligned}E_{3,\max}(\cos\theta') = -\frac{1}{2\left(s + m_1^2\left(-1 + \cos\theta'^2\right)\right)}\Big[\left(m_1^2 + m_2^2 - m_3^2 - s\right)\sqrt{s} + \\ + \Big(\left(m_1^2 + m_2^2 - m_3^2 - s\right)^2 s - \left(s + m_1^2(-1 + \cos\theta'^2)\right) \\ \left(m_1^4 + \left(-m_2^2 + m_3^2 + s\right)^2 - 2m_1^2(m_2^2 + s + m_3^2(-1 + 2\cos\theta'^2))\right)\Big)^{\frac{1}{2}}\Big].\end{aligned} \tag{6.10}$$

As argued before, $E_{1,1}$ and $E_{1,2}$ do not fulfill the on-shell condition (6.3) over the whole range of $\cos\theta'$ but only in particular regions. Plugging the solutions (6.7) into equation (6.3), it shows that $E_{1,2}$ is valid in the range

$$\cos\theta' < 0 \wedge E_3 \in [m_3; E_{3,\max}], \tag{6.11}$$

whereas solution $E_{1,1}$ has the scope of validity

$$\begin{aligned}&\left(\cos\theta' > 0 \wedge E_3 \in [m_3 \quad ; E'_{3,\max}]\right) \vee \\ &\left(\cos\theta' < 0 \wedge E_3 \in [E'_{3,\max}; E_{3,\max}]\right).\end{aligned} \tag{6.12}$$

$E'_{3,\max}$ herein is defined as

$$E'_{3,\max} := E_{3,\max}(\cos\theta' = 0) = \frac{-m_2^2 + m_3^2 + (m_1 - \sqrt{s})^2}{2\left(\sqrt{s} - m_1\right)}. \tag{6.13}$$

The scope of validity (6.11-6.12) is graphically shown in figure 6.2. Its physical interpretation is given in the following paragraph.

Once again, the results of parameterization 2 and 3 need not be treated separately. For parameterization 2 the scope of validity and the specific energies $E_{1,\max}$ and $E'_{1,\max}$ therein are found by exchanging $m_1 \leftrightarrow m_3$ and $E_1 \leftrightarrow E_3$. Moreover, starting from parameterization 2, applying the replacements $m_1 \to m_2$, $m_2 \to m_1$ and $\cos\theta' \to \cos\widetilde{\theta'}$, the results for parameterization 3 are obtained.

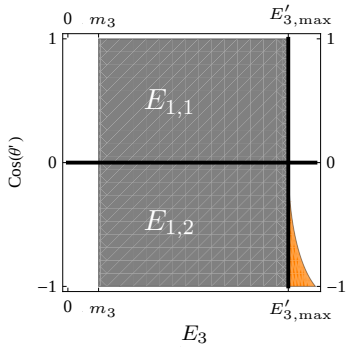

Figure 6.2: In the lower gray shaded area ($\cos\theta' < 0 \ \wedge \ E_3 < E'_{3,\max}$) the on-shell condition (6.3) is only fulfilled by solution $E_{1,2}$, in the upper area ($\cos\theta' > 0 \ \wedge \ E_3 < E'_{3,\max}$) only by $E_{1,1}$. The orange region with the curvy shape indicates the region where both solutions satisfy this condition.

Physical interpretation

The calculation before has shown that the 3-particle phase space is naturally divided into subregions in the E_3-$\cos\theta'$-plane (for parameterization 1). To understand this from the physics point of view, the kinematical constellations of the involved final state particles are discussed in the following, starting from small energies E_3:

- **case $\mathbf{E_3 = m_3}$:** Particle p_3 carries no momentum ($|\vec{p}_3| = 0$). Due to conservation of momentum particles p_1 and p_2 have momenta with the same norm $|\vec{p}_1| = |\vec{p}_2| = \sqrt{-m_1^2 + \frac{\left(m_1^2 - m_2^2 + \left(m_3 - \sqrt{s}\right)^2\right)^2}{4\left(m_3 - \sqrt{s}\right)^2}}$ but with opposite sign $\vec{p}_1 = -\vec{p}_2$. The two solutions $E_{1,1}$ and $E_{1,2}$ are degenerated in this scenario.
- **case $\mathbf{m_3 < E_3 < E'_{3,\max}}$:** In this case the energy of particle p_3 is below the specific threshold $E'_{3,\max}$. The value $E'_{3,\max}$ has the property that for any given pair of values ($E_3 < E'_{3,\max}$, $\cos\theta'$) a phase space configuration that respects the conservation of energy and momentum can be found. That is to say for all energies E_3 in this range and all angles θ' ($\measuredangle(\vec{p}_1, \vec{p}_3)$) appropriate four-vectors $\mathbf{p}_1$ and $\mathbf{p}_2$, which are compatible with the phase space constraints, can be chosen. Solution $E_{1,1}$ corresponds to the scenario in which the three-momenta of particle p_1 and p_3 lie in the same half-space and particle p_2 goes into the opposite direction. Consequently, one finds $0 \leq \cos\theta' \leq 1$ and $|\vec{p}_2| > |\vec{p}_1|, |\vec{p}_3|$. In contrast, the scenario with $\vec{p}_1$ and $\vec{p}_3$ being in different half-spaces and thus having $-1 \leq \cos\theta' < 0$ is related to solution $E_{1,2}$.
- **case $\mathbf{E_3 = E'_{3,\max}}$:** The special meaning of energy $E'_{3,\max}$ becomes evident when looking at solution $E_{1,1}$. For this solution and $E_3 = E'_{3,\max}$ particle p_1 carries no momentum ($|\vec{p}_1| = 0$), i. e. $E_1 = m_1$. Particles p_2 and p_3 have momenta with the same norm $|\vec{p}_2| = |\vec{p}_3| = \frac{\sqrt{\left(m_1 - m_2 - m_3 - \sqrt{s}\right)\left(m_1 + m_2 - m_3 - \sqrt{s}\right)\left(m_1 - m_2 + m_3 - \sqrt{s}\right)\left(m_1 + m_2 + m_3 - \sqrt{s}\right)}}{2\left(\sqrt{s} - m_1\right)}$ but with opposite sign $\vec{p}_2 = -\vec{p}_3$. As can easily be checked, $E'_{3,\max}$, as defined in equation (6.13), is equivalent to the energy of particle p_3 of this constellation.
- **case $\mathbf{E'_{3,\max} < E_3 < E_{3,\max}}$:** The energy of particle p_3 exceeds above the threshold $E'_{3,\max}$. $\vec{p}_1$ and $\vec{p}_2$ are situated in one half-space and $\vec{p}_3$ in the other. For a given value of E_3 only specific values of $\cos\theta'$ in the range $-1 \leq \cos\theta' \leq \cos\theta'_{\max} \leq 0$ are allowed. In other words, conservation of energy and momentum constrains the three-momenta of particles p_1 and p_2 to lie within a cone that points into the opposite direction of

$\vec{p}_3$. The higher the energy E_3 is, the narrower the cone must be. Consequently, $E_{3,\max}$ must be a function of $\cos\theta'$, as stated in equation 6.10.

- **case $\mathbf{E_3} = \mathbf{E}_{3,\max}$:** Particle p_3 has maximal energy $E_{3,\max}$, which depends on $\cos\theta'$. $E_{3,\max}(\cos\theta')$ takes its maximum at $\cos\theta' = -1$:

$$E_{3,\max}(\cos\theta' = -1) = \frac{-(m_1+m_2)^2 + m_3^2 + s}{2\sqrt{s}} \tag{6.14}$$

To which physical constellation does energy 6.14 of particle p_3 belong to? To answer this question, an independent derivation of the kinematic variables of the scenario in which particle p_3 has maximum energy will be given in the following. E_3 taking its maximum value, all the three-vectors are located in one line and thus $|\vec{p}_3| = |\vec{p}_1| + |\vec{p}_2|$. As $|\vec{p}_1|$ and $|\vec{p}_2|$ are a priori not known, neither is $|\vec{p}_3|$. To obtain an expression for $|\vec{p}_3|$ out of physical considerations, it is convenient to start with the ansatz $|\vec{p}_1| = a \cdot |\vec{p}_3|$ and $|\vec{p}_2| = (1-a) \cdot |\vec{p}_3|$ with $0 \leq a \leq 1$. Thereby the problem has reduced to finding an expression of a that maximizes $|\vec{p}_3|$. Employing this ansatz, the equation of conservation of energy reads

$$\sqrt{s} = E_1 + E_2 + E_3 = \sqrt{a^2 \cdot |\vec{p}_3|^2 + m_1^2} + \sqrt{(a-1)^2 \cdot |\vec{p}_3|^2 + m_2^2} + \sqrt{|\vec{p}_3|^2 + m_3^2}. \tag{6.15}$$

Solving this equation for $|\vec{p}_3|$ and maximizing this expression with respect to a is straight-forward in principal but still challenging because of the lengthy expressions. Eventually, the calculation shows that $|\vec{p}_3|$ and thus E_3 take its maximum value for

$$a = \frac{m_1}{m_1 + m_2}. \tag{6.16}$$

The idea why this may be considered as the correct solution can easily be understood: Inserting solution 6.16 into equation 6.15, one obtains:

$$\sqrt{s} = \sqrt{|\vec{p}_3|^2 + (m_1+m_2)^2} + \sqrt{|\vec{p}_3|^2 + m_3^2} \tag{6.17}$$

This, however, can be interpreted as the equation of conservation of energy of a three-particle final state with one massless particle at rest and two massive particles with masses $m_1 + m_2$ and m_3, respectively, both having momentum with the norm $|\vec{p}_3|$. This scenario is illustrated schematically in figure 6.3. It is evident that in this kinematic constellation E_3 is maximal and indeed is equivalent to expression 6.14.

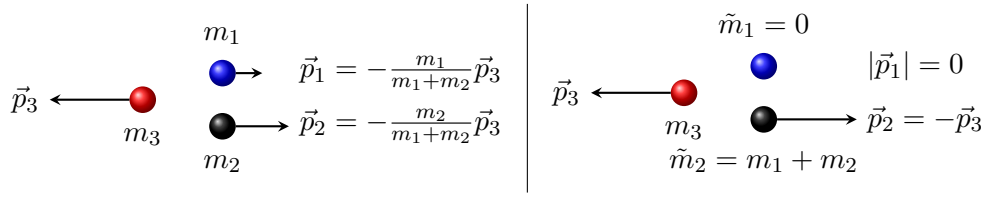

Figure 6.3: Determination of the maximal momentum / energy of particle p_3. The sketch of the kinematical situation on the left corresponds to the scenario with three massive particles. $|\vec{p}_3|$ is maximal when $\vec{p}_1 = a\,\vec{p}_3$ and $\vec{p}_1 = (a-1)\,\vec{p}_3$, where $a = \frac{m_1}{m_2+m_3}$ as defined in (6.16). The same value for the maximal energy is obtained much easier in the corresponding scenario illustrated on the right. Here particle p_1 is massless and particle p_2 has mass $\tilde{m}_2 = m_1 + m_2$.

6.3.2 Three massive particles, two particles having identical masses

The special case of a final state with three massive particles of which two have identical masses is considered separately in this paragraph, as this is the relevant kinematic scenario for the process $GG \to t\bar{t}Z$. Without loss of generality, particles p_1 and p_2 are chosen to have equal masses $m := m_1 = m_2$. The procedure of determining an expression for E_1 (for parameterization 1) in terms of the parameters of the phase space parameterization is of course similar to the one of the most general case and so are the obtained formulas. The corresponding terms of the two solutions $E_{1/2}$ 6.7 simplify to

$$A = -\left(E_3 - \sqrt{s}\right)\left(-m_3^2 + 2E_3\sqrt{s} - s\right), \tag{6.18a}$$

$$B = -2\left(E_3 - \sqrt{s}\right)^2 + 2(E_3^2 - m_3^2)\cos\theta'^2, \tag{6.18b}$$

$$\begin{aligned}\Delta = \left(E_3^2 - m_3^2\right)\Big[&-4m^2 s + \left(m_3^2 + s\right)^2 - 4E_3\sqrt{s}\left(-2m^2 + m_3^2 + s\right) - \\ &4m^2 m_3^2\cos\theta'^2 + 4E_3^2\left(s + m^2\left(-1 + \cos\theta'^2\right)\right)\Big].\end{aligned} \tag{6.18c}$$

Consequently, the specific energies $E_{3,\max}$ and $E'_{3,\max}$ read

$$\begin{aligned}E_{3,\max}(\cos\theta') = \frac{1}{2\left(s + m_1^2\left(-1 + \cos\theta'^2\right)\right)}\Big[&m_3^2\sqrt{s} + \sqrt{s}\left(-2m^2 + s\right) - \\ &- m\sqrt{\left(m_3^2 - s\right)^2 - \left(m_3^2 - s\right)\left(4m^2 + m_3^2 - s\right)\cos\theta'^2 + 4m^2 m_3^2\cos\theta'^4}\Big]\end{aligned} \tag{6.19}$$

and

$$E'_{3,\max} := E_{3,\max}(\cos\theta' = 0) = \frac{m_3^2 - 2m\sqrt{s} + s}{2\left(\sqrt{s} - m_1\right)}, \tag{6.20}$$

respectively. For the physical interpretation is referred to the preceding subsection.

6.3.3 Two massive particles with identical masses and one massless particle

The case considered in this paragraph appears for example in the process $GG \to t\bar{t}\gamma$. Its feature is a final state with one massless particle, which in the above notation is chosen to be p_3, and the remaining two having identical masses $m := m_1 = m_2$. For parameterization 1 the structure of the phase space stays the same as in the most general case, i. e. the phase space is still divided into subregions as depicted in figure 6.2. There are two solutions for E_1 having the structure of equations (6.7) with

$$A = -2E_3^2\sqrt{s} + 3E_3 s - s^{3/2}, \tag{6.21a}$$

$$B = 4E_3\sqrt{s} - 2s + 2E_3^2\left(-1 + \cos\theta'^2\right), \tag{6.21b}$$

$$\Delta = E_3^2\left[s\left(-4m^2 + s\right) - 4E_3\sqrt{s}\left(-2m^2 + s\right) + 4E_3^2\Big(s + m^2\left(-1 + \cos\theta'^2\right)\Big)\right]. \tag{6.21c}$$

$E_{3,\max}$ and $E'_{3,\max}$ reduce to

$$E_{3,\max}(\cos\theta') = \frac{\sqrt{s}\left(s - m\left(2m + \sqrt{s + (4m^2 - s)\cos\theta'^2}\right)\right)}{2\left(s + m^2\left(-1 + \cos\theta'^2\right)\right)} \tag{6.22}$$

$$E'_{3,\max} := E_{3,\max}(\cos\theta' = 0) = \frac{(\sqrt{s} - 2m)\sqrt{s}}{2(\sqrt{s} - m)}. \tag{6.23}$$

However, m_3 vanishing simplifies parameterizations 2 and 3 significantly. As mentioned above, the results for parameterization 2 are obtained by exchanging $E_1 \leftrightarrow E_3$ and $m_1 \leftrightarrow m_3$, the latter meaning setting $m = 0$ in this special case. From equation (6.22) one immediately sees, that $E_{1,\max} = \sqrt{s}/2$, independent of $\cos\theta'$. This means that in this parameterization the phase space does not decompose into separate regions. This matches with the fact that the on-shell condition (6.3) (or more easily seen in the explicit form (6.4)) is not a quadratic but a linear equation in E_3 for $m_3 = 0$. Hence, only one solution exists, namely

$$E_3 = \frac{2E_1\sqrt{s} - s}{2\left(E_1 - \sqrt{s} - \sqrt{E_1^2 - m^2}\cos\theta'\right)}, \tag{6.24}$$

which satisfies equation (6.3) over the whole parameter space.

6.3.4 Three massless particles

For completeness also the case of a final state with three massless particles $m_1 = m_2 = m_3 = 0$ is mentioned in this subsection. All the three parameterizations show a simple structure. The only solution of the mass shell condition (6.3) for parameterization 1, which is now linear in E_1, takes the form

$$E_1 = \frac{2E_3\sqrt{s} - s}{2(E_3 - \sqrt{s} - E_3\cos\theta')}, \tag{6.25}$$

which is valid in the whole parameter space ($0 \le E_3 < \sqrt{s}/2$). Similar results are obtained for parameterization 2 and 3.

6.4 Phase space integral

With the knowledge gathered in the previous section it is straight-forward to write down the actual phase space integral

$$R_{n=3}(s) \equiv \int \prod_{i=1}^{3} \frac{\mathrm{d}^3 p_i}{2E_i}\ \delta^{(4)}\left(\mathbf{p}_a + \mathbf{p}_b - \sum_{j=1}^{3}\mathbf{p}_j\right) \tag{6.26}$$

for a three-particle final state in concrete terms. Employing the identity

$$\frac{\mathrm{d}^3 p_i}{2E_i} = \mathrm{d}^4 p_i\ \delta\left(\mathbf{p}_i^2 - m_i^2\right)\theta(E_i) \tag{6.27}$$

the phase space integral (6.26) can be transformed into

$$R_3(s) = \int \frac{\mathrm{d}^3p_1\mathrm{d}^3p_3}{4E_1E_3}\ \theta\big(\sqrt{s}-E_1-E_3\big)\,\delta\big(\mathbf{p}_2^2-m_2^2\big) \tag{6.28}$$

and by switching to three-dimensional spherical coordinates

$$\mathrm{d}^3p_i = |\vec{p}_i|E_i\mathrm{d}E_i\mathrm{d}\Omega_i \tag{6.29}$$

further into

$$R_3(s) = \int \mathrm{d}E_1\mathrm{d}\Omega_1\mathrm{d}E_3\mathrm{d}\Omega_3\ \frac{1}{4}|\vec{p}_1||\vec{p}_3|\ \theta\big(\sqrt{s}-E_1-E_3\big)\,\delta\big(\mathbf{p}_2^2-m_2^2\big)\,. \tag{6.30}$$

Of course, for parameterization 3 one would rather eliminate the variables of particle p_3 than those of particle p_2 in step (6.28). One additional integration can be performed by making use of the property

$$\int \mathrm{d}x\ f(x)\ \delta(g(x)) = \sum_i \frac{f(x_i)}{|g'(x_i)|} \quad \text{with} \quad g(x_i)=0;\ g'(x_i) := \left.\frac{\partial g(x)}{\partial x}\right|_{x=x_i} \tag{6.31}$$

of the Dirac delta distribution. In order to do this one has however to solve the equation $\mathbf{p}_2^2 - m_2^2 = 0$, which is of course exactly the on-shell condition (6.3). As the solution of this equation was already discussed in section 6.3, we can directly go to the presentation of the phase space integral for each of the introduced parameterizations. Once again, at first the general case of a final state with three massive particles, all with different masses, is shown. After that, the special cases that are of interest for the physical analyzes in this thesis follow.

6.4.1 Three particles with different masses

The actual phase space integral for a three-particle final state with different masses in parameterization 1 (see section 6.3) reads

$$\begin{aligned}
R_3^{\mathrm{par}\,1}(s;&m_1,m_2,m_3) = \\
&-\frac{\pi}{2}\int_{-1}^{1}\mathrm{d}\cos\theta\int_0^{2\pi}\mathrm{d}\phi\int_0^{1}\mathrm{d}\cos\theta'\int_{m_3}^{E'_{3,\max}}\mathrm{d}E_3\ \frac{1}{D}\sqrt{E_1^2-m_1^2}\sqrt{E_3^2-m_3^2}\Big|_{E_1=E_{1,1}} \\
&+\frac{\pi}{2}\int_{-1}^{1}\mathrm{d}\cos\theta\int_0^{2\pi}\mathrm{d}\phi\int_{-1}^{0}\mathrm{d}\cos\theta'\int_{E'_{3,\max}}^{E_{3,\max}}\mathrm{d}E_3\ \frac{1}{D}\sqrt{E_1^2-m_1^2}\sqrt{E_3^2-m_3^2}\Big|_{E_1=E_{1,1}} \\
&-\frac{\pi}{2}\int_{-1}^{1}\mathrm{d}\cos\theta\int_0^{2\pi}\mathrm{d}\phi\int_{-1}^{0}\mathrm{d}\cos\theta'\int_{m_3}^{E_{3,\max}}\mathrm{d}E_3\ \frac{1}{D}\sqrt{E_1^2-m_1^2}\sqrt{E_3^2-m_3^2}\Big|_{E_1=E_{1,2}}\,,
\end{aligned} \tag{6.32}$$

where $E_{1,1}$ and $E_{1,1}$ are defined in equations (6.7) and (6.8), $E_{3,\max}$ in equation (6.10), $E'_{3,\max}$ in equation (6.13) and D takes the form

$$D := \frac{\partial(\mathbf{p}_2^2 - m_2^2)}{\partial E_1} = 2\left(E_3 - \sqrt{s} - \frac{E_1\sqrt{E_3^2 - m_3^2}\cos\theta'}{\sqrt{E_1^2 - m_1^2}}\right). \tag{6.33}$$

Note the relative signs in the phase space integral (6.32), which originate from the explicitly taken absolute value of D for the specific integrals. The explicit θ-function is dropped in (6.32), as the on-shell condition guarantees a positive energy of particle p_2 anyway. Furthermore, recall that $E_{1,1/2}$ is a function of $(E_3, \cos\theta')$ and the integration limit $E_{3,\max}$ depends on $\cos\theta'$. Exchanging $m_1 \leftrightarrow m_3$ and $E_1 \leftrightarrow E_3$ yields the phase space integrals for parameterization 2, while the integral for parameterization 3 is obtained by replacing $m_1 \to m_2$, $m_2 \to m_1$ and $\cos\theta' \to \cos\widetilde{\theta'}$ in the formulas of parameterization 2.

As the phase space integral has to be performed by means of numerical Monte Carlo techniques finally, it is more convenient and most of all more efficient to write the three separate integrals of (6.32) as only one integral of a sum of three terms introducing appropriate θ-step-functions to respect the original integration range. The phase space integral (6.32) then takes the form

$$\begin{aligned}
\tilde{R}_3^{\text{par }1}(s; m_1, m_2, m_3) = -\frac{\pi}{2}\int_{-1}^{1}\mathrm{d}\cos\theta\int_{0}^{2\pi}\mathrm{d}\phi\int_{-1}^{1}\mathrm{d}\cos\theta'\int_{m_3}^{E_{3,\max}}\mathrm{d}E_3 \\
\Bigg[\ \theta(E'_{3,\max} - E_3)\theta(+\cos\theta')\frac{1}{D}\sqrt{E_1^2 - m_1^2}\sqrt{E_3^2 - m_3^2}\Big|_{E_1=E_{1,1}} \\
-\theta(E_3 - E'_{3,\max})\theta(-\cos\theta')\frac{1}{D}\sqrt{E_1^2 - m_1^2}\sqrt{E_3^2 - m_3^2}\Big|_{E_1=E_{1,1}} \\
+\qquad\qquad \theta(-\cos\theta')\frac{1}{D}\sqrt{E_1^2 - m_1^2}\sqrt{E_3^2 - m_3^2}\Big|_{E_1=E_{1,2}}\Bigg].
\end{aligned} \tag{6.34}$$

6.4.2 Three massive particles, two particles having identical masses

For the case $m := m_1 = m_2$ the generic structure of the phase space integrals $R_3(s; m, m, m_3)$ is the same as given in equation (6.32) for the general case but with inserting the definitions (6.18) for $E_{1,1/2}$, (6.19) for $E_{3,\max}$ and (6.20) for $E'_{3,\max}$.

6.4.3 Two massive particles with identical masses and one massless particle

Particle p_3 being massless, the phase space integral for parameterization 1 still takes the form (6.32), where the formulas for $E_{1,1/2}$ are given in (6.21), those for $E_{3,\max}$ and $E'_{3,\max}$ in (6.22) and (6.23), respectively. However, the integrals for parameterization 2 reduces

to

$$R_3^{\text{par }2}(s;m,m,0) = -\frac{\pi}{2}\int_{-1}^{1}\mathrm{d}\cos\theta\int_{0}^{2\pi}\mathrm{d}\phi\int_{-1}^{1}\mathrm{d}\cos\theta'\int_{0}^{\sqrt{s}/2}\mathrm{d}E_1\;\frac{1}{D'}\sqrt{E_1^2-m_1^2}\;E_3\Big|_{E_3=E_3(E_1)}, \tag{6.35}$$

where $E_3(E_1)$ is defined in equation (6.24) and

$$D' := \frac{\partial(\mathbf{p}_1^2-m^2)}{\partial E_3} = 2\left(E_1-\sqrt{s}-\sqrt{E_1^2-m^2}\cos\theta'\right). \tag{6.36}$$

Parameterization 3 is obtained out of parameterization 2 as explained in subsection 6.4.1.

6.4.4 Three massless particles

All the particles being massless, the phase space integral simplifies to

$$R_3^{\text{par }1}(s;0,0,0) = -\frac{\pi}{2}\int_{-1}^{1}\mathrm{d}\cos\theta\int_{0}^{2\pi}\mathrm{d}\phi\int_{-1}^{1}\mathrm{d}\cos\theta'\int_{0}^{\sqrt{s}/2}\mathrm{d}E_3\;\frac{1}{D}E_1E_3\Big|_{E_1=E_1(E_3)}. \tag{6.37}$$

Herein the expression of $E_1(E_3)$ is given in equation (6.25) and

$$D := \frac{\partial(\mathbf{p}_2^2)}{\partial E_1} = 2\left(E_1-\sqrt{s}-E_1\cos\theta'\right). \tag{6.38}$$

7 Analysis of the general γtt vertex in the process $GG \to t\bar{t}\gamma$

The aim of this chapter is the examination of the general γtt vertex looking at the top quark pair production via gluon-gluon fusion plus additional photon radiation. However, before doing that, the process $GG \to t\bar{t}$, i. e. the same process without additional radiated photon in the final state, is considered in section 7.1.

7.1 Process $GG \to t\bar{t}$

In this section the calculation of the total reaction cross-section of the process $GG \to t\bar{t}$ is considered. The following Feynman-diagrams contribute to this process:

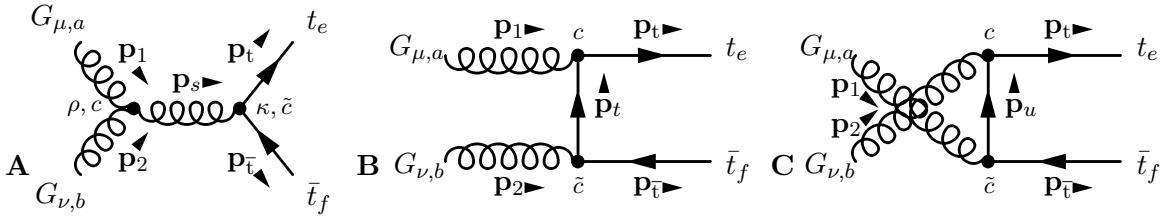

Figure 7.1: Feynman graphs for the process $GG \to t\bar{t}$. Greek indices at external particles and vertices refer to the Dirac structure, the color structure is denoted by Latin indices. Moreover, the momentum flow is indicated by small arrows next to the corresponding four-vectors (bold symbols).

Diagram **A** is usually referred to as the s-channel graph, diagrams **B** and **C** as the t- and u-channel graphs, respectively. The corresponding Feynman-amplitudes read:

$$\begin{aligned}\mathcal{M}_A = {} & \overline{u}_r(\mathbf{p}_\mathrm{t})\mathrm{i}g_s\gamma^\kappa(t^{\tilde{c}})_{ef}v_s(\mathbf{p}_{\bar{\mathrm{t}}})g_s f^{abc} \\ & [g^{\mu\nu}(\mathbf{p}_1-\mathbf{p}_2)^\rho + g^{\nu\rho}(\mathbf{p}_2+\mathbf{q}_s)^\mu + g^{\rho\mu}(-\mathbf{q}_s-\mathbf{p}_1)^\nu]\,\mathrm{i}D_{\mathrm{F},\rho\kappa}(\mathbf{q}_s)\delta_{c,\tilde{c}}\epsilon_{\mu,x}(\mathbf{p}_1)\epsilon_{\nu,y}(\mathbf{p}_2) \quad (7.1a)\end{aligned}$$

$$\mathcal{M}_B = \overline{u}_r(\mathbf{p}_\mathrm{t})\mathrm{i}g_s\gamma^\mu(t^a)_{ec}\mathrm{i}S_F(\mathbf{q}_t)\delta_{c,\tilde{c}}\mathrm{i}g_s\gamma^\nu(t^b)_{\tilde{c}f}v_s(\mathbf{p}_{\bar{\mathrm{t}}})\epsilon_{\mu,x}(\mathbf{p}_1)\epsilon_{\nu,y}(\mathbf{p}_2) \quad (7.1b)$$

$$\mathcal{M}_C = \overline{u}_r(\mathbf{p}_\mathrm{t})\mathrm{i}g_s\gamma^\nu(t^b)_{ec}\mathrm{i}S_F(\mathbf{q}_u)\delta_{c,\tilde{c}}\mathrm{i}g_s\gamma^\mu(t^a)_{\tilde{c}f}v_s(\mathbf{p}_{\bar{\mathrm{t}}})\epsilon_{\mu,x}(\mathbf{p}_1)\epsilon_{\nu,y}(\mathbf{p}_2) \quad (7.1c)$$

where the fermion spinors u_s and v_s carry an additional polarization index s. The scalar propagator $D_\mathrm{F}^{\mu\nu}(\mathbf{q})$ and the fermion propagator $S_F(\mathbf{q})$ are defined as

$$D_\mathrm{F}^{\mu\nu}(\mathbf{q}) = -\frac{1}{\mathbf{q}^2(+\mathrm{i}\epsilon)}g^{\mu\nu} \quad (7.2)$$

$$S_F(\mathbf{q}) = \frac{1}{\not{\mathbf{q}} - m_\mathrm{t}(+\mathrm{i}\epsilon)} = \frac{\not{\mathbf{q}} + m_\mathrm{t}}{\mathbf{q}^2 - m_\mathrm{t}^2(+\mathrm{i}\epsilon)}. \quad (7.3)$$

The gluon polarization vector is dentoted by $\epsilon_{\mu,x}$, the strong coupling constant by g_s. The $(t^c)_{ab}$ are the generators of the SU(3) group, f^{abc} correspond to the structure constants of the SU(3) group (see also section 3.1). Summation over repeated indices is understood.

The squared matrix element takes the form

$$\begin{aligned} |\mathcal{M}|^2 &= |\mathcal{M}_A + \mathcal{M}_B + \mathcal{M}_C|^2 \\ &= |\mathcal{M}_A|^2 + |\mathcal{M}_B|^2 + |\mathcal{M}_C|^2 + 2\,\mathcal{M}_A\mathcal{M}_B^\dagger + 2\,\mathcal{M}_A\mathcal{M}_C^\dagger + 2\,\mathcal{M}_B\mathcal{M}_C^\dagger, \end{aligned} \tag{7.4}$$

where the symbol † denotes hermitian conjugation. Since there are two gluons in the initial state with two physical polarizations and eight possible colors each, the squared matrix element, averaged over polarization and color of the incoming particles and summed over all polarizations and colors of the outgoing particles, reads

$$|\overline{\mathcal{M}}|^2 = \frac{1}{2^2 \cdot 8^2} \underbrace{\sum_{a,b,e,f}}_{\text{sum over color}} \underbrace{\sum_{s,r,x,y}}_{\text{sum over polarization}} |\mathcal{M}|^2. \tag{7.5}$$

To see how the procedure of the calculation as outlined in section 5.3 works, the explicit computing is performed for the part $|\overline{\mathcal{M}}_A|^2$ in the following. After starting with

$$\begin{aligned} |\overline{\mathcal{M}}_A|^2 =& \frac{1}{256} \sum_{a,b,e,f} \sum_{s,r,t} \mathcal{M}_A \mathcal{M}_A^\dagger \\ =& \frac{1}{256} g_s^4 \frac{1}{\mathbf{q}_s^4} \sum_{s,r} \overline{u}_r(\mathbf{p}_\mathrm{t}) \gamma_\rho v_s(\mathbf{p}_{\bar{\mathrm{t}}}) \overline{v}_s(\mathbf{p}_{\bar{\mathrm{t}}}) \gamma_{\tilde{\rho}} u_r(\mathbf{p}_\mathrm{t}) \\ & \left[g^{\mu\nu}(\mathbf{p}_1 - \mathbf{p}_2)^\rho + g^{\nu\rho}(\mathbf{p}_2 + \mathbf{q}_s)^\mu + g^{\rho\mu}(-\mathbf{q}_s - \mathbf{p}_1)^\nu\right] \\ & \left[g^{\tilde{\mu}\tilde{\nu}}(\mathbf{p}_1 - \mathbf{p}_2)^{\tilde{\rho}} + g^{\tilde{\nu}\tilde{\kappa}}(\mathbf{p}_2 + \mathbf{q}_s)^{\tilde{\mu}} + g^{\tilde{\rho}\tilde{\mu}}(-\mathbf{q}_s - \mathbf{p}_1)^{\tilde{\nu}}\right] \\ & \sum_{x,y} \epsilon_{\mu,x}(\mathbf{p}_1) \epsilon^*_{\tilde{\mu},x}(\mathbf{p}_1) \epsilon_{\nu,y}(\mathbf{p}_2) \epsilon^*_{\tilde{\nu},y}(\mathbf{p}_2) \\ & \sum_{a,b,e,f} (t^c)_{ef} f^{abc} (t^{\tilde{c}})_{fe} f^{ab\tilde{c}}, \end{aligned} \tag{7.6}$$

we employ the completeness relations

$$\sum_{s=1,2} u_s(\mathbf{p}) \overline{u}_s(\mathbf{p}) = \not{\mathbf{p}} + m \tag{7.7a}$$

$$\sum_{s=1,2} v_s(\mathbf{p}) \overline{v}_s(\mathbf{p}) = \not{\mathbf{p}} - m. \tag{7.7b}$$

The gluon polarization sum requires a more rigorous treatment. There are two possibilities to handle this problem: Either one uses the physical polarization sum (5.12) or instead employs the simple polarization sum

$$\sum_{\text{pol. } s} \epsilon_{\mu,s}(\mathbf{p}) \epsilon^*_{\nu,s}(\mathbf{p}) \to -g_{\mu\nu} \tag{7.8}$$

and additionally subtracts the contributions of the ghost graphs:

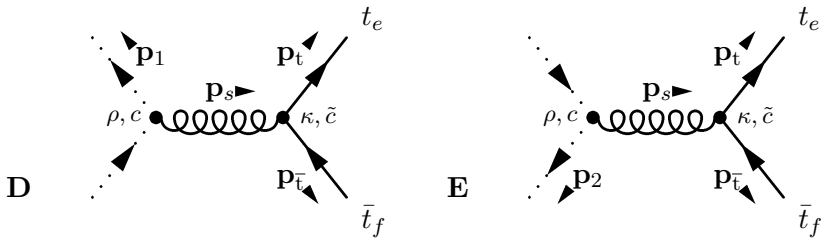

This is necessary to cancel the contributions of unphysical gluon polarizations due to the involved three-gluon vertex. As the second approach keeps the computational effort much lower compared to the first method, this approach is followed. The squared matrix element (7.4) thus receives the corrections of the ghost graphs to become

$$\begin{aligned}|\mathcal{M}|^2 &= |\mathcal{M}_A + \mathcal{M}_B + \mathcal{M}_C|^2 - |\mathcal{M}_D|^2 - |\mathcal{M}_E|^2 \\ &= |\mathcal{M}_A|^2 + |\mathcal{M}_B|^2 + |\mathcal{M}_C|^2 - |\mathcal{M}_D|^2 - |\mathcal{M}_E|^2 + 2\mathcal{M}_A\mathcal{M}_B^\dagger + 2\mathcal{M}_A\mathcal{M}_C^\dagger + 2\mathcal{M}_B\mathcal{M}_C^\dagger.\end{aligned} \tag{7.9}$$

The amplitudes for the ghosts graph read:

$$\mathcal{M}_D = \overline{u}_r(\mathbf{p}_\mathrm{t})\mathrm{i}g_s\gamma^\nu(t^c)_{ef}v_s(\mathbf{p}_{\bar{\mathrm{t}}})\left(-g_s f^{abc}\mathbf{p}_1^\mu\right)\left(-\mathrm{i}\frac{g_{\mu\nu}}{\mathbf{q}_s^2}\delta_{c\tilde{c}}\right) \tag{7.10a}$$

$$\mathcal{M}_E = \overline{u}_r(\mathbf{p}_\mathrm{t})\mathrm{i}g_s\gamma^\nu(t^c)_{ef}v_s(\mathbf{p}_{\bar{\mathrm{t}}})\left(-g_s f^{abc}\mathbf{p}_2^\mu\right)\left(-\mathrm{i}\frac{g_{\mu\nu}}{\mathbf{q}_s^2}\delta_{c\tilde{c}}\right) \tag{7.10b}$$

Going back to the calculation of $|\overline{\mathcal{M}}_A|^2$, equation (7.6) becomes

$$\begin{aligned}|\overline{\mathcal{M}}_A|^2 =& \frac{1}{256}g_s^4\frac{1}{\mathbf{q}_s^4}\,\mathrm{Tr}\left[(\not{\mathbf{p}}_\mathrm{t} + m_\mathrm{t})\gamma_\rho(\not{\mathbf{p}}_{\bar{\mathrm{t}}} - m_\mathrm{t})\gamma_{\tilde{\rho}}\right] \\ &\left[g^{\mu\nu}(\mathbf{p}_1 - \mathbf{p}_2)^\rho + g^{\nu\rho}(\mathbf{p}_2 + \mathbf{q}_s)^\mu + g^{\rho\mu}(-\mathbf{q}_s - \mathbf{p}_1)^\nu\right] \\ &\left[g^{\tilde{\mu}\tilde{\nu}}(\mathbf{p}_1 - \mathbf{p}_2)^{\tilde{\rho}} + g^{\tilde{\nu}\tilde{\kappa}}(\mathbf{p}_2 + \mathbf{q}_s)^{\tilde{\mu}} + g^{\tilde{\rho}\tilde{\mu}}(-\mathbf{q}_s - \mathbf{p}_1)^{\tilde{\nu}}\right] \\ &g_{\mu\tilde{\mu}}g_{\nu\tilde{\nu}}\sum_{a,b,e,f}(t^c)_{ef}(t^{\tilde{c}})_{fe}f^{abc}f^{ab\tilde{c}},\end{aligned} \tag{7.11}$$

having performed the polarization sums, as discussed above. In the next step the color factor, that is the sum in the last line, is evaluated. For this purpose, the identities

$$f^{acd}f^{bcd} = C_2(G)\delta^{ab} = N \tag{7.12a}$$

$$t^a t^a = C_2(r)\cdot\mathbb{1} \tag{7.12b}$$

with

$$C_2(G) = N = 3 \tag{7.13a}$$

$$C_2(r = N) = \frac{N^2 - 1}{2N} = \frac{4}{3} \tag{7.13b}$$

in SU($N = 3$) for QCD are useful. Thus, one obtains

$$\sum_{a,b,e,f}(t^c)_{ef}(t^{\tilde{c}})_{fe}f^{abc}f^{ab\tilde{c}} = \sum_{e,f}(t^c)_{ef}(t^{\tilde{c}})_{fe}\cdot 3\,\delta^{c,\tilde{c}} = \mathrm{Tr}[t^c t^c]\cdot 3 = \frac{4}{3}\,\mathrm{Tr}[\mathbb{1}]\cdot 3 = 12. \tag{7.14}$$

Now the Dirac trace in equation (7.11) has to be calculated. Employing the linearity of the trace and numerator algebra for Dirac matrices (see e. g. Ref. [44]), one yields

$$\mathrm{Tr}\left[(\not{\mathbf{p}}_{\mathrm{t}} + m_{\mathrm{t}})\gamma_\rho(\not{\mathbf{p}}_{\bar{\mathrm{t}}} - m_{\mathrm{t}})\gamma_{\tilde{\rho}}\right] = 4\left(\mathbf{p}_{\mathrm{t}\,\rho}\mathbf{p}_{\bar{\mathrm{t}}\,\tilde{\rho}} + \mathbf{p}_{\mathrm{t}\,\tilde{\rho}}\mathbf{p}_{\bar{\mathrm{t}}\,\rho} - g_{\rho,\tilde{\rho}}\ \mathbf{p}_{\mathrm{t}}\cdot\mathbf{p}_{\bar{\mathrm{t}}} - g_{\rho,\tilde{\rho}}\ m_{\mathrm{t}}^2\right), \tag{7.15}$$

where the four-vector dot-product

$$\mathbf{p}\cdot\mathbf{q} \equiv \mathbf{p}^\mu\mathbf{q}_\mu = \mathbf{p}_\mu\mathbf{q}^\mu \tag{7.16}$$

is introduced. Inserting (7.14) and (7.15) into equation (7.11) and contracting all Lorentz-indices we find for on-shell external particles, i. e. $\mathbf{p}_{1/2}^2 = 0$ and $\mathbf{p}_{\mathrm{t}/\bar{t}}^2 = m_{\mathrm{t}}$, and after algebraic simplification

$$\begin{aligned}|\overline{\mathcal{M}}_A|^2 = \frac{3g_s^4}{8\mathbf{q}_s^4}\Big[&3\mathbf{p}_1\cdot\mathbf{p}_2(\mathbf{p}_{\mathrm{t}}\cdot\mathbf{p}_{\bar{\mathrm{t}}} + m_{\mathrm{t}}^2) + \mathbf{p}_2\cdot\mathbf{p}_{\bar{\mathrm{t}}}(2\mathbf{p}_2\cdot\mathbf{p}_{\mathrm{t}} - \mathbf{p}_{\mathrm{t}}\cdot\mathbf{q}_s)\\ &- \mathbf{p}_1\cdot\mathbf{p}_{\bar{\mathrm{t}}}(3\mathbf{p}_2\cdot\mathbf{p}_{\mathrm{t}} + \mathbf{p}_{\mathrm{t}}\cdot\mathbf{q}_s) + \mathbf{p}_1\cdot\mathbf{p}_{\mathrm{t}}(2\mathbf{p}_1\cdot\mathbf{p}_{\bar{\mathrm{t}}} - 3\mathbf{p}_2\cdot\mathbf{p}_{\bar{\mathrm{t}}} - \mathbf{p}_{\bar{\mathrm{t}}}\cdot\mathbf{q}_s)\\ &- \mathbf{p}_{\bar{\mathrm{t}}}\cdot\mathbf{q}_s(\mathbf{p}_2\cdot\mathbf{p}_{\mathrm{t}} + 2\mathbf{p}_{\mathrm{t}}\cdot\mathbf{q}_s) - (\mathbf{p}_{\mathrm{t}}\cdot\mathbf{p}_{\bar{\mathrm{t}}} + 3m_{\mathrm{t}}^2)(\mathbf{p}_1\cdot\mathbf{q}_s + \mathbf{p}_2\cdot\mathbf{q}_s + \mathbf{q}_s^2)\Big].\end{aligned} \tag{7.17}$$

The next item on the agenda is to insert the scalar products in terms the phase space parameterization. Since there are two particles in the final state, one variable is sufficient for the phase space parameterization (cf. section 6.2). This parameter is chosen to be the angle $\theta = \measuredangle(\vec{p}, \vec{p}_{\mathrm{t}})$, that is the angle between the collision axis and the axis of the outgoing particles (see figure 7.2).

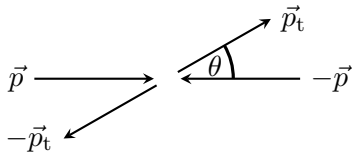

Figure 7.2: Definition of the angle $\theta = \measuredangle(\vec{p}, \vec{p}_{\mathrm{t}})$.

In the COM-frame the four-vectors of the external particles read

$$\mathbf{p}_1 = \begin{pmatrix}|\vec{p}|\\ \vec{p}\end{pmatrix},\ \mathbf{p}_2 = \begin{pmatrix}|\vec{p}|\\ -\vec{p}\end{pmatrix},\ \mathbf{p}_{\mathrm{t}} = \begin{pmatrix}E_{\mathrm{t}}\\ \vec{p}_{\mathrm{t}}\end{pmatrix},\ \text{ and } \mathbf{p}_{\bar{\mathrm{t}}} = \begin{pmatrix}E_{\mathrm{t}}\\ -\vec{p}_{\mathrm{t}}\end{pmatrix},$$

with $|\vec{p}| = \sqrt{s}/2$ and $E_{\mathrm{t}}^2 = |\vec{p}_{\mathrm{t}}|^2 + m_{\mathrm{t}}^2 = |\vec{p}|^2$. Hence, the scalar products involving external particles take the form

$$\begin{aligned}\mathbf{p}_1\cdot\mathbf{p}_2 &= \frac{s}{2} & \mathbf{p}_2\cdot\mathbf{p}_{\mathrm{t}} &= \frac{s}{4} + |\vec{p}||\vec{p}_{\mathrm{t}}|\cos\theta\\ \mathbf{p}_1\cdot\mathbf{p}_{\mathrm{t}} &= \frac{s}{4} - |\vec{p}||\vec{p}_{\mathrm{t}}|\cos\theta & \mathbf{p}_2\cdot\mathbf{p}_{\bar{\mathrm{t}}} &= \frac{s}{4} - |\vec{p}||\vec{p}_{\mathrm{t}}|\cos\theta\\ \mathbf{p}_1\cdot\mathbf{p}_{\bar{\mathrm{t}}} &= \frac{s}{4} + |\vec{p}||\vec{p}_{\mathrm{t}}|\cos\theta & \mathbf{p}_{\mathrm{t}}\cdot\mathbf{p}_{\bar{\mathrm{t}}} &= \frac{s}{2} - m_{\mathrm{t}}^2.\end{aligned}$$

All residual scalar products are computed by replacing $\mathbf{q}_s$ with $\mathbf{p}_1 + \mathbf{p}_2$ and making use of the linearity of the scalar product. Consequently, inserting the scalar products, expression

(7.17) reduces significantly to

$$|\overline{\mathcal{M}}_A|^2 = \frac{3g_s^4}{64s}\left(11s + 32m_\mathrm{t}^2 + 5(s - m_\mathrm{t}^2)\cos^2\theta\right). \tag{7.18}$$

The calculation of the remaining squared diagrams follows the same approach. Thus, only the final result for the whole squared matrix element (7.9) is stated:

$$\begin{aligned}|\overline{\mathcal{M}}|^2 =& \frac{g_s^4\left(36m_\mathrm{t}^2 - 23s + 9\left(4m_\mathrm{t}^2 - s\right)\cos(2\theta)\right)}{192s\left(4m_\mathrm{t}^2 + s + \left(4m_\mathrm{t}^2 - s\right)\cos(2\theta)\right)^2} \\ &\cdot\left(176m_\mathrm{t}^4 - 56m_\mathrm{t}^2 s - 5s^2 + 4\left(-16m_\mathrm{t}^4 + s^2\right)\cos(2\theta) + \left(-4m_\mathrm{t}^2 + s\right)^2\cos(4\theta)\right).\end{aligned} \tag{7.19}$$

The computation of the color factor for each squared diagram can be found in appendix A. The differential cross-section then reads:

$$\frac{\mathrm{d}\sigma}{\mathrm{d}\cos\theta} = \frac{1}{32\pi s^2}\sqrt{(s - 4m_\mathrm{t})s}\;|\overline{\mathcal{M}}|^2 \tag{7.20}$$

Introducing the Mandelstam variables

$$s = \mathbf{q}_s^2 = (\mathbf{p}_a + \mathbf{p}_b)^2 = (\mathbf{p}_t + \mathbf{p}_{\bar{t}})^2 \tag{7.21a}$$

$$t = \mathbf{q}_t^2 = (\mathbf{p}_\mathrm{t} - \mathbf{p}_a)^2 = (\mathbf{p}_b - \mathbf{p}_{\bar{t}})^2 = m_\mathrm{t}^2 - \frac{s}{2} + \frac{1}{2}\sqrt{s - 4m_\mathrm{t}^2}\sqrt{s}\cos\theta \tag{7.21b}$$

$$u = \mathbf{q}_u^2 = (\mathbf{p}_a - \mathbf{p}_{\bar{t}})^2 = (\mathbf{p}_t - \mathbf{p}_b)^2 = m_\mathrm{t}^2 - \frac{s}{2} - \frac{1}{2}\sqrt{s - 4m_\mathrm{t}^2}\sqrt{s}\cos\theta \tag{7.21c}$$

with the property

$$s + t + u = \sum_{\text{external particles } i} m_i^2 \quad = 2\,m_\mathrm{t}^2 \tag{7.22}$$

and considering the massless limit $m_\mathrm{t} \to 0$ the familiar result (cf. e. g. Ref. [44])

$$\frac{\mathrm{d}\sigma}{\mathrm{d}t} = \frac{g_s^4}{96\pi s^2}\left(\frac{u}{t} + \frac{t}{u} - \frac{9}{4}\left(\frac{t^2 + u^2}{s^2}\right)\right) \tag{7.23}$$

is reproduced.

The differential cross-section (7.20) can be integrated analytically to obtain the total reaction cross-section. It is remarked at this point that the results for the process $GG \to t\bar{t}$ are independent of the decay width of the top quark for a treatment of the decay width as discussed in section 5.3 because the two involved momenta $\mathbf{p}_t$ and $\mathbf{p}_u$ are both timelike ($\mathbf{p}_{t/u}^2 < 0$).

7.2 Process $GG \to t\bar{t}\gamma$

7.2.1 Calculation neglecting the top quark width

In this section the process $GG \to t\bar{t}\gamma$ is considered, that is to say the process of the previous section but with additional photon radiation. The eight Feynman graphs sketched

in figure 7.3 (diagram **A1-C3**) contribute to this process. At first the top quark decay width is neglected. Then we are allowed to employ the simple polarization sum (7.8) for the external gluons if the contributions of the ghost diagrams (diagrams **D1-E2** of figure 7.3) are subtracted. The amplitudes of all Feynman diagrams are listed in appendix B.1. The summation over the fermion polarization is accomplished the same way as in equations (7.7) of the previous section. For the summation of the photon polarization the simple polarization sum (7.8) may be used, too, as long as the decay width is set to zero. As the additional radiated photon does not affect the color structure of the involved graphs, the color factors computed in section 7.1 can be adopted. For example any amplitude involving two **A**-graphs, such as $|\mathcal{M}_{A1}|^2$ or $\mathcal{M}_{A1}\mathcal{M}_{A2}^{\dagger}$, has the same color factor as the squared matrix element $|\mathcal{M}_A|^2$ of section 7.1. Analogously, any amplitude involving one of the **B**-graphs and one of the **C**-graphs, like $\mathcal{M}_{B1}\mathcal{M}_{C2}^{\dagger}$, multiplies the color factor of the $\mathcal{M}_B\mathcal{M}_C^{\dagger}$ graph of the process $GG \to t\bar{t}$ and so on for the remaining terms. The computation of the Dirac traces, the contracting and the analytical simplification of the obtained expression for the squared matrix element is once more accomplished by `FeynCalc` / `Mathematica`.

In the next step the scalar products are written in terms of the phase space parameterization. Referring to the notation introduced in section 6.3 we relate $\mathbf{p}_a \mathrel{\widehat{=}} \mathbf{p}_1$, $\mathbf{p}_b \mathrel{\widehat{=}} \mathbf{p}_2$, $\mathbf{p}_1 \mathrel{\widehat{=}} \mathbf{p}_t$, $\mathbf{p}_2 \mathrel{\widehat{=}} \mathbf{p}_{\bar{\mathrm{t}}}$ and $\mathbf{p}_3 \mathrel{\widehat{=}} \mathbf{k}$. The scalar products involving external particles for phase space parameterization 1 and 2 (see section 6.3) take the form:

$$\begin{aligned}
\mathbf{p}_1 \cdot \mathbf{p}_2 &= \frac{s}{2} & \mathbf{p}_2 \cdot \mathbf{p}_{\mathrm{t}} &= \frac{\sqrt{s}}{2} E_{\mathrm{t}} + \vec{p} \cdot \vec{p}_{\mathrm{t}} \\
\mathbf{p}_1 \cdot \mathbf{p}_{\mathrm{t}} &= \frac{s}{2} E_{\mathrm{t}} - \vec{p} \cdot \vec{p}_{\mathrm{t}} & \mathbf{p}_2 \cdot \mathbf{p}_{\bar{\mathrm{t}}} &= \frac{s}{2} - \frac{\sqrt{s}}{2}(E_{\mathrm{t}} + E_{\mathrm{k}}) - \vec{p} \cdot \vec{p}_{\mathrm{t}} - \vec{p} \cdot \vec{k} \\
\mathbf{p}_1 \cdot \mathbf{p}_{\bar{\mathrm{t}}} &= \frac{s}{2} - \frac{\sqrt{s}}{2}(E_{\mathrm{t}} + E_{\mathrm{k}}) + \vec{p} \cdot \vec{p}_{\mathrm{t}} + \vec{p} \cdot \vec{k} & \mathbf{p}_2 \cdot \mathbf{p}_{\mathrm{k}} &= \frac{\sqrt{s}}{2} E_{\mathrm{k}} + \vec{p} \cdot \vec{k} \\
\mathbf{p}_1 \cdot \mathbf{p}_{\mathrm{k}} &= \frac{\sqrt{s}}{2} E_{\mathrm{k}} - \vec{p} \cdot \vec{k} & \mathbf{p}_{\mathrm{t}} \cdot \mathbf{p}_{\bar{\mathrm{t}}} &= E_{\mathrm{t}}(\sqrt{s} - E_{\mathrm{k}}) - m_{\mathrm{t}}^2 + \vec{p} \cdot \vec{k},
\end{aligned}$$

with

$$\begin{aligned}
\vec{p} \cdot \vec{p}_{\mathrm{t}} &= \frac{\sqrt{s}}{2} \sqrt{E_{\mathrm{t}}^2 - m_{\mathrm{t}}} \cos\theta \\
\vec{p} \cdot \vec{k} &= \frac{\sqrt{s}}{2} E_{\mathrm{k}} \left(\sin\theta \sin\theta' \cos\phi + \cos\theta \cos\theta' \right) \\
\vec{p}_{\mathrm{t}} \cdot \vec{k} &= \sqrt{E_{\mathrm{t}}^2 - m_{\mathrm{t}}^2}\, E_{\mathrm{k}} \cos\theta'.
\end{aligned}$$

Once again, to calculate the remaining scalar products the four-vectors involved in the propagators are expressed in terms of the external momenta:

$$\begin{aligned}
\mathbf{q}_s &= \mathbf{p}_1 + \mathbf{p}_2 & & \\
\mathbf{q}_t &= \mathbf{p}_{\mathrm{t}} - \mathbf{p}_1 & \mathbf{q}_t' &= \mathbf{p}_{\mathrm{t}} - \mathbf{p}_1 + \mathbf{k} \\
\mathbf{q}_u &= \mathbf{p}_{\mathrm{t}} - \mathbf{p}_2 & \mathbf{q}_u' &= \mathbf{p}_{\mathrm{t}} - \mathbf{p}_2 + \mathbf{k} \\
\mathbf{p}_{\mathrm{t}}' &= \mathbf{p}_{\mathrm{t}} + \mathbf{k} & \mathbf{p}_{\bar{\mathrm{t}}}' &= \mathbf{p}_{\bar{\mathrm{t}}} + \mathbf{k}
\end{aligned}$$

Having done these replacements for the scalar products, it is time to perform the phase space integral as discussed in subsection 6.4.3. As argued in section 5.3, a cut of the minimal energy of the radiated photon $E_{\mathrm{k,\,min}}$ has to be applied, which is chosen to be

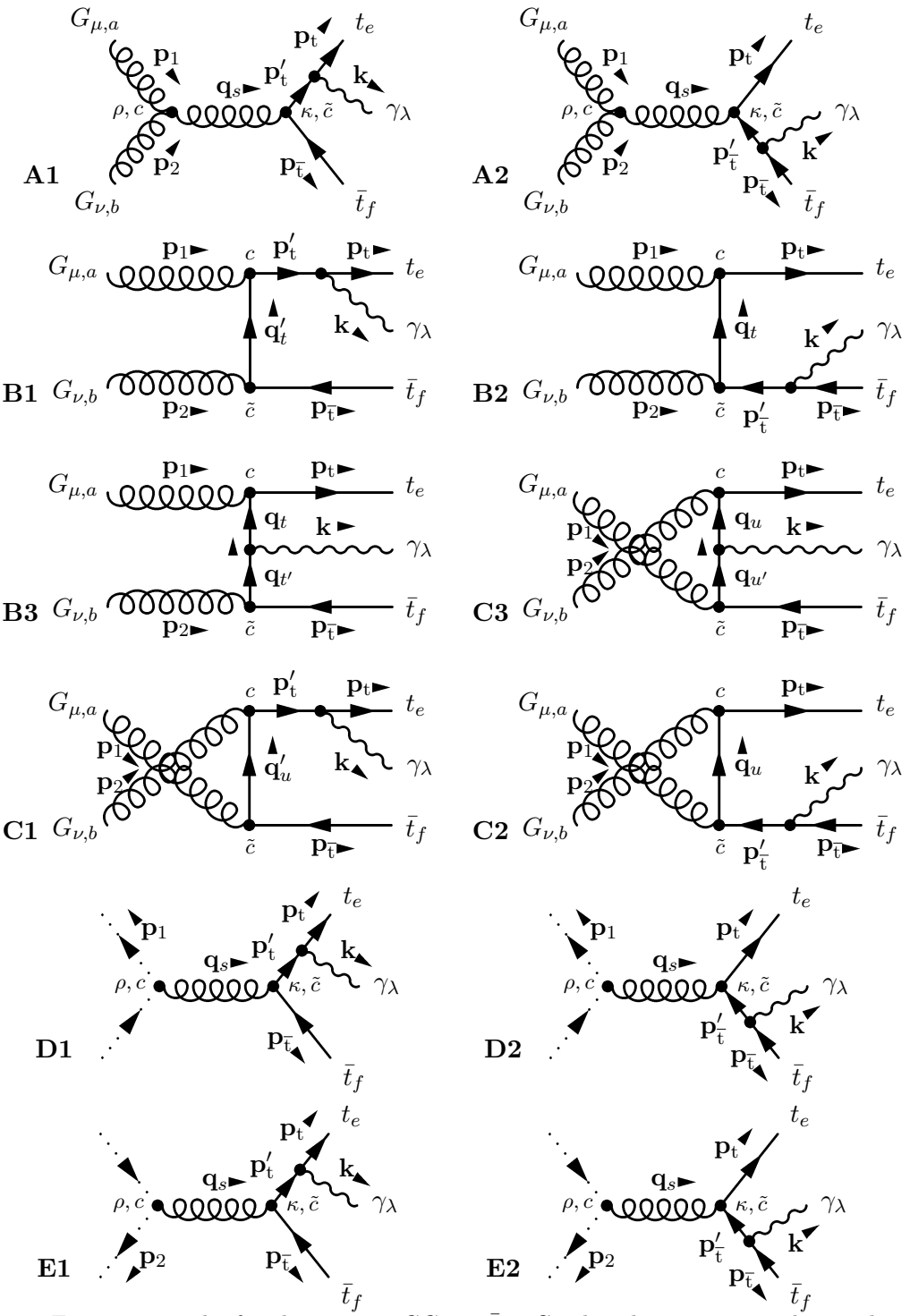

Figure 7.3: Feynman graphs for the process $GG \to t\bar{t}\gamma$. Greek indices at external particles and vertices refer to the Dirac structure, the color structure is denoted by roman indices. Moreover, the momentum flow is indicated by small arrows next to the corresponding four-vectors (bold symbols).

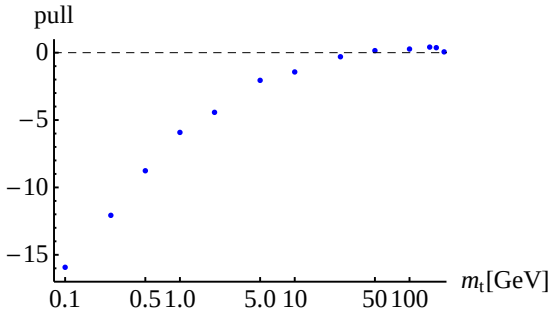

Figure 7.4: Pull between the calculation approach without any substitution of integration variables and a more sophisticated and reliable method, which yields the correct results, as a function of the top quark mass at a center-of-mass energy of $\sqrt{s} = 1.0$ TeV.

$E_{\mathrm{k,\,min}} = 5$ GeV. It is furthermore convenient to replace the integral $\int_0^{2\pi} \mathrm{d}\phi$ in favor of $2\int_0^{\pi} \mathrm{d}\phi$, which is possible since the integrand is a function of $\cos\phi$. At first we decide to do the integration in terms of phase space parameterization 1. However, it shows that the numeric integration converges badly for top quark masses $m_\mathrm{t} \ll s$. To stress this statement the pull, defined as

$$\mathrm{pull}(\sigma_a, s_a; \sigma_b, s_b) := \frac{\sigma_a - \sigma_b}{\sqrt{s_a^2 + s_b^2}}, \tag{7.24}$$

where σ is the estimated value for the cross-section and s its estimated error, is considered. As obvious from the definition (7.24), this quantity should be in the order of one in case of consistent results of both calculation approaches a and b. The pull of the cross-section calculated with two different methods is plotted in figure 7.4 as a function of m_t for a center-of-mass energy of $\sqrt{s} = 1.0$ TeV. The first method employs just the phase space integral for parameterization 1 as stated in subsection 6.4.3 without any substitution of integration variables. The `VEGAS` integrator gives an estimate of the relative error of 10^{-3} for each data point. The second method uses a more sophisticated approach, which will be derived later on. As will be seen then, the results obtained with this method are reliable. As is obvious from figure 7.4, the computed values for the cross-section employing the simple method show a systematic deviation from the correct result. The values are too small; the smaller the top quark mass, the more severe the discrepancy. The Monte Carlo integrator significantly underestimates the integral and gives an error estimate which is much too small. To understand the reason for that, recall the generic structure of the propagators involved in bremsstrahlung diagrams, as discussed in section 5.3. In that section it was seen that the denominator of the propagators may become very small in specific phase space regions. In addition, the discussion of the basic principals of Monte Carlo integration in section 4.3 implies that such quasi-singularities are problematic and give rise to convergence problems. There it is also discussed that one may overcome these problematics by virtue of adequate substitutions of integration variables. In fact, taking a closer look at the Feynman diagrams 7.3, one notices that six problematic propagators with different momenta occur. As a consequence each term is factorizable near its quasi-singularity in a different coordinate system. In other words, there is no substitution where all the terms factorize at the same time. As argued in section 4.3, this is however exactly the motivation for the multi-channel Monte Carlo approach.

In the following paragraph the mathematical structure of the denominators near the problematic regions is analyzed with the aim of finding appropriate parameterizations for each quasi-pol. This knowledge will eventually be used to implement a multi-channel Monte Carlo environment in the programming language `C` to obtain a better convergent phase space integration with the `VEGAS` integrator.

Appropriate parameterization of the quasi-singularities

Although six propagators with different momenta are encountered in the Feynman amplitudes (see figure 7.3), two denominators each can be grouped together to be described by the same set of coordinates, however, still favoring a distinct substitution in these coordinate systems. We begin with the analysis of the asymptotic behavior near the quasi-singularities of the propagator with momentum $\mathbf{p}'_{\mathrm{t}} = \mathbf{p}_{\mathrm{t}} + \mathbf{k}$, as occurring in graphs $\mathcal{M}_{A1}$, $\mathcal{M}_{B1}$ and $\mathcal{M}_{C1}$. Its denominator takes the form

$$(\mathbf{p}_{\mathrm{t}} + \mathbf{k})^2 - m_{\mathrm{t}}^2 = 2\mathbf{p}_{\mathrm{t}} \cdot \mathbf{k} = 2E_{\mathrm{k}} \left(E_{\mathrm{t}} - \sqrt{E_{\mathrm{t}}^2 - m_{\mathrm{t}}^2} \cos\theta' \right). \tag{7.25}$$

This expression becomes small for small values of E_{k} and in the case $E_{\mathrm{t}} \gg m_{\mathrm{t}}$ for $\cos\theta' \to 1$ (cf. section 5.3). As for a specific phase space integration m_{t} is fixed, the ratio $m_{\mathrm{t}}/E_{\mathrm{t}}$ is smallest for the maximum possible value of E_{t}, i. e. for $E_{\mathrm{t}} = \sqrt{s}/2$. Thus, the asymptotic behavior near the quasi-singularities of denominator (7.25) can be factorized into

$$\mathbf{p}_{\mathrm{t}}'^2 - m_{\mathrm{t}}^2 \sim 2E_{\mathrm{k}} \left(E_{\mathrm{t}} - \sqrt{E_{\mathrm{t}}^2 - m_{\mathrm{t}}^2} \cos\theta' \right) \Big|_{E_{\mathrm{t}}=\sqrt{s}/2} = E_{\mathrm{k}} \left(\sqrt{s} - \sqrt{s - 4m_{\mathrm{t}}^2} \cos\theta' \right). \tag{7.26}$$

Analogously, one finds for the propagator involving momentum $\mathbf{p}'_{\bar{\mathrm{t}}} = \mathbf{p}_{\bar{\mathrm{t}}} + \mathbf{k}$

$$2\mathbf{p}_{\bar{\mathrm{t}}} \cdot \mathbf{k} = \left(\frac{\sqrt{s}}{2} - E_{\mathrm{t}} - E_{\mathrm{k}} \right) E_{\mathrm{k}} + \left(\vec{p}_{\mathrm{t}} + \vec{k} \right) \cdot \vec{k} = \left(\frac{\sqrt{s}}{2} - E_{\mathrm{t}} \right) E_{\mathrm{k}} + \sqrt{E_{\mathrm{t}}^2 - m_{\mathrm{t}}^2} E_{\mathrm{k}} \cos\theta' \tag{7.27}$$

and asymptotically

$$\mathbf{p}_{\bar{\mathrm{t}}}'^2 - m_{\mathrm{t}}^2 \quad \sim \quad 2\mathbf{p}_{\bar{\mathrm{t}}} \cdot \mathbf{k} \Big|_{E_{\mathrm{t}}=\sqrt{s}/2} = E_{\mathrm{k}} \left(\sqrt{s} + \sqrt{s - 4m_{\mathrm{t}}^2} \cos\theta' \right). \tag{7.28}$$

Therefore, an appropriate parameterization for the denominators with momenta $\mathbf{p}'_{\mathrm{t}}$ and $\mathbf{p}'_{\bar{\mathrm{t}}}$ should involve the parameters E_{k} and $\cos\theta'$, as does parameterization 1 introduced in section 6.3. The next term to consider is the propagator involving momentum $\mathbf{q}_t = \mathbf{p}_{\mathrm{t}} - \mathbf{p}_1$, which occurs in diagrams $\mathcal{M}_{B2}$ and $\mathcal{M}_{B3}$. Writting the denominator of this propagator explicitly, one obtains

$$\mathbf{q}_t^2 - m_{\mathrm{t}}^2 = -2\mathbf{p}_{\mathrm{t}} \cdot \mathbf{p}_1 = -2E_{\mathrm{t}} \frac{\sqrt{s}}{2} + 2\vec{p}_{\mathrm{t}} \cdot \vec{p} = -\sqrt{s} E_{\mathrm{t}} \left(1 - \sqrt{1 - \frac{m_{\mathrm{t}}^2}{E_{\mathrm{t}}^2}} \cos\theta \right). \tag{7.29}$$

This denominator is problematic either if E_{t} is minimal, that is $E_{\mathrm{t}} = m_{\mathrm{t}}$, or if E_{t} is maximal, that is $E_{\mathrm{t}} = \sqrt{s}/2$, because then the second factor becomes small for $\cos\theta \to 1$.

Ch.	involved momentum	asymptotic behavior of quasi-singularity	phase space parameter.	
1, 2	$\mathbf{p}'_{\mathrm{t}}$, $\mathbf{p}'_{\bar{\mathrm{t}}}$	$E_{\mathrm{k}} \cdot \left(\sqrt{s} \pm \sqrt{s - 4m_{\mathrm{t}}^2}\cos\theta'\right)$	parameter. 1 E_{k}, θ, θ', ϕ	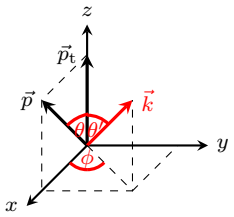
3, 4	$\mathbf{q}_t$, $\mathbf{q}_u$	$E_{\mathrm{t}} \cdot \left(\sqrt{s} \pm \sqrt{s - 4m_{\mathrm{t}}^2}\cos\theta\right)$	parameter. 2 E_{t}, θ, θ', ϕ	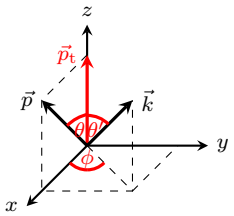
5, 6	$\mathbf{q}'_t$, $\mathbf{q}'_u$	$E_{\bar{\mathrm{t}}} \cdot \left(\sqrt{s} \pm \sqrt{s - 4m_{\mathrm{t}}^2}\cos\tilde{\theta}\right)$	parameter. 3 $E_{\bar{\mathrm{t}}}$, $\tilde{\theta}$, $\tilde{\theta}'$, $\tilde{\phi}$	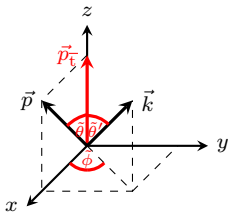

Table 7.1: Asymptotic behavior of the six problematic propagators and the employed parameterization. For two channels each the same set of parameters is used. The number of the phase space parameterization refers to the introduced parameterizations in section 6.3.

Hence, a suitable factorization of this quasi-singularity is

$$\mathbf{q}_t^2 - m_{\mathrm{t}}^2 \sim E_{\mathrm{t}} \left(\sqrt{s} - \sqrt{s - 4m_{\mathrm{t}}^2}\cos\theta\right) \tag{7.30}$$

involving the parameters E_{t} and $\cos\theta$, like in parameterization 2 of section 6.3. The preceding comments are also true for the propagator involving momentum $\mathbf{q}'_t = \mathbf{p}_{\mathrm{t}} - \mathbf{p}_1 + \mathbf{k}$, the only change being the sign of the $\cos\theta$ term. Same reasoning yields

$$\mathbf{q}_u^2 - m_{\mathrm{t}}^2 \sim E_{\bar{\mathrm{t}}} \left(\sqrt{s} - \sqrt{s - 4m_{\mathrm{t}}^2}\cos\tilde{\theta}\right) \tag{7.31}$$

$$\text{and} \quad {\mathbf{q}'_u}^2 - m_{\mathrm{t}}^2 \sim E_{\bar{\mathrm{t}}} \left(\sqrt{s} + \sqrt{s - 4m_{\mathrm{t}}^2}\cos\tilde{\theta}\right), \tag{7.32}$$

that is to say an appropriate parameterization should involve the parameters $E_{\bar{\mathrm{t}}}$ and $\cos\tilde{\theta}$ (cf. parameterization 3 of section 6.3). Table 7.1 summarizes the above found asymptotic behavior of the six involved propagators and the suggested corresponding parameterization. It is remarked at this point that these parameterizations are not the only possible choice. However, it has shown empirically that significant enhancements of the performance of the numerical integration can be achieved with them.

Having found a suitable coordinate system, where the quasi-singularity factorizes, for each problematic denominator, the next step is to find the substitution in these coordinates that eliminates the quasi-singularity. Knowing already the asymptotic behavior of it,

this procedure is straight-forward. Consider for example the asymptotic behavior of the propagator involving momentum $\mathbf{p}'_{\mathrm{t}}$ (expression (7.26)) with the original integration over E_{k} from $E_{\mathrm{k,min}}$ to $E_{\mathrm{k,max}}$ and over $x \equiv \cos\theta'$ from -1 to 1. Since we want the Jacobian invoked by the substitution to cancel the quasi-singularity (cf. example integral (4.5) in section 4.3), in order to obtain the original integration variables in terms of the new ones E'_{k} and x', we perform the analytical integrals

$$\int \mathrm{d}E_{\mathrm{k}}\ \frac{1}{E_{\mathrm{k}}} = \ln E_{\mathrm{k}} \equiv E' \tag{7.33a}$$

$$\int \mathrm{d}x\ \frac{1}{\left(\sqrt{s} - \sqrt{s-4m_{\mathrm{t}}^2}\ x\right)} = \frac{\ln\left[\sqrt{s} - \sqrt{s-4m_{\mathrm{t}}^2}\ x\right]}{-\sqrt{s-4m_{\mathrm{t}}^2}} \equiv x' \tag{7.33b}$$

and solve for E_{t} and x, respectively:

$$E_{\mathrm{k}} = e^{E'} \tag{7.34a}$$

$$x = \frac{\exp\left[-\sqrt{s-4m_{\mathrm{t}}^2}\ x'\right] + \sqrt{s}}{-\sqrt{s-4m_{\mathrm{t}}^2}}. \tag{7.34b}$$

As the integration domain of each new variables must be the unit hypercube (cf. section 4.3), the substitution is furthermore normalized to the integration range 0 to 1. We eventually obtain for the integral in terms of the new variables

$$\int_{E_{\mathrm{k,min}}}^{E_{\mathrm{k,max}}} \mathrm{d}E_{\mathrm{k}} \int_{-1}^{1} \mathrm{d}x\ f(E_{\mathrm{k}}, x) = \int_0^1 \mathrm{d}E' \int_0^1 \mathrm{d}x'\ g_{pt}\big(E_{\mathrm{k},\,pt}(E'), x_{pt}(x')\big)\, f\big(E_{\mathrm{k},\,pt}(E'), x_{pt}(x')\big) \tag{7.35}$$

with

$$E_{\mathrm{k},\,pt}(E') = E_{\mathrm{k,min}} \left(\frac{E_{\mathrm{k,max}}}{E_{\mathrm{k,min}}}\right)^{E'} \tag{7.36a}$$

$$x_{pt}(x') = \left[\sqrt{s} - \left(\frac{\sqrt{s} - \sqrt{s-4m_{\mathrm{t}}^2}}{\sqrt{s} + \sqrt{s-4m_{\mathrm{t}}^2}}\right)^{x'} \left(\sqrt{s} + \sqrt{s-4m_{\mathrm{t}}^2}\right)\right] \frac{1}{\sqrt{s-4m_{\mathrm{t}}^2}} \tag{7.36b}$$

$$g_{pt}(E_{\mathrm{k}}, x) = E_{\mathrm{k}} \left(\sqrt{s} - \sqrt{s-4m_{\mathrm{t}}^2}\ x\right) \ln\left[\frac{E_{\mathrm{k,max}}}{E_{\mathrm{k,min}}}\right] \ln\left[\frac{\sqrt{s} - \sqrt{s-4m_{\mathrm{t}}^2}}{\sqrt{s} + \sqrt{s-4m_{\mathrm{t}}^2}}\right] \frac{1}{\sqrt{s-4m_{\mathrm{t}}^2}}. \tag{7.36c}$$

This procedure of finding a normalized substitution whose Jacobian kills a specific quasi-pol can easily be automatized employing a computer algebra system like `Mathematica`.

Multi-channel Monte Carlo integration

Having obtained all the normalized parameterizations in the previous paragraph, this knowledge is now used to implement the multi-channel Monte Carlo integration environment, which is done in the programming language `C`. As we found six different helpful substitutions, six integration channels are employed. The function to be integrated by the `VEGAS` algorithm takes the form (with $x \equiv \cos\theta'$, $y \equiv \cos\theta$, $\tilde{x} \equiv \cos\tilde{\theta}'$, $\tilde{y} \equiv$

$\cos\tilde{\theta}$)

$$\begin{aligned}\text{prefactor} \cdot \Big[& \text{int}_{\text{par}\,1}\left(x_{pt}(x'), y_{pt}(y'), E_{\text{k},\,pt}(E'), \phi(\phi')\right) && \text{(channel 1)} \\ & + \text{int}_{\text{par}\,1}\left(x_{p\bar{t}}(x'), y_{p\bar{t}}(y'), E_{\text{k},\,p\bar{t}}(E'), \phi(\phi')\right) && \text{(channel 2)} \\ & + \text{int}_{\text{par}\,2}\left(x_{qt}(x'), y_{qt}(y'), E_{\text{t},\,\text{qt}}(E'), \phi(\phi')\right) && \text{(channel 3)} \\ & + \text{int}_{\text{par}\,2}\left(x_{qu}(x'), y_{qu}(y'), E_{\text{t},\,\text{qu}}(E'), \phi(\phi')\right) && \text{(channel 4)} \\ & + \text{int}_{\text{par}\,3}\left(\tilde{x}_{qt'}(x'), \tilde{y}_{qt'}(y'), E_{\bar{\text{t}},\,\text{qt}'}(E'), \tilde{\phi}(\phi')\right) && \text{(channel 5)} \\ & + \text{int}_{\text{par}\,3}\left(\tilde{x}_{qu'}(x'), \tilde{y}_{qu'}(y'), E_{\bar{\text{t}},\,\text{qu}'}(E'), \tilde{\phi}(\phi')\right)\Big] && \text{(channel 6)}\end{aligned} \tag{7.37}$$

where the integration range of all the four parameters (x', y', E', ϕ') is the unit hypercube (from 0 to 1). The terms in (7.37) are defined as

$$\begin{aligned}&\text{int}_{\text{par}\,1}(x, y, E_\text{k}, \phi) = \\ &\quad \alpha_1\, g\, |\overline{\mathcal{M}}|^2 \theta(E'_{\text{k,max}} - E_\text{k}) \theta(+x) \frac{1}{D} \sqrt{E_\text{t}^2 - m_\text{t}^2}\; E_\text{k}\Big|_{E_\text{t}=E_{\text{t},1}} \\ &\quad -\alpha_1\, g\, |\overline{\mathcal{M}}|^2 \theta(E_\text{k} - E'_{\text{k,max}}) \theta(-x) \frac{1}{D} \sqrt{E_\text{t}^2 - m_\text{t}^2}\; E_\text{k}\Big|_{E_\text{t}=E_{\text{t},1}} \\ &\quad +\alpha_1\, g\, |\overline{\mathcal{M}}|^2 \qquad\qquad \theta(-x) \frac{1}{D} \sqrt{E_\text{t}^2 - m_\text{t}^2}\; E_\text{k}\Big|_{E_\text{t}=E_{\text{t},2}},\end{aligned} \tag{7.38}$$

$$\text{int}_{\text{par}\,2}(x, y, E_\text{t}, \phi) = \alpha_2\, g\, |\overline{\mathcal{M}}|^2 \frac{1}{D'} \sqrt{E_\text{t}^2 - m_\text{t}^2}\; E_\text{k}\Big|_{E_\text{k}=E_\text{k}(E_\text{t})} \tag{7.39}$$

and

$$\text{int}_{\text{par}\,3}(\tilde{x}, \tilde{y}, E_{\bar{\text{t}}}, \tilde{\phi}) = \alpha_3\, g\, |\overline{\mathcal{M}}|^2 \frac{1}{D'} \sqrt{E_{\bar{\text{t}}}^2 - m_\text{t}^2}\; E_\text{k}\Big|_{E_\text{k}=E_\text{k}(E_{\bar{\text{t}}})} \tag{7.40}$$

with the total probability density

$$\begin{aligned}\frac{1}{g} = \frac{1}{g(x, y, E_\text{k}, E_\text{t}, \tilde{y})} \equiv & \frac{\alpha_1}{g_{pt}(x, E_\text{k})} + \frac{\alpha_1}{g_{p\bar{t}}(x, E_\text{k})} \\ & + \frac{\alpha_2}{g_{qt}(y, E_\text{t})} + \frac{\alpha_2}{g_{qu}(y, E_\text{t})} + \frac{\alpha_3}{g_{qt}(\tilde{y}, E_{\bar{\text{t}}})} + \frac{\alpha_3}{g_{qu}(\tilde{y}, E_{\bar{\text{t}}})}.\end{aligned} \tag{7.41}$$

The factors α_i $(i = 1, 2, 3)$ are the probabilities for each channel (cf. section 4.3). For the discussion in this paragraph all factors α_i are set equally to 1. Since the algebraic structure of the substitutions for the propagators involving the momenta $\mathbf{p}_t/\mathbf{p}_{t'}$ and $\mathbf{p}_u/\mathbf{p}_{u'}$, respectively, is the same, we have $g_{qt}(y, E) = g_{qt'}(y, E)$ and $g_{qu}(y, E) = g_{qu'}(y, E)$. For this reason the symbol $'$ is omitted at the last two terms in equation (7.41). Note that the terms $\text{int}_{\text{par}\,i}$ in expression (7.37) are just the integrands of the phase space integral for parameterization i as introduced in subsection 6.4.3 multiplied with α_i, the total probability density g and the squared matrix element $|\overline{\mathcal{M}}|^2$. Since g takes the arguments $(x, y, E_\text{k}, E_\text{t}, \tilde{y})$, some of them have to be expressed in terms of the parameters of the corresponding phase space parameterization. In $\text{int}_{\text{par}\,3}$ the variables x and y have to be

expressed in terms of the other variables, which then read

$$x = \cos\theta' = \frac{\vec{p}_{\mathrm{t}} \cdot \vec{k}}{|\vec{p}_{\mathrm{t}}| \cdot |\vec{k}|} = \frac{\left(-\vec{p}_{\bar{\mathrm{t}}} - \vec{k}\right) \cdot \vec{k}}{\left|\vec{p}_{\bar{\mathrm{t}}} + \vec{k}\right| E_{\mathrm{k}}} = -\frac{\sqrt{E_{\bar{\mathrm{t}}}^2 - m_{\mathrm{t}}^2}\,\tilde{x} + E_{\mathrm{k}}}{\sqrt{E_{\bar{\mathrm{t}}}^2 - m_{\mathrm{t}}^2 + E_{\mathrm{k}}^2 + 2\sqrt{E_{\bar{\mathrm{t}}}^2 - m_{\mathrm{t}}^2}\,E_{\mathrm{k}}\,\tilde{x}}} \tag{7.42a}$$

$$y = \cos\theta = \frac{\vec{p}_{\mathrm{t}} \cdot \vec{p}}{|\vec{p}_{\mathrm{t}}| \cdot |\vec{p}|} = \frac{\left(-\vec{p}_{\bar{\mathrm{t}}} - \vec{k}\right) \cdot \vec{p}}{\left|\vec{p}_{\bar{\mathrm{t}}} + \vec{k}\right| \frac{\sqrt{s}}{2}} = -\frac{\sqrt{E_{\bar{\mathrm{t}}}^2 - m_{\mathrm{t}}^2}\,\tilde{y} + E_{\mathrm{k}}\left(\sqrt{1-\tilde{y}^2}\sqrt{1-\tilde{x}^2}\cos\tilde{\phi} + \tilde{x}\tilde{y}\right)}{\sqrt{E_{\bar{\mathrm{t}}}^2 - m_{\mathrm{t}}^2 + E_{\mathrm{k}}^2 + 2\sqrt{E_{\bar{\mathrm{t}}}^2 - m_{\mathrm{t}}^2}\,E_{\mathrm{k}}\,\tilde{x}}}. \tag{7.42b}$$

The formulas for $\tilde{x}(E_{\mathrm{k}}, E_{\mathrm{t}}, x)$ and $\tilde{y}(E_{\mathrm{k}}, E_{\mathrm{t}}, x, y, \phi)$ are of course exactly the same apart from the replacements $x \leftrightarrow \tilde{x}$, $y \leftrightarrow \tilde{y}$, $\phi \leftrightarrow \tilde{\phi}$ and $E_{\mathrm{t}} \leftrightarrow E_{\bar{\mathrm{t}}}$.

Further enhancement: $t\bar{t}$-symmetry

The multi-channel approach presented so far employs six different integration channels. However, by virtue of employing the $t\bar{t}$-symmetry this number can effectively be reduced by two, as argued in the following. The crucial point of this further simplification is the fact that inverting the direction of the fermion line in all the Feynman diagrams (see figure 7.3) yields exactly the same sum of amplitudes. The consequences of the inverting is twofold: On one hand, the role of the top quark and the antitop quark is interchanged, on the other hand the sign of the momenta of the propagators is reversed, as the fermion lines go now into the opposite direction as the momentum. Consider for example the (original) Feynman graph $\mathcal{M}_{B1}$. Diagrammatically it is easily seen that by inverting the fermion line this graph is transformed into the (original) graph $\mathcal{M}_{C2}$. This equivalence can be shown rigorously looking at the expression for the Feynman amplitude $\mathcal{M}_{B1}$ explicitly, with $\mathbf{q}_t' = \mathbf{p}_{\mathrm{t}} - \mathbf{p}_1 + \mathbf{k}$:

$$\mathcal{M}_{B1} \propto \overline{u}(\mathbf{p}_{\mathrm{t}})\Gamma^{\lambda}\frac{\not{\mathbf{p}}_{\mathrm{t}} + \not{\mathbf{k}} + m_{\mathrm{t}}}{2\mathbf{p}_{\mathrm{t}} \cdot \mathbf{k}}\gamma^{\mu}\frac{\not{\mathbf{p}}_{\mathrm{t}} - \not{\mathbf{p}}_1 + \not{\mathbf{k}} + m_{\mathrm{t}}}{(\mathbf{p}_{\mathrm{t}} - \mathbf{p}_1 + \mathbf{k})^2 - m_{\mathrm{t}}^2}\gamma^{\nu}v(\mathbf{p}_{\bar{\mathrm{t}}}). \tag{7.43}$$

Inverting the fermion line yields, according to the Feyman rules,

$$\propto \overline{u}(\mathbf{p}_{\bar{\mathrm{t}}})\gamma^{\nu}\frac{-\not{\mathbf{p}}_{\mathrm{t}} + \not{\mathbf{p}}_1 - \not{\mathbf{k}} + m_{\mathrm{t}}}{(\mathbf{p}_{\mathrm{t}} - \mathbf{p}_1 + \mathbf{k})^2 - m_{\mathrm{t}}^2}\gamma^{\mu}\frac{-\not{\mathbf{p}}_{\mathrm{t}} - \not{\mathbf{k}} + m_{\mathrm{t}}}{2\mathbf{p}_{\mathrm{t}} \cdot \mathbf{k}}\Gamma^{\lambda}v(\mathbf{p}_{\mathrm{t}}). \tag{7.44}$$

Taking into account the conservation of four-momentum in the form $\mathbf{p}_{\mathrm{t}} = \mathbf{p}_1 + \mathbf{p}_2 - \mathbf{p}_{\bar{\mathrm{t}}} - \mathbf{k}$ in the first propagator (involving the original four-momentum $\mathbf{q}_t'$) and performing the replacement $\mathbf{p}_{\mathrm{t}} \leftrightarrow \mathbf{p}_{\bar{\mathrm{t}}}$, one eventually finds

$$\propto \overline{u}(\mathbf{p}_{\mathrm{t}})\gamma^{\nu}\frac{\not{\mathbf{p}}_{\mathrm{t}} - \not{\mathbf{p}}_2 + m_{\mathrm{t}}}{(\mathbf{p}_{\mathrm{t}} - \mathbf{p}_2)^2 - m_{\mathrm{t}}^2}\gamma^{\mu}\frac{-\not{\mathbf{p}}_{\bar{\mathrm{t}}} - \not{\mathbf{k}} + m_{\mathrm{t}}}{2\mathbf{p}_{\bar{\mathrm{t}}} \cdot \mathbf{k}}\Gamma^{\lambda}v(\mathbf{p}_{\bar{\mathrm{t}}}), \tag{7.45}$$

which equals exactly the original amplitude $\mathcal{M}_{C2}$, since $\mathbf{q}_u = \mathbf{p}_{\mathrm{t}} - \mathbf{p}_2$. Analogously, the relations $\mathcal{M}_{A1} \leftrightarrow \mathcal{M}_{A2}$, $\mathcal{M}_{B2} \leftrightarrow \mathcal{M}_{C1}$ and $\mathcal{M}_{B3} \leftrightarrow \mathcal{M}_{C3}$ with respect to the $t\bar{t}$-symmetry can be established. In summary, we thus have

$$\mathcal{M}(E_{\mathrm{t}}, \theta, \theta', \phi) = \mathcal{M}(E_{\bar{\mathrm{t}}}, \widetilde{\theta}, \widetilde{\theta}', \widetilde{\phi}). \tag{7.46}$$

For the definition of the involved parameters is referred to section 6.3. As the only difference between the phase space parameterizations 2 and 3 is the interchange of all variables involving the top quark with the corresponding ones involving the antitop quark, this result can be employed to collect the integration channels 3/5 and 4/6, respectively. The new multi-channel integrand hence takes the form

$$\begin{aligned}\text{prefactor} \cdot \Big[& \text{int}_{\text{par}\,1}\left(x_{pt}(x'), y_{pt}(y'), E_{\text{k},\,pt}(E'), \phi(\phi')\right) \\ & + \text{int}_{\text{par}\,1}\left(x_{p\bar{t}}(x'), y_{p\bar{t}}(y'), E_{\text{k},\,p\bar{t}}(E'), \phi(\phi')\right) \\ & + \text{int}'_{\text{par}\,2}\left(x_{qt}(x'), y_{qt}(y'), E_{\text{t},\,\text{qt}}(E'), \phi(\phi')\right) \\ & + \text{int}'_{\text{par}\,2}\left(x_{qu}(x'), y_{qu}(y'), E_{\text{t},\,\text{qu}}(E'), \phi(\phi')\right)\Big],\end{aligned} \tag{7.47}$$

where the function $\text{int}_{\text{par}\,1}$ is the same as in expression (7.37). However, the term $\text{int}'_{\text{par}\,2}$ differs slightly from $\text{int}_{\text{par}\,2}$ (see expression (7.39)), the difference being the total probability density g. The new total probability density g' now takes the form

$$\begin{aligned} g' = {} & g(x, y, E_{\text{k}}, E_{\text{t}}, \tilde{y}) + g(\tilde{x}, \tilde{y}, E_{\text{k}}, E_{\bar{\text{t}}}, y) = \\ & \left(\frac{\alpha_1}{g_{pt}(x, E_{\text{k}})} + \frac{\alpha_1}{g_{p\bar{t}}(x, E_{\text{k}})} + \frac{\alpha_2}{g_{qt}(y, E_{\text{t}})} + \frac{\alpha_2}{g_{qu}(y, E_{\text{t}})} + \frac{\alpha_2}{g_{qt}(\tilde{y}, E_{\bar{\text{t}}})} + \frac{\alpha_2}{g_{qu}(\tilde{y}, E_{\bar{\text{t}}})}\right)^{-1} \\ & + \left(\frac{\alpha_1}{g_{pt}(\tilde{x}, E_{\text{k}})} + \frac{\alpha_1}{g_{p\bar{t}}(\tilde{x}, E_{\text{k}})} + \frac{\alpha_2}{g_{qt}(y, E_{\text{t}})} + \frac{\alpha_2}{g_{qu}(y, E_{\text{t}})} + \frac{\alpha_2}{g_{qt}(\tilde{y}, E_{\bar{\text{t}}})} + \frac{\alpha_2}{g_{qu}(\tilde{y}, E_{\bar{\text{t}}})}\right)^{-1}. \end{aligned} \tag{7.48}$$

For symmetry reasons the probability factors α_i are set equal in the first two channels and in channels three to six, respectively. For the following statements both factors α_1 and α_2 are set to 1. The advantage of the integrand (7.47) is that the sampling of the squared matrix element $|\mathcal{M}|^2$, which by far consumes the largest amount of computational costs, has to be performed only four times compared with six times for the former integrand (7.37). Nevertheless, the problematic quasi-singularities of the integrand are still canceled by the Jacobians, i. e. both integrands converge equally well. Indeed, it shows that the computational costs for the integration of (7.47) is reduced by approximately 30% compared to the integration of (7.37). Yet, it must be remarked that one can only profit from the above presented enhancement so easily if the top quark and the antitop quark are treated equally, that is to say, in particular, if the same (or no) cuts regarding the top and the antitop quark are applied, because otherwise the $t\bar{t}$-symmetry is broken. However, that does not mean that one cannot employ the $t\bar{t}$-symmetry in such scenarios at all. It is more the case that the treatment becomes more sophisticated (see section 8.1).

Determination of the probability factor α

Up to now we have not benefited from a favorable choice for the probability factors for the reduction of the variance of the numerical integration. For the integral (7.47) there is only one free parameter in doing so, since on must satisfy the normalization condition (4.9b). Thus, the only parameter to be varied is $\alpha := \alpha_1 = 1 - \alpha_2$. By simply computing the cross-section for different values of α, the most favorable value turned out to be $\alpha = 0.99$. A reduction of the computational costs by roughly 30 % to 60 % (additionally to the enhancements mentioned before) is achieved this way. The best value for α itself is approximately independ of the ratio $m_{\text{t}}/\sqrt{s}$.

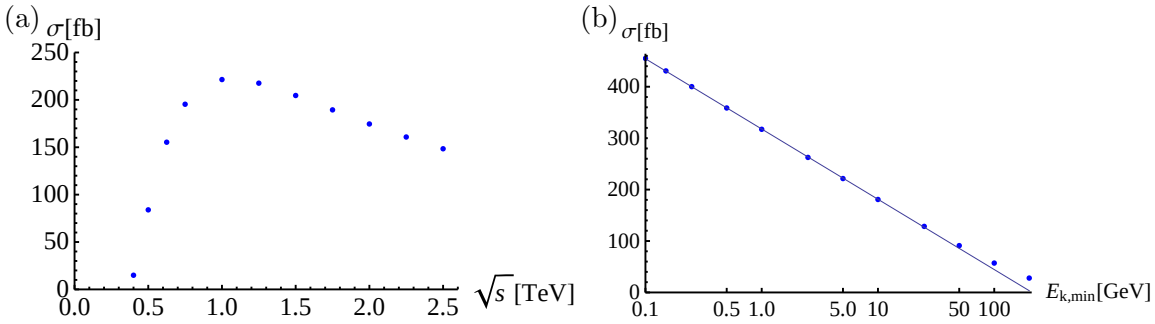

Figure 7.5: (a) Total reaction cross-section for the process $GG \to t\bar{t}\gamma$ as a function of the center-of-mass energy $\sqrt{s}$, where a cut on the minimal energy of the radiated photon of $E_{\mathrm{k,min}} = 5$ GeV is applied. (b) Semi-logarithmic plot of the total reaction cross-section for the process $GG \to t\bar{t}\gamma$ as a function of the value for the cut on the minimal energy of the radiated photon $E_{\mathrm{k,min}}$ at a center-of-mass energy of $\sqrt{s} = 1.0$ TeV. The straight line is a linear fit to the plotted points, where the three ones with largest $E_{\mathrm{k,min}}$ are omitted. In both calculations the top quark mass is assumed to be $m_{\mathrm{t}} = 172$ GeV and the top quark width is neglected. The error bars due to numerical integration are smaller than the dot size.

Discussion of results

For the following discussion of results the optimized phase space integration as presented in expression (7.47) with $\alpha = 0.99$ is employed. The hard scattering total reaction cross-section for the process $GG \to t\bar{t}\gamma$ as a function of the center-of-mass energy $\sqrt{s}$ with a top quark mass of $m_{\mathrm{t}} = 172$ GeV and a cut on the minimal energy of the radiated photon of $E_{\mathrm{k,min}} = 5$ GeV is plotted in figure 7.5(a). The relative error due to numerical integration is 10^{-4} for each data point in this and the following plots. As expected, the cross-section rises sharply for center-of-mass energies slightly above the energy threshold ($2m_{\mathrm{t}}$) to reach a peak around $\sqrt{s} = 1$ TeV and then gradually decreases. Figure 7.5(b) shows the cross-section as a function of the minimal energy of the radiated photon $E_{\mathrm{k,min}}$ at a center-of-mass energy of $\sqrt{s} = 1.0$ TeV. The logarithmic dependence is evident for small values of $E_{\mathrm{k,min}}$ (cf. the discussion of the divergent behavior of bremsstrahlung processes in section 5.3). Finally, the cross-section as a function of $\cos\theta'$, i. e. of the cosine of the angle between the three-momenta of the top quark and the radiated photon, is displayed in figure 7.6(a) for a center-of-mass energy of $\sqrt{s} = 1.0$ TeV, a top quark mass of $m_{\mathrm{t}} = 172$ GeV and a cut on the minimal energy of the radiated photon of $E_{\mathrm{k,min}} = 5$ GeV. This plot is obtained by computing the total reaction cross-section with applying additional cuts on $\cos\theta'$. Each point indicates the value for the cross-section in a range of $\Delta\cos\theta' = 0.1$. For example the point on the left at $\cos\theta' = -0.95$ gives the value for the cross-section in the range $-1 < \cos\theta' < -0.9$. The observed kinks in the graph for values of $|\cos\theta'|$ close to one are independent of the cut $E_{\mathrm{k,min}}$ but sensitive to the top quark mass. A larger mass moves the kinks to smaller values of $|\cos\theta'|$.

Comparison with `WHIZARD`

The results of the semi-analytical calculation for the process $GG \to t\bar{t}\gamma$ are compared to the results obtained by `WHIZARD` in this paragraph. For this approach the total cross-sections discussed above are computed once again employing the `WHIZARD` program system. To facilitate a quantitative comparison all parameters are set to exactly the same values as in the previous calculations. The signed pull between both obtained results for the cross-section as a function of the center-of-mass energy is plotted in figure 7.7(a), the one

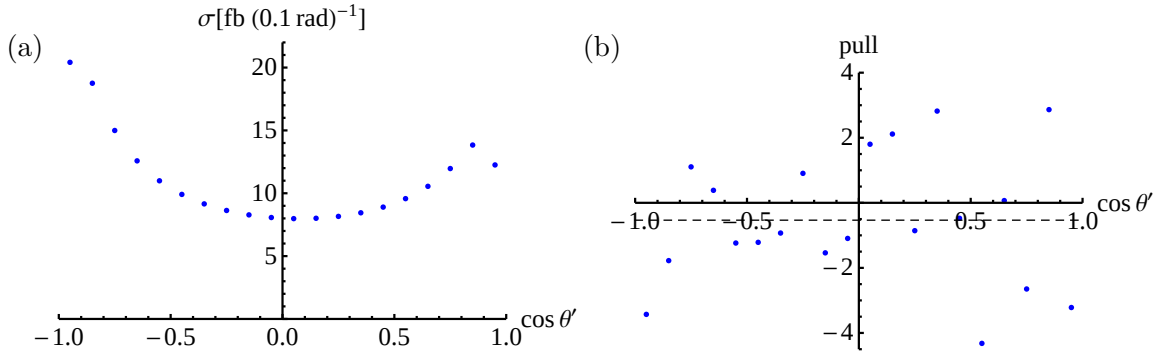

Figure 7.6: (a) Cross-section for the process $GG \to t\bar{t}\gamma$ as a function of $\cos\theta'$ for a center-of-mass energy of $\sqrt{s} = 1.0$ TeV, a top quark mass of $m_\mathrm{t} = 172$ GeV and a cut on the minimal energy of the radiated photon of $E_{\mathrm{k,min}} = 5$ GeV. The plot is obtained by applying cuts on $\cos\theta'$ for each section. The error bars due to numerical integration are smaller than the dot size. (b) Pull between the results of the semi-analytical calculation and the ones of `WHIZARD` for the cross-section as a function of $\cos\theta'$ ($\sqrt{s} = 1.0$ TeV; $m_\mathrm{t} = 172$ GeV; $E_{\mathrm{k,min}} = 5$ GeV). The straight dashed line indicates the mean of all values.

for the cross-section as a function of the minimal energy of the radiated photon $E_{\mathrm{k,min}}$ in figure 7.7(b) and the pull for the cross-section as a function of $\cos\theta'$ in figure 7.6(b). The straight dashed line indicates the mean of the signed pull in each plot. Whereas the estimated relative error due to numerical integration for the semi-analytical calculation is 10^{-4} for each data point in all the plots, the corresponding relative errors for the results of `WHIZARD` vary slightly. For figures 7.7(a) and (b) they are in the order of $1.5 \cdot 10^{-4}$, while for figure 7.6 the relative error varies in the range between $2 \cdot 10^{-4}$ for $|\cos\theta'| \sim 1$ and $5 \cdot 10^{-4}$ for $|\cos\theta'| \sim 0$.
As both the semi-analytical approach and `WHIZARD` employ Monte Carlo integration techniques, the values for the pull statistically fluctuate around 0. Since only three out of 32 values exceed ± 3 and the absolute value of the mean of all values for each plot is significantly below 1, a good accordance of `WHIZARD` with the semi-analytical approach is manifest. For a more quantitative comparison of both calculation approaches is also referred to chapter 9.

7.2.2 Calculation including the top quark width

Up to now the width of the top quark has been neglected. To see how a non-vanishing width affects the results, the process $GG \to t\bar{t}\gamma$ with the SM γtt vertex is considered once again, this time including a finite top quark width Γ_t. At first glance the only thing changing in the calculation procedure is the additional term $\mathrm{i}\, m_\mathrm{t}\Gamma_\mathrm{t}$ in the denominator of the propagators involving spacelike momenta, i. e. in the propagators with momenta $\mathbf{p}'_\mathrm{t}$ and $\mathbf{p}'_{\bar{\mathrm{t}}}$. However, as discussed in section 5.3, such terms violate Gauge invariance and require the usage of the physical polarization sum (5.12) both for the external gluons and the photon. The additional ghost graphs can then be dropped. Yet, due to the more involved polarization sum the computational effort for calculating the squared matrix element significantly increases and so does the length of the obtained expression. Note that this statement is not true for the `WHIZARD` program package. Calculating the matrix elements efficiently as helicity amplitudes, `WHIZARD` always uses the physical polarization sum anyway.

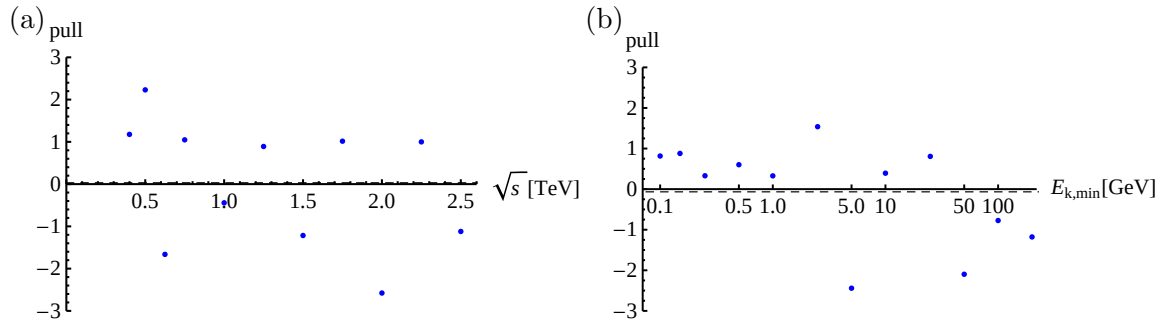

Figure 7.7: (a) Pull between the results of the semi-analytical calculation and the ones of WHIZARD for the cross-section for the process $GG \to t\bar{t}\gamma$ as a function of the center-of-mass energy $\sqrt{s}$, where a cut on the minimal energy of the radiated photon of $E_{\mathrm{k,min}} = 5$ GeV is applied. (b) Semi-logarithmic plot of the pull between the results of the semi-analytical calculation and the ones of WHIZARD for the cross-section for the process $GG \to t\bar{t}\gamma$ as a function of the value for the cut on the minimal energy of the radiated photon $E_{\mathrm{k,min}}$ at a center-of-mass energy of $\sqrt{s} = 1.0$ TeV. The straight dashed line indicates the mean in each plot.

In order to enhance the performance of the numerical integration, the same multi-channel approach as introduced in the preceding subsection is employed. Though the structure of the quasi-singularities of the propagators involving momenta $\mathbf{p}'_{\mathrm{t}}$ and $\mathbf{p}'_{\bar{\mathrm{t}}}$ has changed slightly, it showed that the suggested integration channels of the preceding section still yield satisfactory performance enhancements. Thus, the phase space integration is performed as presented in expression (7.47). In the following discussion the top quark width is assumed to be $\Gamma_{\mathrm{t}} = 1.523$ GeV. The total reaction cross-section is analyzed as a function of the center-of-mass energy (see figure 7.8(a)), the mass of the top quark (see figure 7.8(c)) and the value for the cut on the minimal energy of the radiated photon $E_{\mathrm{k,min}}$ (see figure 7.8(e)). In these graphs the relative deviation $\Delta = (\sigma_0 - \sigma_{\Gamma_{\mathrm{t}}})/\sigma_0$ of the total reaction cross-section of the calculation without considering the top quark width (σ_0) and of the one with $\Gamma_{\mathrm{t}} = 1.523$ GeV ($\sigma_{\Gamma_{\mathrm{t}}}$) is shown. Additionally, to ensure that the physical polarization sum is indeed necessary, the computation is performed once again using the simple polarization sum. It shows that the effect of the top quark width is most prominent for small values of the top quark mass and small values for $E_{\mathrm{k,min}}$. This behavior seems reasonable, since Γ_{t} becomes the dominant term in the denominator of the propagator in this parameter region. Yet, the effect is maximal of the order of 1% for $m_{\mathrm{t}} = 172$ GeV and $E_{\mathrm{k,min}} = 5$ GeV, which are the values that will be used later on for the analysis of the general vertex. Moreover, the effect of the top quark width on the cross-section as a function of $\cos\theta'$ is examined at a center-of-mass energy of $\sqrt{s} = 1.0$ TeV. As obvious from figure 7.8(g), the relative deviation Δ tends to 0 for $\cos\theta' \approx 0$ but increases for $|\cos\theta'|$ approaching 1.

The results for the calculation for the cross-sections including the top quark width using the physical polarization sum are compared to WHIZARD. For this purpose the pull between the semi-analytical results and the results of WHIZARD are shown in figures 7.8(b) for $\sigma(\sqrt{s})$, 7.8(d) for $\sigma(m_{\mathrm{t}})$, 7.8(f) for $\sigma(E_{\mathrm{k,min}})$ and 7.8(h) for $\sigma(\cos\theta')$.
As in the previous subsection the values for the pull are statistically distributed around 0, while very few points with an absolute value for the pull greater than 3 are observed. Since also the means of the values for the pull is very close to 0, a good accordance of the results of WHIZARD with the ones of the semi-analytical approach may safely be assumed.

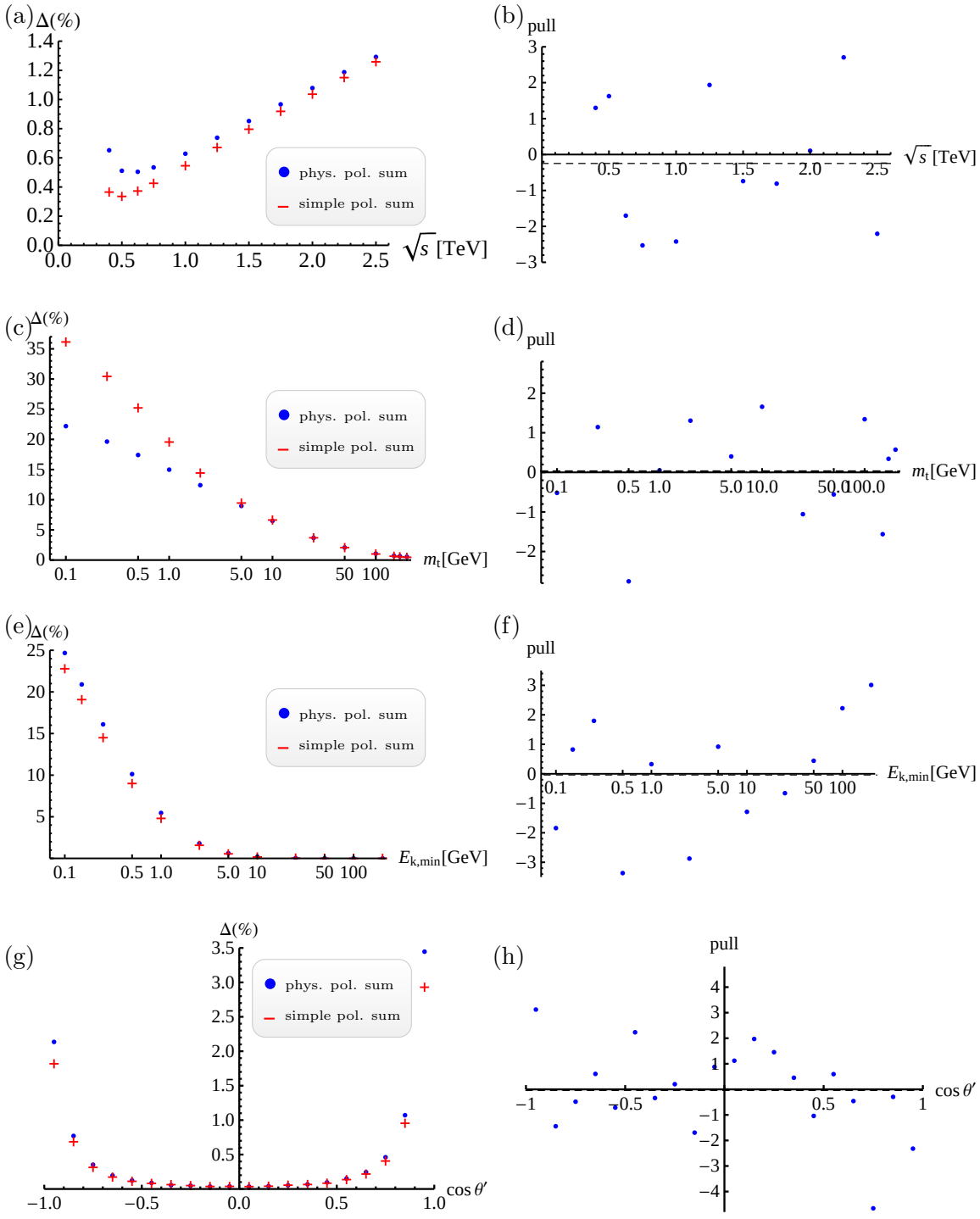

Figure 7.8: Plots on the left: Relative deviation $\Delta = (\sigma_0 - \sigma_{\Gamma_t})/\sigma_0$ of the cross-section for the calculation without considering the top quark width (σ_0) and of the one with $\Gamma_t = 1.523$ GeV (σ_{Γ_t}). Blue points indicate the values where the physical polarization sum is used (for σ_{Γ_t}), red crosses the ones where the simple polarization sum is used. Plots on the right: Pull between the results of the semi-analytical calculation and the ones of `WHIZARD`. In both calculations the physical polarization sum is used. The straight dashed line indicates the mean. In figure (a) and (b) Δ and the pull are shown as a function of the center-of-mass energy $\sqrt{s}$ ($m_t = 172$ GeV; $E_{k,min} = 5$ GeV), in (c) and (d) as a function of the top quark mass ($E_{k,min} = 5$ GeV; $\sqrt{s} = 1.0$ TeV), in (e) and (f) as a function of the value for the cut on the minimal energy of the radiated photon $E_{k,min}$ ($m_t = 172$ TeV; $\sqrt{s} = 1.0$ TeV) and in (g) and (h) as a function of $\cos\theta'$ ($m_t = 172$ TeV; $E_{k,min} = 5$ GeV; $\sqrt{s} = 1.0$ TeV), respectively. Note that the x-axis is scaled logarithmically for the graphs (c) to (f).

7.2.3 Calculation including the general γtt-vertex

In this section the process $GG \to t\bar{t}\gamma$ including the general γtt vertex

$$\Gamma^{\mu}(\mathbf{k}) = \gamma^{\mu} f_{\mathrm{V}}^{\mathrm{A}} - \frac{\upsilon}{\Lambda^2} \mathrm{i}\, \sigma^{\mu\nu} \mathbf{k}_{\nu} (d_{\mathrm{V}}^{\mathrm{A}} + \mathrm{i}\, d_{\mathrm{A}}^{\mathrm{A}} \gamma_5) \tag{7.49}$$

(cf. section 3.3) is considered, where $\upsilon = 246$ GeV and $\Lambda = 1$ TeV. The procedure of calculating the cross-section, as discussed in the previous subsections, is not affected by the general couplings. However, the more involved structure of the vertex once again increases significantly the computational costs both of calculating the squared matrix elements and the numerical integration. Since we found in subsection 7.2.2 that the effect of the top quark width is maximally of the order of 1% for physically interesting parameters, one may expect that the qualitative results of the analysis of the general γtt vertex do not change if the top quark width is neglected. Moreover, the quantitative accordance with `WHIZARD` for the SM-vertex including the top quark width was already seen in subsection 7.2.2. Hence, in the following discussion we abandon the consideration of the top quark width in favor of performance.

Since the general vertex (7.49) involves a γ_5-matrix, terms of the form

$$\mathbf{p}_{a,\mu}\, \mathbf{p}_{b,\nu}\, \mathbf{p}_{c,\rho}\, \mathbf{p}_{d,\sigma}\, \epsilon^{\mu\nu\rho\sigma} \tag{7.50}$$

occur in the squared matrix element, where $\epsilon^{\mu\nu\rho\sigma}$ denotes the fully antisymmetric symbol and $\mathbf{p}_{i,\mu}$ is any of the internal or external four-momenta occurring in the Feynman-graphs. The $\epsilon^{\mu\nu\rho\sigma}$-term vanishes if at least one of the involved four-momenta can be expressed as a linear combination of the other four-momenta. Consequently, for a three-particle final state any term of the form (7.50) either vanishes or is equivalent to

$$\pm \mathbf{p}_{k,\mu}\, \mathbf{p}_{1,\nu}\, \mathbf{p}_{2,\rho}\, \mathbf{p}_{\mathrm{t},\sigma}\, \epsilon^{\mu\nu\rho\sigma}. \tag{7.51}$$

This observation is employed to simplify the obtained expression for the squared matrix element before integration.

Discussion of results

For the following discussion the function

$$\delta\sigma := \frac{\sigma_{\text{anom.}} - \sigma_{\mathrm{SM}}}{\sigma_{\mathrm{SM}}} \tag{7.52}$$

is defined, which is the normalized deviation of the cross-section with anomalous couplings $\sigma_{\text{anom.}}$ from the SM cross-section σ_{SM}. To see how each of the anomalous coupling parameters affects the cross-section qualitatively, at first only one of the three anomalous couplings $f_{\mathrm{V}}^{\mathrm{A}}$, $d_{\mathrm{V}}^{\mathrm{A}}$ and $d_{\mathrm{A}}^{\mathrm{A}}$ is varied simultaneously, while the SM values are kept for the remaining two parameters. As expected from the structure of the vertex, a variation of the parameter $f_{\mathrm{V}}^{\mathrm{A}}$ then just induces a global rescaling of the SM cross-section, which is proportional to ${f_{\mathrm{V}}^{\mathrm{A}}}^2$. Yet, the parameters $d_{\mathrm{V}}^{\mathrm{A}}$ and $d_{\mathrm{A}}^{\mathrm{A}}$ have a more interesting influence. Figure 7.9(a) shows the deviation $\delta\sigma$ as a function of the center-of-mass energy $\sqrt{s}$ for $d_{\mathrm{V}}^{\mathrm{A}} = 1$ and $d_{\mathrm{A}}^{\mathrm{A}} = 1$, the other parameters taking the SM values. Two main conclusions can be drawn from this plot: Firstly, $\delta\sigma$ is dependent on the center-of-mass energy for both couplings. Secondly, the dependence on $\sqrt{s}$ for $d_{\mathrm{V}}^{\mathrm{A}} = 1$ differs from the one for $d_{\mathrm{A}}^{\mathrm{A}} = 1$. This observation will afterwards be employed when formulating a strategy to distinguish

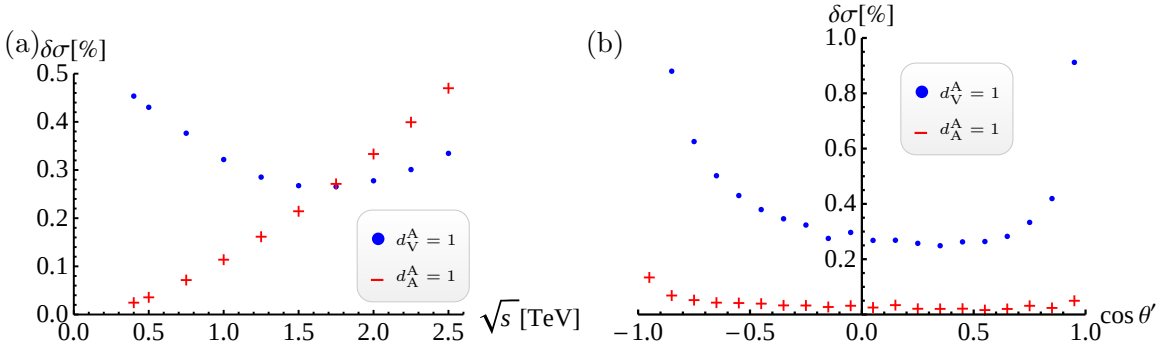

Figure 7.9: (a) Normalized deviation $\delta\sigma := (\sigma_{\text{anom.}} - \sigma_{\text{SM}})/\sigma_{\text{SM}}$ of the cross-section with anomalous couplings $\sigma_{\text{anom.}}$ from the SM cross-section σ_{SM} as a function of the center-of-mass energy $\sqrt{s}$ ($m_t = 172$ GeV; $E_{k,\min} = 5$ GeV). (b) Normalized deviation $\delta\sigma = (\sigma_{\text{anom.}} - \sigma_{\text{SM}})/\sigma_{\text{SM}}$ as a function of $\cos\theta'$ ($\sqrt{s} = 500$ GeV; $m_t = 172$ GeV; $E_{k,\min} = 5$ GeV). In both plots the data set with $d_V^A = 1$ is illustrated with blue points, the one with $d_A^A = 1$ with red crosses. The remaining anomalous parameters are set to their SM values.

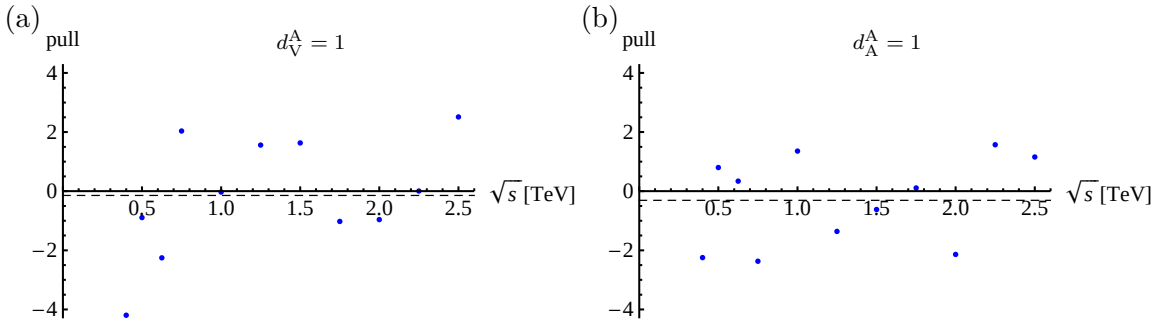

Figure 7.10: Pull between the results of the semi-analytical calculation and the ones of WHIZARD for the cross-section for the process $GG \to t\bar{t}\gamma$ as a function of the center-of-mass energy $\sqrt{s}$ ($m_t = 172$ GeV; $E_{k,\min} = 5$ GeV). The anomalous coupling d_V^A is set to 1 in figure (a), while $d_A^A = 1$ in figure (b). The remaining couplings take SM values. The straight dashed line indicates the mean in each plot.

these two couplings through measurement. The effect of the anomalous couplings is also examined for the cross-section as a function of $\cos\theta'$ in an analogous way. The values for $\delta\sigma$ are plotted in figure 7.9(b) for a center-of-mass energy of $\sqrt{s} = 500$ GeV. It shows that here the qualitative dependence is the same for $d_V^A > 0$ and $d_A^A > 0$. A rescaling of the points for $d_A^A = 1$ by a factor of ~ 10 would yield a similar shape as observed for $d_V^A = 1$ for the dependence of the cross-section on $\cos\theta'$. As a consequence, the analysis of $\delta\sigma(\cos\theta')$ is not useful for the distinction of the anomalous couplings.

Comparison with WHIZARD

For comparison of the results of the preceding paragraph with WHIZARD the corresponding pulls are calculated. Figure 7.10 depicts the pull for the total reaction cross-section $\sigma(\sqrt{s})$ for $d_V^A = 1$ (a) and $d_A^A = 1$ (b), all other couplings taking SM values. The pull for the cross-section as a function of $\cos\theta'$ is shown in figure 7.11(a) and (b) for $d_V^A = 1$ and $d_A^A = 1$, respectively.

Also including anomalous top quark photon couplings the results of WHIZARD are fully consistent with the ones of the semi-analytical approach, since the values for the pull closely fluctuate around 0.

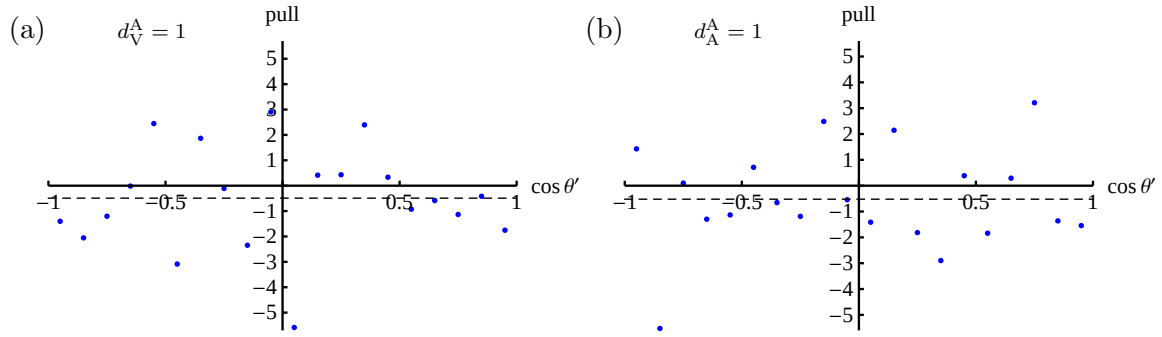

Figure 7.11: Pull between the results of the semi-analytical calculation and the ones of WHIZARD for the cross-section for the process $GG \to t\bar{t}\gamma$ as a function of $\cos\theta'$ ($\sqrt{s} = 500$ GeV; $m_t = 172$ GeV; $E_{k,min} = 5$ GeV). The anomalous coupling d_V^A is set to 1 in figure (a), while $d_A^A = 1$ in figure (b). The remaining couplings take SM values. The straight dashed line indicates the mean in each plot.

7.3 Strategy to distinguish the anomalous couplings

7.3.1 Strategy to distinguish the anomalous couplings on parton level

The information gathered in the previous section can be employed to formulate a strategy to distinguish the three unknown parameters of the general γtt vertex in a fictitious experimental measurement. In this subsection the discussion will be led on parton level, that is to say, in particular, under the assumption that the precise determination of the center-of-mass energy of the event is possible. In this idealized scenario a strategy including the following two steps is suggested:

1. Measurement of the cross-section for the process $GG \to t\bar{t}\gamma$ at different center-of-mass energies $\sqrt{s}$
2. Calculation of the deviation of the cross-section from the SM expectation $\delta\sigma = (\sigma_{anom.} - \sigma_{SM})/\sigma_{SM}$

This allows to extract the first parameter f_V^A from the constant contribution of $\delta\sigma$, while the remaining two parameters d_V^A and d_A^A can be determined from the $\sqrt{s}$-dependent contribution. The latter will be illustrated by an example in the following. For this purpose consider figure 7.12(a) at first. It shows a two-dimensional contour plot of the calculated values for $\delta\sigma$ as a function of the two anomalous coupling parameters d_V^A and d_A^A at a definite center-of-mass energy of $\sqrt{s} = 0.5$ TeV. The plot is obtained by computing the cross-section for each point on the two-dimensional (d_V^A, d_A^A)-grid, where adjacent points are separated by $\Delta = 0.1$ along the d_V^A and d_A^A direction. Though the relative error for each value for the cross-section is estimated to be 10^{-3}, a rather smooth plot is obtained. Of course, the deviation vanishes in the lower left corner at $d_V^A = d_A^A = 0$. Figure 7.12(b) shows a similar plot for the calculated values at a different center-of-mass energy ($\sqrt{s} = 1.5$ TeV). Let us assume that we are actually able to carry out the measurement of the cross-section at these definite center-of-mass energies and further that the analysis of it shows a deviation $\delta\sigma$ of 0.1% at $\sqrt{s} = 0.5$ TeV and of 0.05% at $\sqrt{s} = 1.5$ TeV. Then one can combine the information of these two measurements in a such a way as to enable one to read

the values for $d_{\mathrm{V}}^{\mathrm{A}}$ and $d_{\mathrm{A}}^{\mathrm{A}}$ directly at the point of intersection of the two curves (see figure 7.13). In conclusion, this procedure allows for the determination of all the three anomalous couplings through experimental measurements.

Since the discussion above does not include the convolution of the hard scattering cross-section with the PDFs (cf. section 5.1), this is supplemented in the following subsection.

7.3.2 Strategy to distinguish the anomalous couplings including the convolution with the PDFs

As argued in section 5.1, for hadron colliders the hard interaction cross-section has to be convoluted with the PDFs to obtain the measurable cross-section. For this reason, the feasibility of the strategy to distinguish the anomalous couplings $d_{\mathrm{V}}^{\mathrm{A}}$ and $d_{\mathrm{A}}^{\mathrm{A}}$ including the convolution with the PDFs is examined in this subsection. The analysis is carried out using unweighted events generated by the `WHIZARD` program package at a center-of-mass energy of $\sqrt{s} = 7.0$ TeV with a top quark width of $\Gamma_{\mathrm{t}} = 1.523$ GeV. A cut on the minimal energy of the photon of $E_{\mathrm{k,min}} = 5$ GeV is applied. The PDF description CTEQ6L1 [51] is used. The following discussion is based on samples with around $7.2 \cdot 10^5$ events each, which corresponds to an integrated luminosity of $5.0 \cdot 10^3\, fb^{-1} = 5.0\, ab^{-1}$. Since the study on parton level showed that the deviation $\delta\sigma$ can be separated into the sum $\delta\sigma(d_{\mathrm{V}}^{\mathrm{A}}) + \delta\sigma(d_{\mathrm{A}}^{\mathrm{A}})$ in very good approximation, the event samples are generated only for $d_{\mathrm{V}}^{\mathrm{A}}$ going from 0.1 to 1 in steps of 0.1 while $d_{\mathrm{A}}^{\mathrm{A}} = 0$ and vice versa in order to reduce the computational effort. Furthermore, an additional event sample with SM coupling parameters is produced.

In the following a possible approach for the determination of the anomalous coupling parameters $d_{\mathrm{V}}^{\mathrm{A}}$ and $d_{\mathrm{A}}^{\mathrm{A}}$ is discussed. For this purpose, all events are divided into two classes: The first class contains all events for which the invariant mass of the top quark, the antitop quark and the photon is below a specific threshold $\sqrt{s_1}$, the second class all events where this quantity exceeds a specific threshold $\sqrt{s_2}$. The dependence of $\delta\sigma$ on the partonic center-of-mass energy for $d_{\mathrm{V}}^{\mathrm{A}} = 1$ and $d_{\mathrm{A}}^{\mathrm{A}} = 1$ (cf. figure 7.9(a)) suggests to choose the threshold energies around $\sqrt{s_1} = 750$ GeV and $\sqrt{s_2} = 1.0$ TeV. Certainly it would be more favorable to set $\sqrt{s_2}$ to a larger value but this would negatively affect the available statistics of the second class. Comparing the number of events in the two classes for each sample with anomalous couplings with the one of the SM sample allows to determine the normalized deviation $\delta\sigma$ as a function of $d_{\mathrm{V}}^{\mathrm{A}}$ and $d_{\mathrm{A}}^{\mathrm{A}}$. However, it shows that the effect of the anomalous couplings on the cross-section is much too small to allow an extraction of the parameters from statistical fluctuations in spite of the large integrated luminosity. As a consequence, this approach fails. The situation does not improve when applying an additional cut demanding that the invariant mass of the top quark and the photon is greater than $m_{\mathrm{t}} + 5$ GeV. It is speculated that applying a more stringent cut on the invariant mass of the form $m_{\mathrm{t}} + E_{\mathrm{min}}$, where E_{min} is in the order of the Z-boson mass, could lead to a more promising approach. Moreover, the anomalous couplings cannot be distinguished by the analysis of the transverse momenta of the photon, either.

Though not providing a promising strategy to determine the anomalous couplings, the scenario considered in the previous paragraph is still far from a realistic one, in which several difficulties arise. Firstly, other involved vertices, in this case particularly the Gtt vertex, could contain anomalous couplings, as well. This would lead to an even larger number of

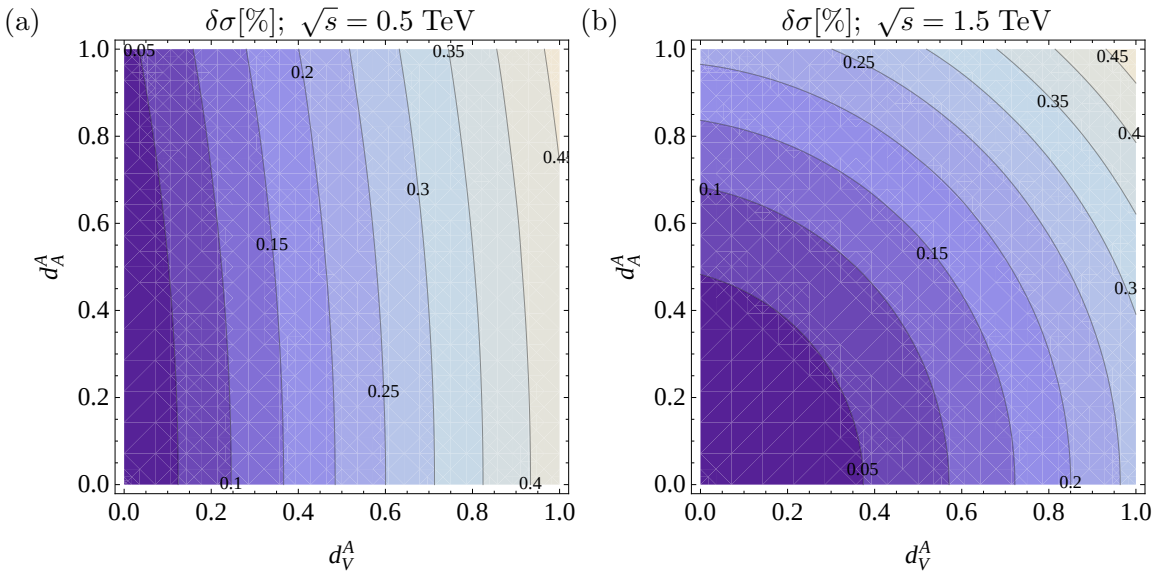

Figure 7.12: Normalized deviation $\delta\sigma = (\sigma_{\text{anom.}} - \sigma_{\text{SM}})/\sigma_{\text{SM}}$ in percent of the cross-section with anomalous couplings $\sigma_{\text{anom.}}$ from the SM cross-section σ_{SM} as a function of the two anomalous couplings d_{V}^{A} and d_{A}^{A} ($m_{\text{t}} = 172$ GeV; $E_{\text{k,min}} = 5$ GeV). Figure (a) shows the calculated values for the definite center-of-mass energy of $\sqrt{s} = 0.5$ TeV, figure (b) for $\sqrt{s} = 1.5$ TeV.

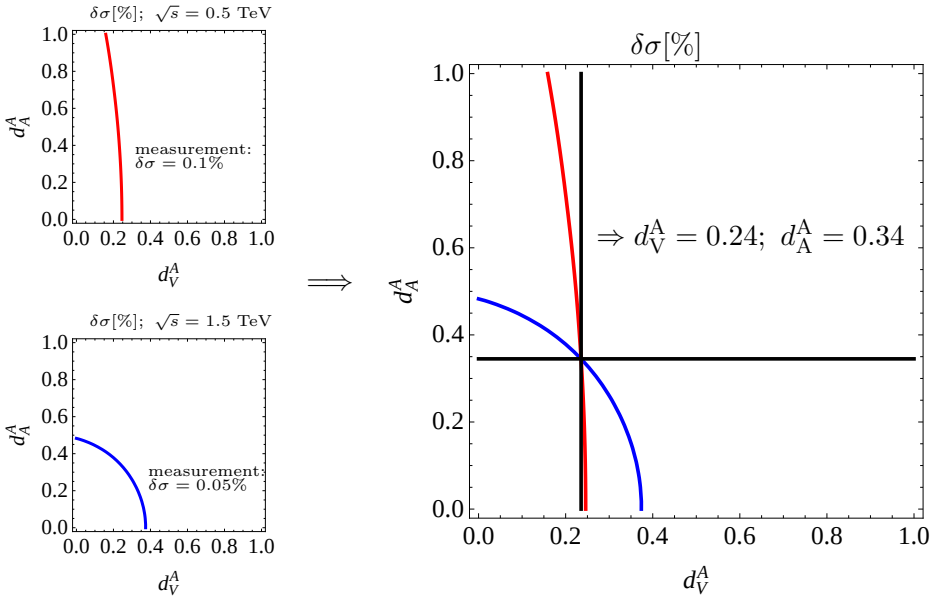

Figure 7.13: Example for the determination of the two anomalous couplings d_{V}^{A} and d_{A}^{A} through measurement. A measured deviation $\delta\sigma$ of 0.1% at $\sqrt{s} = 0.5$ TeV and of 0.05% at $\sqrt{s} = 1.5$ TeV is assumed. The combination of both measurements would restrict the parameters to $d_{\text{V}}^{\text{A}} = 0.24$ and $d_{\text{A}}^{\text{A}} = 0.34$ in this case.

unknown parameters, which would need to be determined. More seriously is however the point that a real measurement always comes with an experimental error. For the measurement of the top quark pair cross-section the error is predicted to be in the order of $5-10\%$ at the ATLAS detector of the LHC [4]. This error might be even larger for the process with additional photon radiation. As the experimental error is expected to be well above the possible deviation due to anomalous couplings, a determination of the parameters of the couplings seems very challenging in the analysis of the total reaction cross-section for the process $GG \to t\bar{t}\gamma$ at the LHC. Yet, by investigating specific differential cross-sections with the objective of finding more appropriate observables, promising strategies to distinguish the anomalous couplings are hopefully formulated in future studies.

8 Analysis of the general Ztt vertex in the process $GG \to t\bar{t}Z$

This chapter deals with the analysis of the anomalous Ztt vertex in the process $GG \to t\bar{t}Z$. As in the case of the γtt vertex, first of all this event is studied with the SM vertex without considering the top quark width (section 8.1) and then including the top quark width in the subsequent section (8.2). Section 8.3 finally analyzes the anomalous couplings including the general Ztt vertex. Strategies to distinguish the anomalous couplings both on parton level and including the convolution with the PDFs are discussed later on in section 8.4.

8.1 Calculation neglecting the top quark width

Firstly, the process $GG \to t\bar{t}Z$ is considered with neither anomalous couplings nor top quark width. For convenience the notation of chapter 7 is kept, i. e. in particular the four-vector of the Z-boson is denoted by $\mathbf{k}$. The Feynman diagrams contributing to this process look exactly the same as for the process $GG \to t\bar{t}\gamma$ (cf. figure 7.3), the only difference being the replacement of the photon in favor of the Z-boson. Hence, the procedure of calculating the total reaction cross-section is very similar. Still, there are two deviations: Firstly, the coupling of the top quark to the Z-boson differs from the γtt-coupling. Secondly, the Z-boson is massive. The latter point implicates several consequences: There are additional longitudinal polarized Z-bosons meaning that the Z-boson has three polarization degrees of freedom. As a consequence, one has to employ the polarization sum for massive gauge bosons, which takes the form

$$\sum_{\text{pol. } s} \epsilon_{\mu,s}(\mathbf{p})\epsilon^*_{\nu,s}(\mathbf{p}) \to -g_{\mu\nu} + \frac{\mathbf{p}_\mu \mathbf{p}_\nu}{m_Z^2}. \tag{8.1}$$

Additionally, having $\mathbf{k}^2 = m_Z^2 > 0$, some of the scalar products involving the external particles are slightly altered (cf. section 7.2). Now they read:

$$\begin{aligned}
\mathbf{p}_1 \cdot \mathbf{p}_2 &= \frac{s}{2} & \mathbf{p}_2 \cdot \mathbf{p}_\mathrm{t} &= \frac{\sqrt{s}}{2}E_\mathrm{t} + \vec{p}\cdot\vec{p}_\mathrm{t} \\
\mathbf{p}_1 \cdot \mathbf{p}_\mathrm{t} &= \frac{s}{2}E_\mathrm{t} - \vec{p}\cdot\vec{p}_\mathrm{t} & \mathbf{p}_2 \cdot \mathbf{p}_{\bar{\mathrm{t}}} &= \frac{s}{2} - \frac{\sqrt{s}}{2}(E_\mathrm{t} + E_\mathrm{k}) - \vec{p}\cdot\vec{p}_\mathrm{t} - \vec{p}\cdot\vec{k} \\
\mathbf{p}_1 \cdot \mathbf{p}_{\bar{\mathrm{t}}} &= \frac{s}{2} - \frac{\sqrt{s}}{2}(E_\mathrm{t} + E_\mathrm{k}) + \vec{p}\cdot\vec{p}_\mathrm{t} + \vec{p}\cdot\vec{k} & \mathbf{p}_2 \cdot \mathbf{p}_\mathrm{k} &= \frac{\sqrt{s}}{2}E_\mathrm{k} + \vec{p}\cdot\vec{k} \\
\mathbf{p}_1 \cdot \mathbf{p}_\mathrm{k} &= \frac{\sqrt{s}}{2}E_\mathrm{k} - \vec{p}\cdot\vec{k} & \mathbf{p}_\mathrm{t} \cdot \mathbf{p}_{\bar{\mathrm{t}}} &= E_\mathrm{t}(\sqrt{s} - E_\mathrm{k}) - m_\mathrm{t}^2 + \vec{p}\cdot\vec{k} - m_Z^2,
\end{aligned}$$

with

$$\begin{aligned}
\vec{p}\cdot\vec{p}_{\mathrm{t}} &= \frac{\sqrt{s}}{2}\sqrt{E_{\mathrm{t}}^2 - m_{\mathrm{t}}}\cos\theta \\
\vec{p}\cdot\vec{k} &= \frac{\sqrt{s}}{2}\sqrt{E_{\mathrm{k}}^2 - m_Z^2}\left(\sin\theta\sin\theta'\cos\phi + \cos\theta\cos\theta'\right) \\
\vec{p}_{\mathrm{t}}\cdot\vec{k} &= \sqrt{E_{\mathrm{t}}^2 - m_{\mathrm{t}}^2}\,\sqrt{E_{\mathrm{k}}^2 - m_Z^2}\cos\theta'.
\end{aligned}$$

As discussed in chapter 6, the phase space is also affected by the mass of the final state particles. For the process $GG \to t\bar{t}Z$ the phase space integral as introduced in section 6.4.2 is performed. Furthermore, because of $\mathbf{k}^2 = m_Z^2 > 0$ this term adds in the denominator of the propagators involving momenta $\mathbf{p}_{\mathrm{t}}'$ and $\mathbf{p}_{\bar{\mathrm{t}}}'$. This additional mass prevents the divergence of the phase space integral for small values for the energy E_{k} of the Z-boson. No explicit cut on the minimal energy of the Z-boson is thus required. Though the convergence behavior of the integral is positively affected for the same reason, a multi-channel Monte Carlo approach is nevertheless preferable for the phase space integration. As the denominator of the propagators with momenta $\mathbf{p}_{\mathrm{t}}'$ and $\mathbf{p}_{\bar{\mathrm{t}}}'$ has changed, new substitutions need to be found. The denominator with momentum $\mathbf{p}_{\mathrm{t}}'$ takes now the form

$$2E_{\mathrm{k}}E_{\mathrm{t}} - 2\sqrt{E_{\mathrm{t}}^2 - m_{\mathrm{t}}^2}\sqrt{E_{\mathrm{k}}^2 - m_Z^2}\cos\theta' + m_Z^2. \tag{8.2}$$

Its asymptotic behavior is well approximated by the factorized ansatz

$$\left(\sqrt{s}E_{\mathrm{k}} + m_Z^2\right)\left(s + 2m_Z^2 - \sqrt{s - 4m_{\mathrm{t}}}\sqrt{s - 4m_Z}\cos\theta'\right). \tag{8.3}$$

Since this approach involves the parameters E_{k} and $\cos\theta'$, it is suitable for parameterization 1 of section 6.3. For the propagator involving momentum $\mathbf{p}_{\bar{\mathrm{t}}}'$ a similar ansatz is chosen, where $\cos\theta'$ is replaced with $\cos\tilde{\theta}'$. Note that there is no need to adapt the substitutions of integration channels 3 to 6 of the multi-channel approach (7.37) because m_Z does not occur in the chosen parameterizations. Still the integrals of the corresponding phase space parameterizations are changed in comparison to section 7.2.

Multi-channel Monte Carlo integration

The multi-channel Monte Carlo approach for the phase space integration for the process $GG \to t\bar{t}Z$ takes the form as stated in equation (7.37) for the process $GG \to t\bar{t}\gamma$. However, the definitions of the terms $\mathrm{int}_{\mathrm{par}\,i}$ now are

$$\begin{aligned}
&\mathrm{int}_{\mathrm{par}\,1}(x, y, E_{\mathrm{k}}, \phi) = \\
&\quad \alpha_1\, g\, |\overline{\mathcal{M}}|^2 \theta(E'_{\mathrm{k,max}} - E_{\mathrm{k}})\theta(+x)\frac{1}{D}\sqrt{E_{\mathrm{t}}^2 - m_{\mathrm{t}}^2}\sqrt{E_{\mathrm{k}}^2 - m_Z^2}\Big|_{E_{\mathrm{t}}=E_{\mathrm{t},1}} \\
&\quad -\alpha_1\, g\, |\overline{\mathcal{M}}|^2 \theta(E_{\mathrm{k}} - E'_{\mathrm{k,max}})\theta(-x)\frac{1}{D}\sqrt{E_{\mathrm{t}}^2 - m_{\mathrm{t}}^2}\sqrt{E_{\mathrm{k}}^2 - m_Z^2}\Big|_{E_{\mathrm{t}}=E_{\mathrm{t},1}} \\
&\quad +\alpha_1\, g\, |\overline{\mathcal{M}}|^2 \qquad\qquad \theta(-x)\frac{1}{D}\sqrt{E_{\mathrm{t}}^2 - m_{\mathrm{t}}^2}\sqrt{E_{\mathrm{k}}^2 - m_Z^2}\Big|_{E_{\mathrm{t}}=E_{\mathrm{t},2}},
\end{aligned} \tag{8.4}$$

$$\begin{aligned}
&\mathrm{int}_{\mathrm{par}\,2}(x, y, E_\mathrm{t}, \phi) = \\
&\quad \alpha_2\, g\, |\overline{\mathcal{M}}|^2 \theta(E'_{\mathrm{t,max}} - E_\mathrm{t}) \theta(+x) \frac{1}{D'} \sqrt{E_\mathrm{t}^2 - m_\mathrm{t}^2} \sqrt{E_\mathrm{k}^2 - m_Z^2} \Big|_{E_\mathrm{k}=E_{\mathrm{k},1}} \\
&\quad -\alpha_2\, g\, |\overline{\mathcal{M}}|^2 \theta(E_\mathrm{t} - E'_{\mathrm{t,max}}) \theta(-x) \frac{1}{D'} \sqrt{E_\mathrm{t}^2 - m_\mathrm{t}^2} \sqrt{E_\mathrm{k}^2 - m_Z^2} \Big|_{E_\mathrm{k}=E_{\mathrm{k},1}} \\
&\quad +\alpha_2\, g\, |\overline{\mathcal{M}}|^2 \qquad\qquad \theta(-x) \frac{1}{D'} \sqrt{E_\mathrm{t}^2 - m_\mathrm{t}^2} \sqrt{E_\mathrm{k}^2 - m_Z^2} \Big|_{E_\mathrm{k}=E_{\mathrm{k},2}}
\end{aligned} \tag{8.5}$$

and

$$\begin{aligned}
&\mathrm{int}_{\mathrm{par}\,3}(\tilde{x}, \tilde{y}, E_{\bar{\mathrm{t}}}, \tilde{\phi}) = \\
&\quad \alpha_3\, g\, |\overline{\mathcal{M}}|^2 \theta(E'_{\bar{\mathrm{t}},\mathrm{max}} - E_{\bar{\mathrm{t}}}) \theta(+\tilde{x}) \frac{1}{D'} \sqrt{E_{\bar{\mathrm{t}}}^2 - m_\mathrm{t}^2} \sqrt{E_\mathrm{k}^2 - m_Z^2} \Big|_{E_\mathrm{k}=E_{\mathrm{k},1}} \\
&\quad -\alpha_3\, g\, |\overline{\mathcal{M}}|^2 \theta(E_{\bar{\mathrm{t}}} - E'_{\bar{\mathrm{t}},\mathrm{max}}) \theta(-\tilde{x}) \frac{1}{D'} \sqrt{E_{\bar{\mathrm{t}}}^2 - m_\mathrm{t}^2} \sqrt{E_\mathrm{k}^2 - m_Z^2} \Big|_{E_\mathrm{k}=E_{\mathrm{k},1}} \\
&\quad +\alpha_3\, g\, |\overline{\mathcal{M}}|^2 \qquad\qquad \theta(-\tilde{x}) \frac{1}{D'} \sqrt{E_{\bar{\mathrm{t}}}^2 - m_\mathrm{t}^2} \sqrt{E_\mathrm{k}^2 - m_Z^2} \Big|_{E_\mathrm{k}=E_{\mathrm{k},2}} .
\end{aligned} \tag{8.6}$$

The total probability density reads

$$\begin{aligned}
\frac{1}{g} = \frac{1}{g(x, y, E_\mathrm{k}, E_\mathrm{t}, \tilde{x}, \tilde{y})} \equiv &\frac{\alpha_1}{g_{pt}(x, E_\mathrm{k})} + \frac{\alpha_1}{g_{pt}(\tilde{x}, E_\mathrm{k})} \\
&+ \frac{\alpha_2}{g_{qt}(y, E_\mathrm{t})} + \frac{\alpha_2}{g_{qu}(y, E_\mathrm{t})} + \frac{\alpha_3}{g_{qt}(\tilde{y}, E_{\bar{\mathrm{t}}})} + \frac{\alpha_3}{g_{qu}(\tilde{y}, E_{\bar{\mathrm{t}}})}.
\end{aligned} \tag{8.7}$$

The formulas to express x and y in terms of $\tilde{x}$ and $\tilde{y}$ and vice versa are obtained from expressions (7.42) by replacing E_k in favor of $\sqrt{E_\mathrm{k}^2 - m_Z^2}$.

Further enhancement: $t\bar{t}$-symmetry

The enhancement of the phase space integral by virtue of the $t\bar{t}$-symmetry as applied for the process $GG \to t\bar{t}\gamma$ in section 7.2 cannot be adopted directly because the structure of the integrals of phase space parameterizations 2 and 3 has changed drastically. These integrals now involve the step-functions $\theta(\pm x)$ and $\theta(\pm\tilde{x})$, which act as top and antitop specific cuts, respectively. Hence, the $t\bar{t}$-symmetry is not fully provided any more. Nevertheless, if $x(x')$ and $\tilde{x}(x')$ have the same sign, the Feynman amplitude in terms of the variables of the top quark and the one in terms of the antitop quark are still identical, i. e. equation 7.46 holds. This observation is employed in the implementation in `C`. Formally the integration channels 3/5 and 4/6 are treated separately. Yet, the computed values for the squared matrix elements of channels 3 and 4 are temporarily stored so that they can be reused for channels 5 and 6, respectively, if possible. Moreover, channels 1 and 2 were chosen such that the employment of the $t\bar{t}$-symmetry is feasible without difficulties. Thus, the

optimized integrand takes the form

$$\begin{aligned}\text{prefactor} \cdot \Big[& 2 \cdot \text{int}_{\text{par}\,1}\left(x_{pt}(x'), y_{pt}(y'), E_{\text{k},\,pt}(E'), \phi(\phi')\right) \\ & + \text{int}_{\text{par}\,2}\left(x_{qt}(x'), y_{qt}(y'), E_{\text{t},\,\text{qt}}(E'), \phi(\phi')\right) \\ & + \text{int}_{\text{par}\,2}\left(x_{qu}(x'), y_{qu}(y'), E_{\text{t},\,\text{qu}}(E'), \phi(\phi')\right) \\ & + \text{int}_{\text{par}\,3}\left(\tilde{x}_{qt'}(x'), \tilde{y}_{qt'}(y'), E_{\bar{\text{t}},\,\text{qt}'}(E'), \tilde{\phi}(\phi')\right) \\ & + \text{int}_{\text{par}\,3}\left(\tilde{x}_{qu'}(x'), \tilde{y}_{qu'}(y'), E_{\bar{\text{t}},\,\text{qu}'}(E'), \tilde{\phi}(\phi')\right)\Big],\end{aligned} \tag{8.8}$$

where the values for the squared matrix elements of parameterization 3 are adopted from the computation for parameterization 2 if possible. With this procedure a reduction of the computational costs for the total reaction cross-section of about 30% was measured, where all probability factors α_i are set to 1. Since all integration channels are formally implemented separately, it is possible to benefit from this enhancement also in calculations where (anti-)top quark specific cuts are applied, as it is the case for the computation of the cross-section as a function of the cosine of the angle between the three-momenta of the top quark and the Z-boson ($\cos\theta'$). The achieved gain of performance is however dependent on the type of the cut.

Determination of the probability factor α

To further optimize the performance of the integration the probability factors α_i are determined empirically. For symmetry reasons α_2 and α_3 are supposed to be identical so that only one parameter $\alpha = \alpha_1 = 1 - \alpha_2$ is variable. Testing different values for α showed that the most favorable value depends on the top quark mass for a definite center-of-mass energy. In the subsequent calculations with $m_\text{t} = 172$ GeV the setting $\alpha = 0.7$ is used, which results in a reduction of the computational costs of approximately 10% (additionally to the enhancements mentioned before).

Discussion of results

The hard scattering total reaction cross-section for the process $GG \to t\bar{t}Z$ as a function of the center-of-mass energy $\sqrt{s}$ with a top quark mass of $m_\text{t} = 172$ GeV is shown in figure 8.1(a), whereas the dependence on $\cos\theta'$, i. e. on the cosine of the angle between the three-momenta of the top quark and the Z-boson, is presented for the same top quark mass and a center-of-mass energy of $\sqrt{s} = 1.0$ TeV in figure 8.1(b). The shape of the function $\sigma(\sqrt{s})$ is similar to the one of the process $GG \to t\bar{t}\gamma$ but slightly shifted to larger values of $\sqrt{s}$. The estimated relative error due to numerical integration is 10^{-4} for each point in both plots.

Comparison with `WHIZARD`

Once again, the results obtained so far are compared to the ones of the `WHIZARD` program package. The signed pull (for its definition see equation (7.24)) for the total reaction cross-section as a function of the center-of-mass energy and as a function of $\cos\theta'$ is plotted in figure 8.2(a) and (b), respectively. The estimated relative errors for the Monte Carlo integration of the computation of `WHIZARD` varies slightly and is in the order of 10^{-4}.
The plots show that the values for the pull statistically fluctuate around 0 with a maximum absolute value of approximately 4 for the pull as a function of $\cos\theta'$ and of around 2.3 for the pull as a function of $\sqrt{s}$. For both samples the mean of all values for the pull is close to

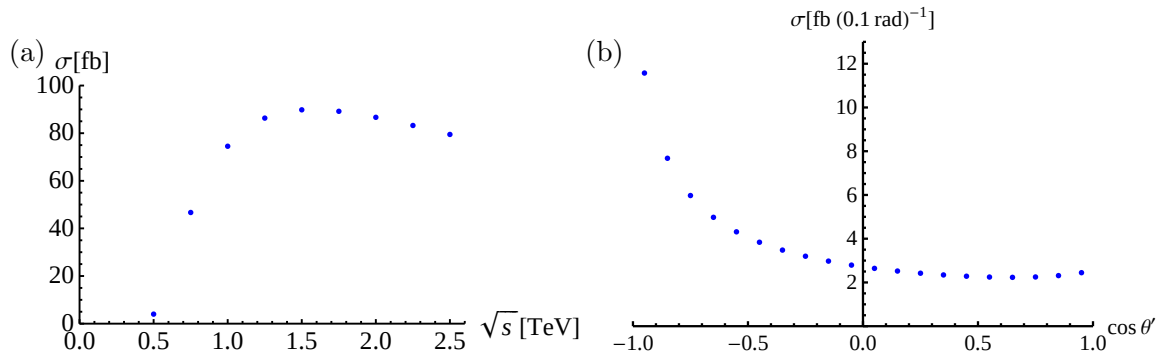

Figure 8.1: (a) Total reaction cross-section for the process $GG \to t\bar{t}Z$ as a function of the center-of-mass energy $\sqrt{s}$. (b) Cross-section as a function of $\cos\theta'$ for a center-of-mass energy of $\sqrt{s} = 1.0$ TeV. In both calculations the top quark mass is assumed to be $m_t = 172$ GeV and the top quark width is neglected. The error bars due to numerical integration are smaller than the dot size.

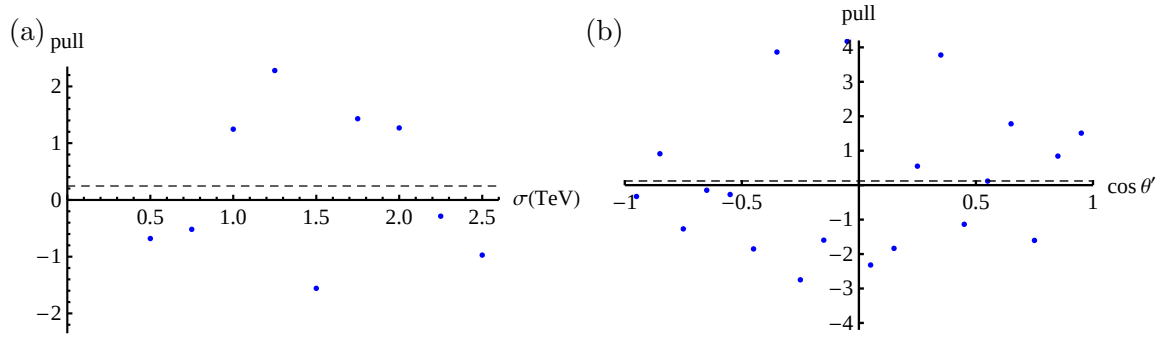

Figure 8.2: (a) Pull between the results of the semi-analytical calculation and of `WHIZARD` for the cross-section for the process $GG \to t\bar{t}Z$ as a function of the center-of-mass energy $\sqrt{s}$. (b) Pull between the results of the semi-analytical calculation and of `WHIZARD` for the cross-section as a function of $\cos\theta'$ for a center-of-mass energy of $\sqrt{s} = 1.0$ TeV. The straight dashed line indicates the mean in each plot.

0. In conclusion, a good qualitative accordance of both calculation approaches is evident. A more quantitative comparison is supplemented in chapter 9.

8.2 Calculation including the top quark width

The calculations of the previous section are done once again including a finite top quark width of $\Gamma_\mathrm{t} = 1.523$ GeV. As argued in section 5.3, the physical polarization sum (5.12) has to be used for the external gluons to substract contributions of unphysical polarizations. As already mentioned for the process $GG \to t\bar{t}\gamma$ in subsection 7.2.2, this leads to a significant increase of the computational costs for the calculation of the squared matrix element and the numerical integration. Yet, the polarization sum of the Z-boson is not affected by the involvement of the top quark width. The effect of the top quark width on the cross-section is analyzed as a function of the top quark mass varying from $m_\mathrm{t} = 0.1$ GeV to $m_\mathrm{t} = 200$ GeV at a center-of-mass energy of $\sqrt{s} = 1.0$ TeV, as a function of the center-of-mass energy varying from $\sqrt{s} = 0.5$ TeV to $\sqrt{s} = 2.5$ TeV with a top quark mass of $m_\mathrm{t} = 172$ GeV and as a function of $\cos\theta'$ ($\sqrt{s} = 1.0$ TeV; $m_\mathrm{t} = 172$ GeV). For none of these calculations a change of the result due to the top quark width can be observed within the error for the numerical integration, where the relative error is estimated to be 10^{-4} everywhere. This result is fully in accordance with the computation of `WHIZARD` (The plots of the corresponding pulls can be found in appendix C.1.). That means that the top quark width can safely be neglected for the process $GG \to t\bar{t}Z$. This observation seems reasonable when considering that the absolute value of the additional term $\mathrm{i}\, m_\mathrm{t}\Gamma_\mathrm{t}$ in the denominator of the propagators with momenta $\mathbf{p}'_\mathrm{t}$ and $\mathbf{p}'_{\bar{\mathrm{t}}}$, which take the generic form

$$\frac{1}{2\,\mathbf{p}\cdot\mathbf{k} + m_Z^2 + \mathrm{i}\, m_\mathrm{t}\Gamma_\mathrm{t}}, \tag{8.9}$$

is small compared to the square of the mass of the Z-boson m_Z^2.

8.3 Calculation including the general Ztt-vertex

The aim of this section is the analysis of the general Ztt vertex

$$\Gamma^\mu(\mathbf{k}) = \gamma^\mu\big(g_\mathrm{V} - g_\mathrm{A}\gamma_5\big) - \frac{v^2}{\Lambda^2}\Big[\gamma^\mu\big(X_\mathrm{L}^\mathrm{Z}P_\mathrm{L} + X_\mathrm{R}^\mathrm{Z}P_\mathrm{R}\big) + \frac{\mathrm{i}\,\sigma^{\mu\nu}\mathbf{k}_\nu}{m_Z}\big(d_\mathrm{V}^\mathrm{Z} + \mathrm{i}\, d_\mathrm{A}^\mathrm{Z}\gamma_5\big)\Big] \tag{8.10}$$

(cf. section 3.3), where $v = 246$ GeV and $\Lambda = 1$ TeV. The projectors are defined as $P_\mathrm{R} = 1 + \gamma_5$ and $P_\mathrm{L} = 1 - \gamma_5$. The SM vector and axial-vector couplings take the values $g_\mathrm{V} = 1/2 - 4/3(\sin\theta_\mathrm{W})^2$ and $g_\mathrm{A} = 1/2$, respectively (cf. equations (3.7) of section 3.1). Since it was seen in the previous section that the top quark width is negligible, in the following analyzes the top quark width is set to zero.

Discussion of results

For the examination of the modification of the cross-section due to the four anomalous couplings the normalized deviation $\delta\sigma = (\sigma_\mathrm{anom.} - \sigma_\mathrm{SM})/\sigma_\mathrm{SM}$ is considered analogously to the preceding chapter. First of all, the effect on the cross-section as a function of the

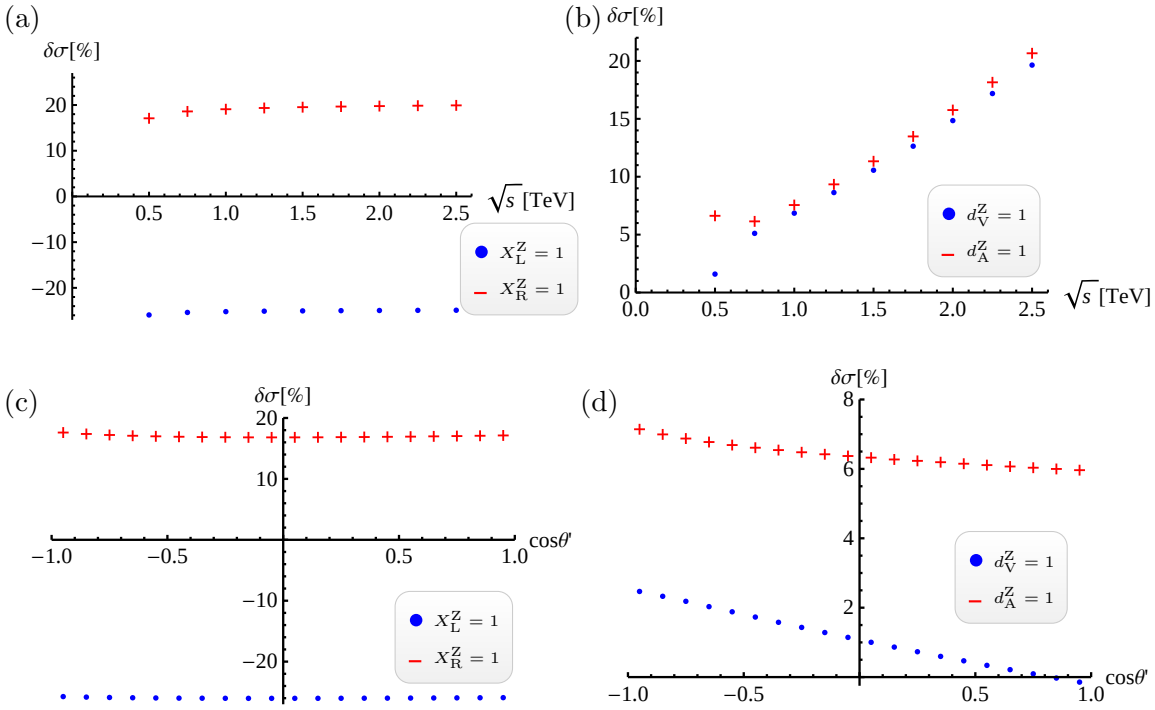

Figure 8.3: Normalized deviation $\delta\sigma = (\sigma_{\text{anom.}} - \sigma_{\text{SM}})/\sigma_{\text{SM}}$ of the cross-section with anomalous couplings $\sigma_{\text{anom.}}$ from the SM cross-section σ_{SM}. In the plots on the left (a) and (c) the results are shown for $X_{\text{L}}^{\text{Z}} = 1$ and $X_{\text{R}}^{\text{Z}} = 1$, in the plots on the right (b) and (d) for $d_{\text{V}}^{\text{Z}} = 1$ and $d_{\text{A}}^{\text{Z}} = 1$. The remaining parameters are set to their SM value. In figures (a) and (b) $\delta\sigma$ is plotted as a function of the center-of-mass energy $\sqrt{s}$ ($m_{\text{t}} = 172$ GeV), in figures (c) and (d) as a function of $\cos\theta'$ ($\sqrt{s} = 0.5$ TeV; $m_{\text{t}} = 172$ GeV).

center-of-mass energy is analyzed. Figure 8.3(a) shows $\delta\sigma$ where either the coupling X_{L}^{Z} or X_{R}^{Z} is set to 1 and the remaining ones to 0, whereas in figure 8.3(b) only d_{V}^{Z} or d_{A}^{Z} is turned on. The deviation for the parameters X_{L}^{Z} or X_{R}^{Z} is independent of the center-of-mass energy. In contrast to that in the case $d_{\text{V}}^{\text{Z}} = 1$ or $d_{\text{A}}^{\text{Z}} = 1$ the function $\delta\sigma$ is approximately linear dependent on $\sqrt{s}$ with almost identical slope for both couplings in the range from $\sqrt{s} = 0.75$ TeV to $\sqrt{s} = 2.5$ TeV. It is only for center-of-mass energies close to the energy threshold for this process that a distinction between d_{V}^{Z} and d_{A}^{Z} seems possible. Looking at the deviation $\delta\sigma$ for the cross-section as a function of $\cos\theta'$ at a center-of-mass energy of $\sqrt{s} = 0.5$ TeV, the situation is very similar for the parameters X_{L}^{Z} and X_{R}^{Z} (see figure 8.3(c)). Once again, the probability of distinguishing the anomalous couplings in this analysis looks more promising for the parameters d_{V}^{Z} and d_{A}^{Z}. Having $d_{\text{A}}^{\text{Z}} = 1$, $\delta\sigma$ is positive over the whole range of $\cos\theta'$. On the contrary, $\delta\sigma$ changes its sign near $\cos\theta' = 0.8$ for $d_{\text{V}}^{\text{Z}} = 1$. Additionally, the plots of $\delta\sigma$ for $\sqrt{s} = 1.0$ TeV are shown in figure C.2 of appendix C.2.

Moreover, the normalized deviation from the SM expectation is examined for the cross-section as a function of the energy of the Z-boson, for the invariant mass $(\mathbf{p}_{\text{t}} + \mathbf{k})^2$ of the top quark and the Z-boson and for the scalar triple product $(\mathbf{p}_{\text{t}} \times \mathbf{p}) \cdot \mathbf{k}$. The obtained results are plotted both for a center-of-mass energy of $\sqrt{s} = 0.5$ TeV and $\sqrt{s} = 1.0$ TeV in figure C.4 of appendix C.2. Though the analysis of these quantities could provide a possibility to cross-check the measured values for the couplings d_{V}^{Z} and d_{A}^{Z}, no distinction between the parameters X_{L}^{Z} and X_{R}^{Z} seems feasible. Still, the most promising approach for the latter might be the study of the scalar triple product at energies close to the energy threshold.

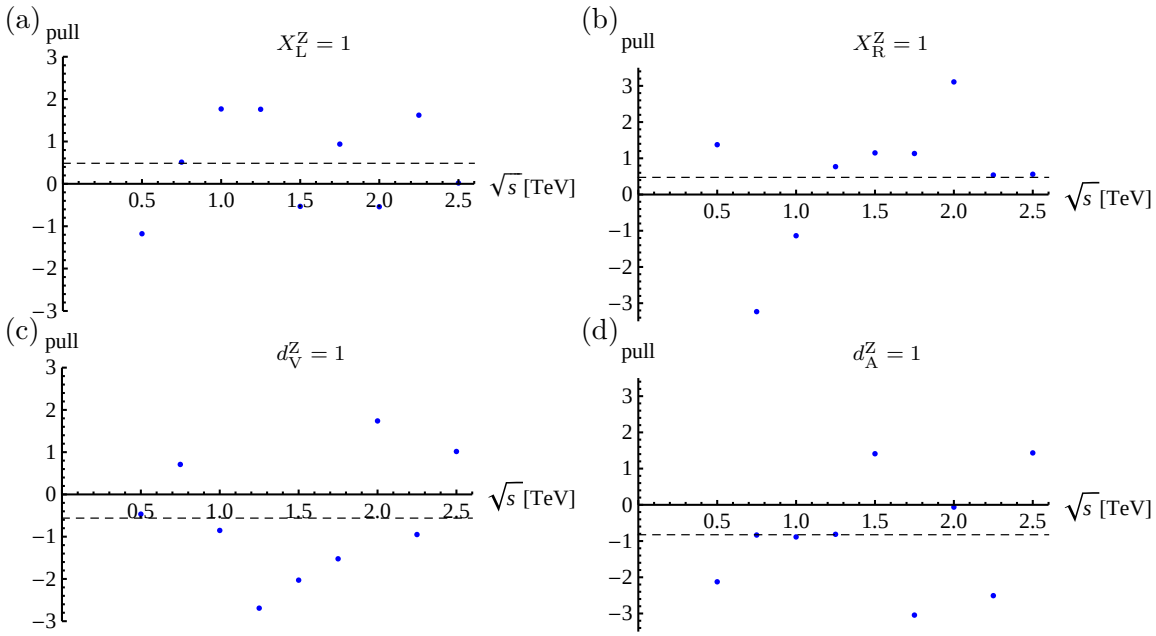

Figure 8.4: Pull between the results of the semi-analytical calculation and the ones of WHIZARD for the cross-section for the process $GG \to t\bar{t}Z$ as a function of the center-of-mass energy $\sqrt{s}$ ($m_t = 172$ GeV). Figure (a) shows the pull for $X_L^Z = 1$, figure (b) for $X_R^Z = 1$, figure (c) for $d_V^Z = 1$ and figure (d) for $d_A^Z = 1$ the remaining anomalous couplings vanishing. The straight dashed line indicates the mean in each plot.

Comparison with WHIZARD

For comparison with the WHIZARD program package the signed pull is determined. The pull between the results of the semi-analytical calculation and the results of WHIZARD for the cross-section as a function of the center-of-mass energy $\sqrt{s}$ is presented in figure 8.4(a) for $X_L^Z = 1$, in figure 8.4(b) for $X_R^Z = 1$, in figure 8.4(c) for $d_V^Z = 1$ and finally for $d_A^Z = 1$ in figure 8.4(d). Similar plots for the cross-section as a function of $\cos\theta'$ for a center-of-mass energy of $\sqrt{s} = 0.5$ TeV are shown in figure 8.5, similar ones for $\sqrt{s} = 1.0$ TeV in figure C.3 in appendix C.2.

The distribution of the values for the pulls suggests a qualitative accordance of the results of WHIZARD and the semi-analytical approach. Except of few outliers of the plots showing the dependence of $\cos\theta'$ all points are in the order of one.

8.4 Strategy to distinguish the anomalous couplings

8.4.1 Strategy to distinguish the anomalous couplings on parton level

In this subsection the question whether a distinction of the four anomalous couplings through measurement is feasible is addressed on parton level. Since a non-vanishing parameter for both the coupling X_L^Z and X_R^Z entails a global rescaling independent of the center-of-mass energy and of the angle between momenta of the top quark and the Z-boson, a determination of these couplings is not possible through the study of the dependences $\sigma(\sqrt{s})$ and $\sigma(\cos\theta')$. However, in order to distinguish the couplings d_V^Z and d_A^Z the analysis

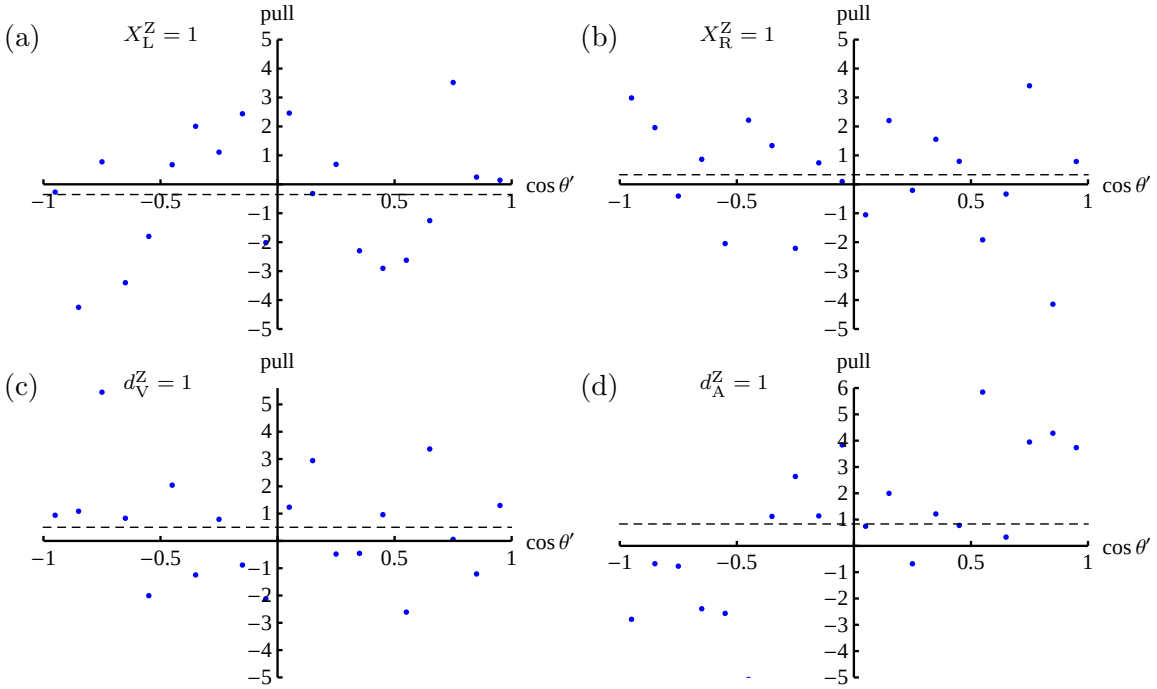

Figure 8.5: Pull between the results of the semi-analytical calculation and the ones of WHIZARD for the cross-section as a function of $\cos\theta'$ for the process $GG \to t\bar{t}Z$ ($\sqrt{s} = 0.5$ TeV; $m_{\mathrm{t}} = 172$ GeV). Figure (a) shows the pull for $X_{\mathrm{L}}^{\mathrm{Z}} = 1$, figure (b) for $X_{\mathrm{R}}^{\mathrm{Z}} = 1$, figure (c) for $d_{\mathrm{V}}^{\mathrm{Z}} = 1$ and figure (d) for $d_{\mathrm{A}}^{\mathrm{Z}} = 1$ the remaining anomalous couplings vanishing. The straight dashed line indicates the mean in each plot.

of the total reaction cross-section as a function of the center-of-mass energy in the preceding section suggested that the strategy presented in subsection 7.3.1 can be adopted. One of the measurements of the normalized deviation $\delta\sigma$ should be carried out around $\sqrt{s} = 0.5$ TeV, the second one sufficiently above this value, for example at $\sqrt{s} = 0.75$ TeV. First of all the $\sqrt{s}$ independent contribution has to be determined and removed. Having done this, the $\sqrt{s}$ dependent part is considered. As illustrated in figure 8.6 showing the dependence of $\delta\sigma$ on $d_{\mathrm{V}}^{\mathrm{Z}}$ and $d_{\mathrm{A}}^{\mathrm{Z}}$ at (a) $\sqrt{s} = 0.5$ TeV and (b) $\sqrt{s} = 0.75$ TeV, the contour lines of both plots cross each other in a sufficiently large angle such that the values of the two anomalous couplings can be extracted at the intersecting of two lines (for an example see figure 8.8(a)).

Alternatively, the coupling parameters $d_{\mathrm{V}}^{\mathrm{Z}}$ and $d_{\mathrm{A}}^{\mathrm{Z}}$ can also be determined by the analysis of the dependence of the cross-section on $\cos\theta'$. For this purpose, the normalized deviation $\delta\sigma$ is measured for the cross-section separately in the range $\cos\theta' < 0$ and $\cos\theta' > 0$ at the same center-of-mass energy. Combining the measured values for $\delta\sigma$ in a way analogous to the procedure presented before, the values for $d_{\mathrm{V}}^{\mathrm{Z}}$ and $d_{\mathrm{A}}^{\mathrm{Z}}$ can be read at the intersection of the contour lines (for an example see figure 8.8(b)). The calculated deviation $\delta\sigma$ is shown as a two dimensional contour plot of $d_{\mathrm{V}}^{\mathrm{Z}}$ and $d_{\mathrm{A}}^{\mathrm{Z}}$ in figure 8.7(a) for $\cos\theta' < 0$ and in figure 8.7(b) for $\cos\theta' > 0$.

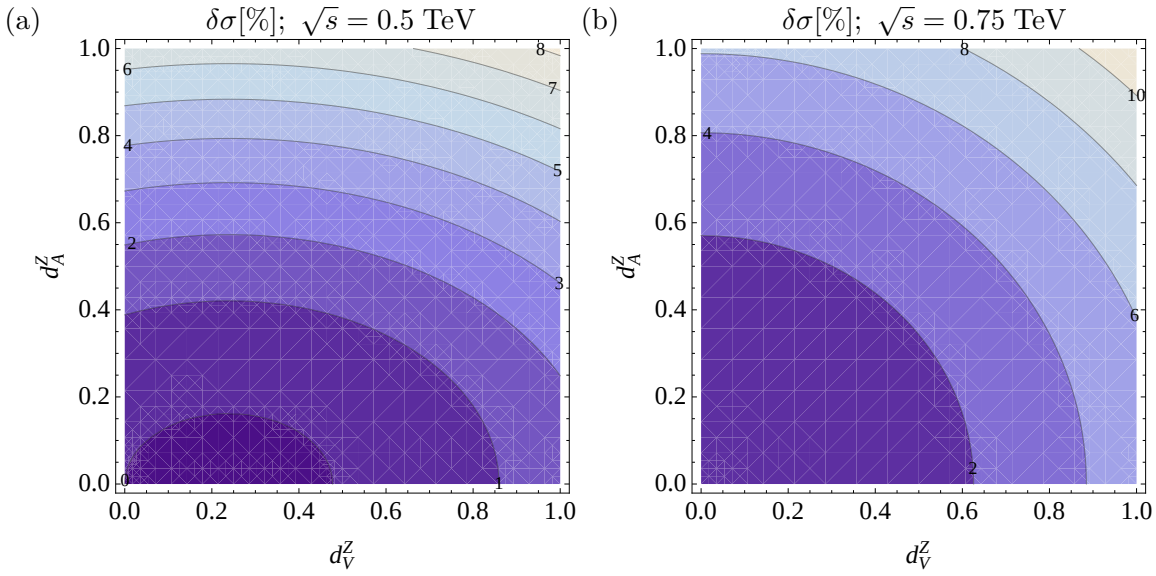

Figure 8.6: Normalized deviation $\delta\sigma = (\sigma_{\text{anom.}} - \sigma_{\text{SM}})/\sigma_{\text{SM}}$ in percent of the cross-section with anomalous couplings $\sigma_{\text{anom.}}$ from the SM cross-section σ_{SM} as a function of the two anomalous couplings d_{V}^{Z} and d_{A}^{Z} ($m_{\text{t}} = 172$ GeV). Figure (a) shows the calculated values for the definite center-of-mass energy of $\sqrt{s} = 0.5$ TeV, figure (b) for $\sqrt{s} = 0.75$ TeV.

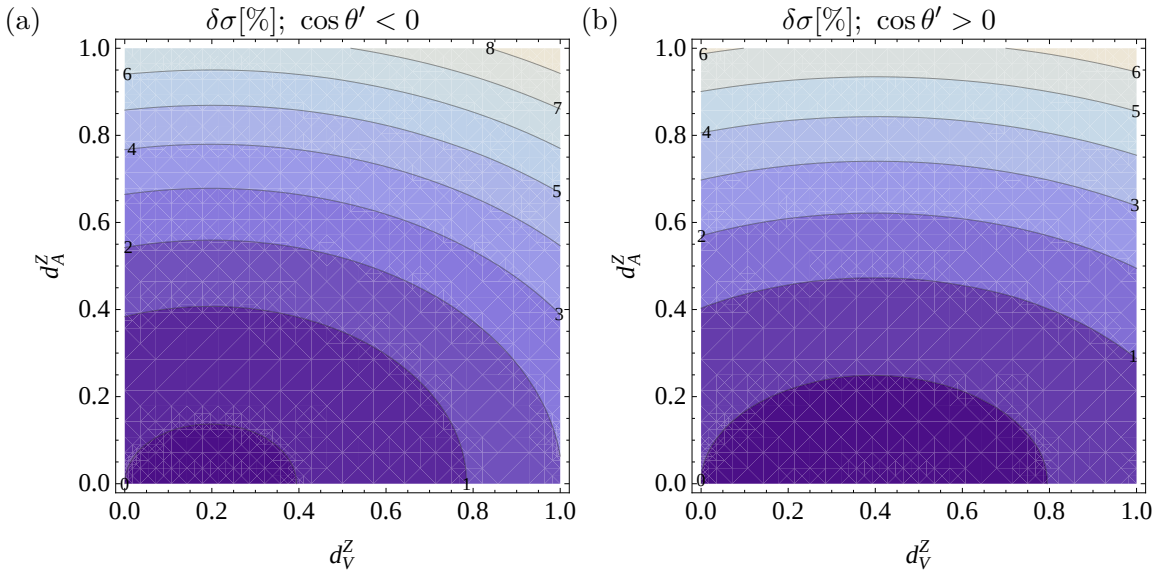

Figure 8.7: Normalized deviation $\delta\sigma = (\sigma_{\text{anom.}} - \sigma_{\text{SM}})/\sigma_{\text{SM}}$ in percent of the cross-section with anomalous couplings $\sigma_{\text{anom.}}$ from the SM cross-section σ_{SM} as a function of the two anomalous couplings d_{V}^{Z} and d_{A}^{Z} ($\sqrt{s} = 0.5$ TeV; $m_{\text{t}} = 172$ GeV). Figure (a) shows the calculated values for the range $\cos\theta' < 0$, figure (b) for the range $\cos\theta' > 0$.

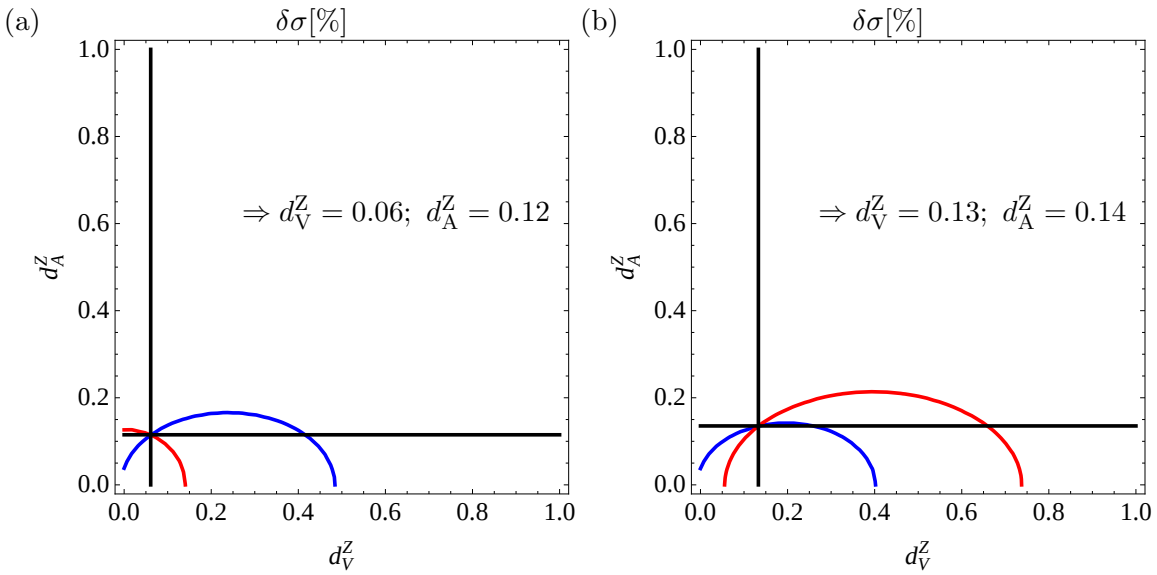

Figure 8.8: Examples for the determination of the two anomalous couplings $d_{\mathrm{V}}^{\mathrm{Z}}$ and $d_{\mathrm{A}}^{\mathrm{Z}}$ through measurement. Figure (a) illustrates the procedure, where the total reaction cross-section is measured at two different center-of-mass energies. A measured deviation $\delta\sigma$ of 0.01% at $\sqrt{s} = 0.5$ TeV (blue curve) and of 0.1% at $\sqrt{s} = 0.75$ TeV (red curve) is assumed. The combination of both measurements would restrict the parameters to $d_{\mathrm{V}}^{\mathrm{Z}} = 0.06$ and $d_{\mathrm{A}}^{\mathrm{Z}} = 0.12$ in this case. Figure (b) illustrates the procedure, where the cross-section is measured separately in the regions $\cos\theta' < 0$ and $\cos\theta' > 0$ at $\sqrt{s} = 0.5$ TeV. A measured deviation $\delta\sigma$ of 0.01% for $\cos\theta' < 0$ (blue curve) and of -0.1% for $\cos\theta' > 0$ (red curve) is assumed. The combination of both measurements would restrict the parameters to $d_{\mathrm{V}}^{\mathrm{Z}} = 0.13$ and $d_{\mathrm{A}}^{\mathrm{Z}} = 0.14$ in this case.

8.4.2 Strategy to distinguish the anomalous couplings including the convolution with the PDFs

Since at a hadron collider, such as the LHC, the momenta of the initial state gluons and thus the exact center-of-mass energy are a priori not known, only the cross-section convoluted with the PDFs is experimentally accessible. Hence, the aim of this subsection is to examine whether the strategies introduced before are still feasible on hadron level. Since it was shown that the couplings $X_{\mathrm{L}}^{\mathrm{Z}}$ and $X_{\mathrm{R}}^{\mathrm{Z}}$ cannot even be distinguised on parton level, the focus is shifted to the remaining couplings $d_{\mathrm{V}}^{\mathrm{Z}}$ and $d_{\mathrm{A}}^{\mathrm{Z}}$. Again, this analysis is done with the `WHIZARD` event generator program package using the PDF description CTEQ6L1 [51]. The analysis is based on samples with around $3.6 \cdot 10^6$ events each, which corresponds to an integrated luminosity of $10^5 fb^{-1} = 10^2 ab^{-1}$ at a center-of-mass energy (of the proton system) of $\sqrt{\hat{s}} = 7.0$ TeV[1]. The top quark width is set to $\Gamma_{\mathrm{t}} = 1.523$ GeV. In order to keep the computational effort as well as the needed amount of disc space modest, it is assumed that the deviation of the cross-section including anomalous couplings from the SM cross-section $\delta\sigma$ can be written in good approximation as $\delta\sigma = \delta\sigma(d_{\mathrm{V}}^{\mathrm{Z}}) + \delta\sigma(d_{\mathrm{A}}^{\mathrm{Z}})$ for sufficiently small values of the anomalous couplings. This assumption showed to be fully in accordance with the actual values on partonic level. Hence, only samples are generated where either $d_{\mathrm{V}}^{\mathrm{Z}} > 0$ or $d_{\mathrm{A}}^{\mathrm{Z}} > 0$ going from 0.1 to 1 in steps of 0.1, and, additionally, one sample for the SM parameters.

[1] In this subsection the center-of-mass energy of the proton system is denoted by $\sqrt{\hat{s}}$ in order not to be confused with the center-of-mass energy $\sqrt{s}$ on parton level.

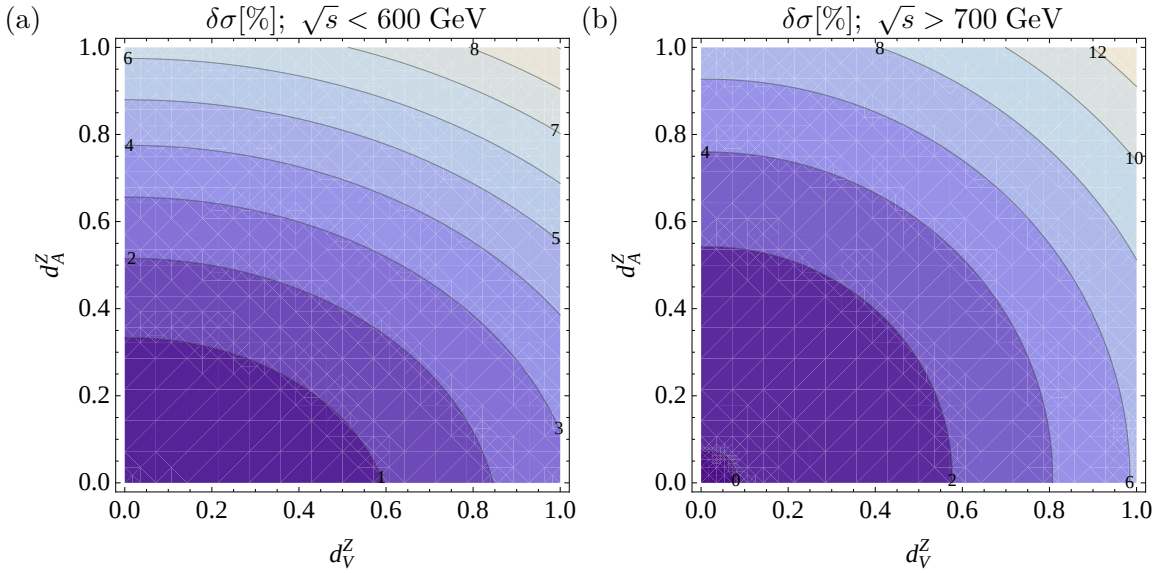

Figure 8.9: Normalized deviation $\delta\sigma = (\sigma_{\text{anom.}} - \sigma_{\text{SM}})/\sigma_{\text{SM}}$ in percent of the cross-section with anomalous couplings $\sigma_{\text{anom.}}$ from the SM cross-section σ_{SM} as a function of the two anomalous couplings d_{V}^{Z} and d_{A}^{Z} ($\sqrt{\hat{s}} = 7.0$ TeV; $m_{\text{t}} = 172$ GeV). Figure (a) shows the dependence for events in the range $\sqrt{s} < 600$ GeV, figure (b) for the ones with $\sqrt{s} > 700$ GeV.

Taking into account the dependence of the hard scattering cross-section as a function of the center-of-mass energy (see figure 8.3(b)), the most obvious way to adopt the strategy involving the analysis of $\sqrt{s}$ is to divide the events into two classes: the first one containing all events with $\sqrt{s} < \sqrt{s_1}$, the second class the events with $\sqrt{s} > \sqrt{s_2}$, where the threshold energies $\sqrt{s_1}$ and $\sqrt{s_2}$ have to be chosen adequately. The Monte Carlo study showed that good results are achieved with $\sqrt{s_1} = 600$ GeV and $\sqrt{s_2} = 700$ GeV. The dependence of $\delta\sigma$ on the parameters d_{V}^{Z} and d_{A}^{Z} as obtained from the analysis of the Monte Carlo event samples is shown in figure C.5 of appendix C.3. A quadratic dependence on the anomalous couplings is evident. Thus, for each of the four plots a function of the form $a\,(d_{\text{V/A}}^{\text{Z}})^2 + b\,d_{\text{V/A}}^{\text{Z}} + c$ is fitted to the Monte Carlo data. These functions as well as the fit parameters are also shown in figure C.5. The one-dimensional graphs can then be combined to get two-dimensional plots $\delta\sigma(d_{\text{V}}^{\text{Z}}, d_{\text{A}}^{\text{Z}})$, as shown in figure 8.9(a) for $\sqrt{s} < 600$ GeV and figure 8.9(b) for $\sqrt{s} > 700$ GeV. Assuming that it is possible to measure the deviation $\delta\sigma$ for both classes, the values for the anomalous parameters can be determined analogously to the approach presented in the previous subsection. The procedure is moreover illustrated in figure 8.10(a). The main disadvantage of this method is the point that it depends on the determination of the invariant mass of the two top quarks and the Z-boson. The energy of the neutrino being not detectable, this is however rather challenging since top quark pair events are usually investigated in the semi-leptonic decay channel (cf. section 2.3). Still the approach seems to be promising because it does not rely on the precise measurement of the invariant mass but rather on the decision whether the invariant mass is below or above specific thresholds. Thus, by employing sophisticated event reconstruction algorithms (see for instance Ref. [4]), this problem should be overcome.

Nonetheless, a further strategy to distinguish the anomalous couplings, which does not rely on the full reconstruction of the $t\bar{t}Z$-event, is presented in the following. Involving the analysis of the cross-section as a function of $\cos\theta'$, this method is completely similar to the one discussed for the hard scattering cross-section, i. e. the deviation $\delta\sigma$ is determined

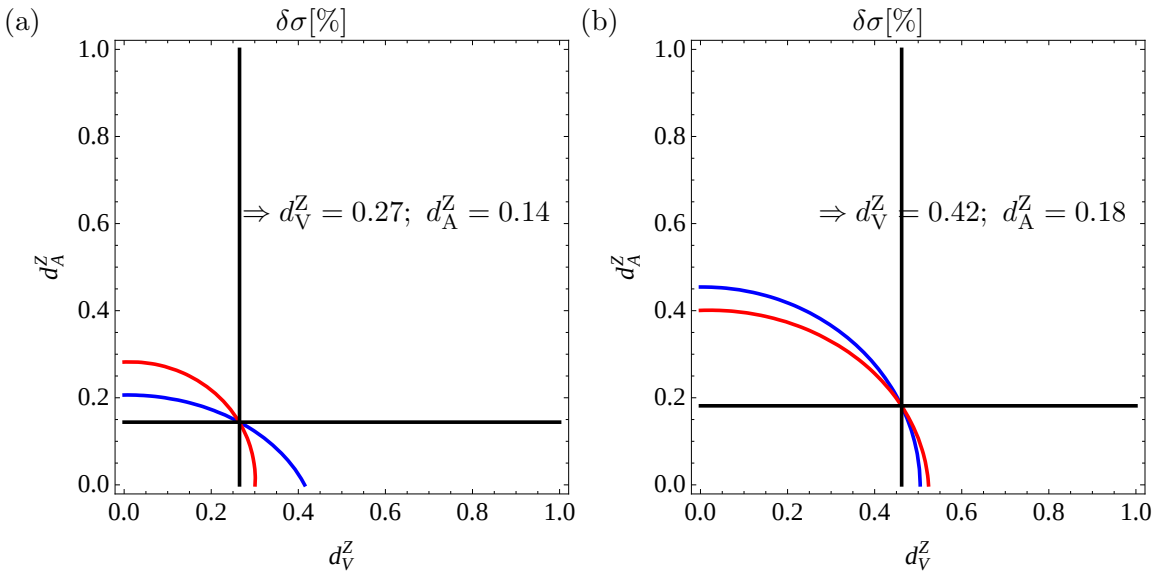

Figure 8.10: Examples for the determination of the two anomalous couplings $d_{\mathrm{V}}^{\mathrm{Z}}$ and $d_{\mathrm{A}}^{\mathrm{Z}}$ through measurement. Figure (a) illustrates the procedure where the deviation $\delta\sigma$ is measured separately for events with $\sqrt{s} < 600$ GeV and $\sqrt{s} > 700$ GeV. A measured deviation $\delta\sigma$ of 0.5% both for $\sqrt{s} < 600$ GeV (blue curve) and $\sqrt{s} > 700$ GeV (red curve) is assumed. The combination of both measurements would restrict the parameters to $d_{\mathrm{V}}^{\mathrm{Z}} = 0.27$ and $d_{\mathrm{A}}^{\mathrm{Z}} = 0.14$ in this case. Figure (b) illustrates the procedure, where the deviation $\delta\sigma$ is measured separately for $\cos\theta' < 0$ and $\cos\theta' > 0$. A measured deviation $\delta\sigma$ of 1.5% for $\cos\theta' < 0$ (blue curve) and of 1.0% for $\cos\theta' > 0$ (red curve) is assumed. The combination of both measurements would restrict the parameters to $d_{\mathrm{V}}^{\mathrm{Z}} = 0.42$ and $d_{\mathrm{A}}^{\mathrm{Z}} = 0.18$ in this case.

separately for $\cos\theta' < 0$ and $\cos\theta' > 0$. Yet, in lieu of a definite (hard scattering) center-of-mass energy $\sqrt{s}$ the deviation $\delta\sigma$ involves now events with all possible values for $\sqrt{s}$ due to the convolution with the PDFs. For the following Monte Carlo study the same assumption on $\delta\sigma$ as in the preceding paragraph is made, that is to say $\delta\sigma = \delta\sigma(d_{\mathrm{V}}^{\mathrm{Z}}) + \delta\sigma(d_{\mathrm{A}}^{\mathrm{Z}})$. As before, $\delta\sigma$ shows approximately a quadratic dependence on the coupling parameters $d_{\mathrm{V}}^{\mathrm{Z}}$ and $d_{\mathrm{A}}^{\mathrm{Z}}$ (see figure C.6 in section C.3 of the appendix), which suggests to fit a function of the form $a\, t_{\mathrm{V/A}}^2 + b\, t_{\mathrm{V/A}} + c$ to the Monte Carlo data. The resulting $\delta\sigma(d_{\mathrm{V}}^{\mathrm{Z}}, d_{\mathrm{A}}^{\mathrm{Z}})$ contour plots for $\cos\theta' < 0$ and $\cos\theta' > 0$ are presented in figure 8.11(a) and (b), respectively. As illustrated in figure 8.10(b), with the information of the measurement for the two ranges of $\cos\theta'$ the determination of $d_{\mathrm{V}}^{\mathrm{Z}}$ and $d_{\mathrm{A}}^{\mathrm{Z}}$ is feasible in general. However, since the angle of intersection of the two contour lines is rather small, a precise determinination of the two coupling parameters is very challenging. It is speculated that this angle increases when considering only events where the invariant mass of the two top quarks and the Z-boson is required to be below a threshold $\sqrt{s_1} \sim 600$ GeV. This would however re-introduce the problem of the difficult determination of the invariant mass.

In conclusion, the strategies discussed above represent two independent approaches, which allow for the determination of the anomalous couplings $d_{\mathrm{V}}^{\mathrm{Z}}$ and $d_{\mathrm{A}}^{\mathrm{Z}}$ under ideal circumstances. However, similar difficulties as mentioned for the γtt vertex arise. Among those are potential further anomalous couplings of the Gtt vertex and the large expected experimental error for the measurement of $t\bar{t}$-cross-sections. The latter is even more severe for the process $GG \to t\bar{t}Z$ since the total reaction cross-section is only about one tenth compared to the process $GG \to t\bar{t}\gamma$. Hence, one cannot expect a precise determination of the

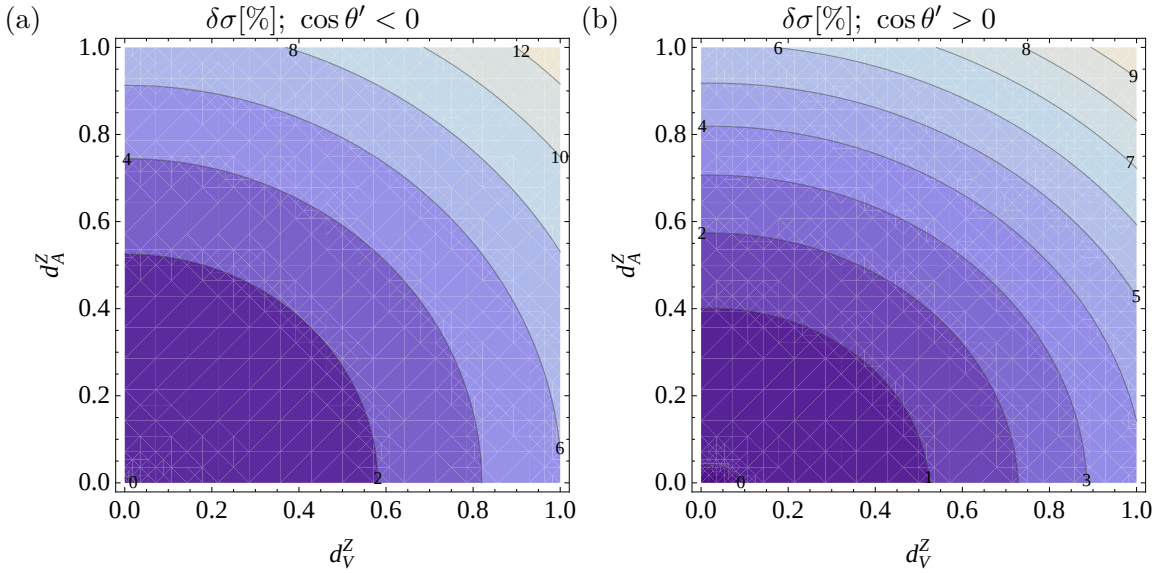

Figure 8.11: Normalized deviation $\delta\sigma = (\sigma_{\text{anom.}} - \sigma_{\text{SM}})/\sigma_{\text{SM}}$ in percent of the cross-section with anomalous couplings $\sigma_{\text{anom.}}$ from the SM cross-section σ_{SM} as a function of the two anomalous couplings d_{V}^{Z} and d_{A}^{Z} ($\sqrt{\hat{s}} = 7.0$ TeV; $m_{\text{t}} = 172$ GeV). Figure (a) shows the dependence for events with $\cos\theta' < 0$, figure (b) for events with $\cos\theta' > 0$.

anomalous Ztt-couplings through the analysis of the process $GG \to t\bar{t}Z$ at the LHC. Yet, using the methods described here allows to give upper limits on these couplings, where the limits will depend on the achieved experimental accuracy.

9 Quantitative comparison with Whizard

9.1 Comparing the means of two normally distributed populations

This chapter addresses the question whether all the results of the semi-analytical calculation and the ones of `WHIZARD` are in accordance with each other or whether a significant deviation is found. Since both the semi-analytical approach and the `WHIZARD` program package make use of numerical integration techniques, the achieved results are not analytically exact numbers but are rather given by an estimate for the integral together with its estimated error. Hence, for a rigorous comparison, one has to compute the value for the cross-section for definite parameters, such as the center-of-mass energy, masses and couplings, sufficiently often with both calculation methods. Then the statistical analysis of these samples allows to decide whether or not both approaches show a significant deviation. This is exemplified for the computation of the hard-scattering total reaction cross-section for the process $GG \to t\bar{t}\gamma$ for the definite parameters $\sqrt{s} = 1.0$ TeV and $m_\mathrm{t} = 172$ GeV with SM top quark couplings neglecting the top quark width. Moreover, the additional cut on the minimal energy of the photon of $E_{\mathrm{k,min}} = 5$ GeV is applied. The estimate for the cross-section is calculated $n_\mathrm{sa} = n_\mathrm{Wh} = 1000$ times with an estimated relative error of approximately 10^{-3} employing both the semi-analytical approach and `WHIZARD`. The probability density of all results is shown in figure 9.1(a), whose analysis allows to draw several conclusions: Obviously, the values are normally distributed with a specific mean μ and standard deviation s, the values of which are stated in table 9.1 both for the semi-analytical calculation (μ_sa and s_sa) and for the calculation with `WHIZARD` (μ_Wh and s_Wh). Knowing these numbers, the hypothesis that the means of the two samples are the same ($\mathcal{H}_0$: $\mu_\mathrm{sa} = \mu_\mathrm{Wh}$) can be probed by applying the two sample z-test[1] for independent samples (see e. g. Ref. [52, 53]). The corresponding standard score, that is to say the distance of both means in units of the combined standard error, is calculated as

$$z = \frac{\mu_\mathrm{sa} - \mu_\mathrm{Wh}}{\sqrt{\frac{s_\mathrm{sa}^2}{n_\mathrm{sa}} + \frac{s_\mathrm{Wh}^2}{n_\mathrm{Wh}}}} = \frac{221.386 - 221.469}{\sqrt{\frac{0.221433^2}{1000} + \frac{0.455078^2}{1000}}} = -5.193. \tag{9.1}$$

This leads to the conclusion that the null hypothesis $\mathcal{H}_0$ is rejected with a confidence level of $(100 - 10^{-5})\%$. The same test is done once more, where the estimated relative error for each value for the cross-section is now reduced to approximately 10^{-4}. Figure 9.1(b) shows the corresponding probability densities. With the obtained values for the means and standard deviations listed in table 9.1 a standard score of even $z = -8.029$ is obtained.

Yet, note that the means of all four statistics samples are fully in accordance with each other within their standard deviations (cf. table 9.1). It is only due to the fact that

[1] This test is sometimes also referred to as two sample Gauss-test.

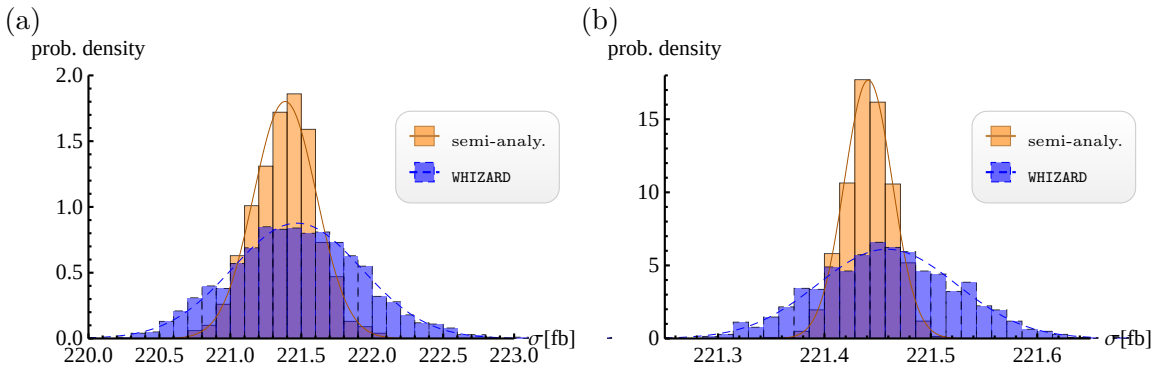

Figure 9.1: Probability density of the value for the cross-section for the process $GG \to t\bar{t}\gamma$ ($\sqrt{s} = 1.0$ TeV; $m_t = 172$ GeV; $E_{k,min} = 5$ GeV). The statistics samples are based on 1000 calculations each. The distribution of the semi-analytic calculation (orange, solid lines) features a narrower Gaussian peak than the one of `WHIZARD` (blue, dashed lines). The curve indicate the probability density of the normal distribution with mean and standard deviation of the corresponding sample. The estimated relative error for each value of the cross-section is $\approx 10^{-3}$ in figure (a) and $\approx 10^{-4}$ in figure (b).

	est. relative error $\approx 10^{-3}$		est. relative error $\approx 10^{-4}$	
	semi-analy. calc.	`WHIZARD`	semi-analy. calc.	`WHIZARD`
mean μ [fb]	221.386	221.469	221.441	221.459
stdev. s [fb]	0.2214	0.4551	0.02257	0.06534
mean est. stdev. $\bar{s}_{est.}$ [fb]	0.2156	0.2319	0.02209	0.02693
$s/\bar{s}_{est.}$	1.03	1.96	1.02	2.43

Table 9.1: Properties of the statistical samples of the values for the cross-section for the process $GG \to t\bar{t}\gamma$ ($\sqrt{s} = 1.0$ TeV; $m_t = 172$ GeV; $E_{k,min} = 5$ GeV). The first row gives the mean of the statistics sample, the second row its standard deviation. The mean of the estimated standard deviation stated by the Monte Carlo integrator is printed in the third row.

the standard error $s/\sqrt{n}$, as encountered in the denominator for the computation of the standard score (9.1), can become arbitrarily small for a sufficiently large size n of the sample that the z-test discloses the slight discrepancy. If samples with lower statistics were considered, the absolute value of the standard score would be smaller. A closer look suggests to interpret the discrepancy rather as a slight convergence problem of the semi-analytical calculation than a disagreement of both calculation methods for the following reasons. The absolute deviation of the means of both samples is reduced by a factor of 4.7 comparing the one for the samples with lower precision with the one for the samples with higher precision. Whereas the mean of the `WHIZARD` sample with higher precision remains almost unchanged compared to the one with lower precision, a shifting of the mean to higher values, that is to say to the means of the `WHIZARD` samples, is observed for the semi-analytical calculation. This shifting is so large that a z-test for the two semi-analytical samples with lower precision and higher precision would come to the conclusion that the hypothesis that both samples have the same mean would be rejected with a confidence level of $(100 - 10^{-13})\%$ (standard score $z = -7.87671$).

Moreover, the analysis of the samples allows also to check the stated estimated error of the numerical integration. Comparing the numbers for the actual standard deviation of the sample with the mean estimated standard deviation stated by the Monte Carlo integrator shows that they are fully in accordance with each other for the semi-analytical calculation (see last row in table 9.1). However, the error is underestimated by a factor of ~ 2 by `WHIZARD`.

An analogous study for the process $GG \to t\bar{t}Z$ with the definite parameters $\sqrt{s} = 1.0$ TeV, $m_\mathrm{t} = 172$ GeV and $\Gamma_\mathrm{t} = 0$ with SM top quark couplings arrives at similar conclusions as for the process $GG \to t\bar{t}\gamma$. As before, the hard-scattering total reaction cross-section is computed 1000 times using both the semi-analytical approach and `WHIZARD`. The probability density is presented for samples with an estimated relative error of $\approx 10^{-3}$ and $\approx 10^{-4}$ in figure 9.2(a) and (b), respectively. Again, the z-test is employed to test the hypothesis that the means of the two samples are the same. The values for the means and standard deviations are given in table 9.2. For the samples with a relative error of $\approx 10^{-3}$ the standard score is $z = -3.97346$, whereas one yields $z = -6.37669$ for the samples with higher precision. Consequently, the null hypothesis is rejected with a confidence level very close to 100%. It is remarked, however, that the means of the four samples are fully in accordance with each other within their standard deviations. As in case of the process $GG \to t\bar{t}\gamma$, the origin of the discrepancy disclosed by the z-test is supposed to be a slight convergence problem of the semi-analytical approach. As before, the mean remains approximately unchanged for the `WHIZARD` samples when increasing the numerical precision. On the contrary, the mean moves to larger values for the semi-analytical calculation. With a standard score of $z = -7.12889$, the two means of the semi-analytical approach for the two tested accuracies significantly differ. Moreover, also for the process $GG \to t\bar{t}Z$ the analysis of the standard deviation of the sample and the mean stated estimated standard deviation indicates that `WHIZARD` gives a too optimistic error estimate. The actual standard deviation is found to be larger by a factor of ~ 2.

Since it is not feasibly to carry out a rigorous z-test for each point in the parameter space, a test involving the pull is used instead. The squared pull of a sample $x_1, x_2, \cdots, x_n$ of a normally distributed statistical population, i. e. the quantity $(x_i - \mu)^2/s^2$, where μ denotes the known expectation value and s the variance, is χ^2-distributed with one degree of freedom [54]. This still holds in case where the pull between two normally distributed samples

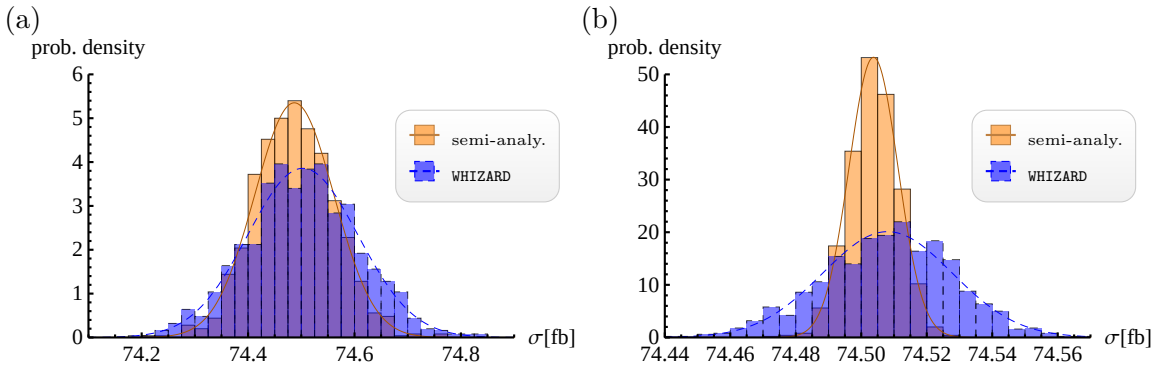

Figure 9.2: Probability density of the value for the cross-section for the process $GG \to t\bar{t}Z$ ($\sqrt{s} = 1.0$ TeV; $m_t = 172$ GeV). The statistics samples are based on 1000 calculations each. The distribution of the semi-analytic calculation (orange, solid lines) features a narrower Gaussian peak than the one of `WHIZARD` (blue, dashed lines). The curves indicate the probability density of the normal distribution with mean and standard deviation of the corresponding sample. The estimated relative error for each value of the cross-section is $\approx 10^{-3}$ in figure (a) and $\approx 10^{-4}$ in figure (b).

	est. relative error $\approx 10^{-3}$		est. relative error $\approx 10^{-4}$	
	semi-analy. calc.	`WHIZARD`	semi-analy. calc.	`WHIZARD`
mean μ [fb]	74.4869	74.5029	74.5037	74.5080
stdev. s [fb]	0.07455	0.1034	0.007492	0.01984
mean est. stdev. $\bar{s}_{\text{est.}}$ [fb]	0.07324	0.0623	0.007437	0.008511
$s/\bar{s}_{\text{est.}}$	1.02	1.66	1.01	2.33

Table 9.2: Properties of the statistical samples of the values for the cross-section for the process $GG \to t\bar{t}Z$ ($\sqrt{s} = 1.0$ TeV; $m_t = 172$ GeV). The first row gives the mean of the statistics sample, the second row its standard deviation. The mean of the estimated standard deviation stated by the Monte Carlo integrator is printed in the third row.

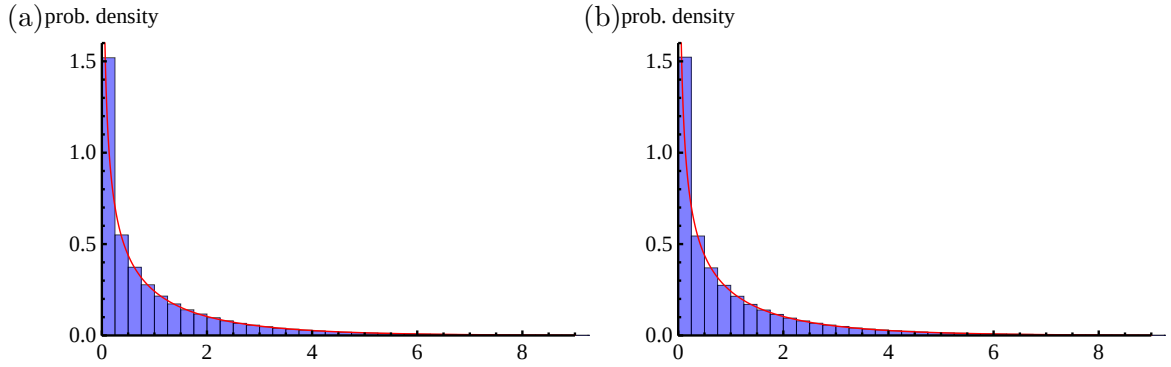

Figure 9.3: Propability density for the squared values of the pull between the sample of the semi-analytical approach and WHIZARD for the process $GG \to t\bar{t}\gamma$ (figure (a)) and the process $GG \to t\bar{t}Z$ (figure (b)). Both plots are based on the samples with an estimated relative error of $\approx 10^{-3}$. The solid curve indicates the propability density function for the χ^2-distribution with one degree of freedom.

x_i and y_j, defined as $(x_i - y_j)/\sqrt{s_x^2 + s_y^2}$, is considered. As illustrated in figure 9.3 the squared pull between the sample of the semi-analytical approach and WHIZARD is precisely χ^2-distributed with one degree of freedom both for the process $GG \to t\bar{t}\gamma$ (figure 9.3(a)) and $GG \to t\bar{t}Z$ (figure 9.3(b)). This means that the distances $x_i - y_j$ are distributed as expected for one combined sample of a normally distributed statistical population with mean $\mu = \mu_{\text{sa}} = \mu_{\text{Wh}}$ and standard deviation $\sqrt{s_{\text{sa}}^2 + s_{\text{Wh}}^2}$. Consequently, the conclusion may be drawn that the results of both calculation approaches are in accordance with each other within their errors. Note that, if the standard deviation stated by the WHIZARD program was used instead of the actual standard deviation of the WHIZARD sample, the values of the pull would not be χ^2-distributed with one degree of freedom but the distribution would be somewhat broader. Hence, in the following sections the estimated error of the integral of the computation of WHIZARD is supplied with a fudge factor to correct for the underestimated error.

9.2 Analysis of the distribution of the pull for the process $GG \to t\bar{t}\gamma$

To test the accordance of the results of WHIZARD with the semi-analytical computation on a more quantitative level for the process $GG \to t\bar{t}\gamma$, the distribution of the pull for this process is examined in this section. As argued in the preceding section, the values for the pull for each pair of results for the cross-section is recalculated providing a fudge factor for the estimated error of the calculation of WHIZARD. Assuming that the error is underestimated by approximately the same extend in the whole parameter space of interest, this factor is chosen to be 2 for all pulls. The resulting probability density of the pull is shown in figure 9.4(a). This plot contains both the obtained values for the pull with SM couplings with and without consideration of the top quark width and the values for the pull with anomalous couplings. All in all the statistics sample is based on 174 values. The probability density is well approximated by the one of the χ^2-distribution with one degree of freedom. This is even more evident when comparing the cumulative distribution function (see figure 9.4(b)). Consequently, the hypothesis that both calculation approaches

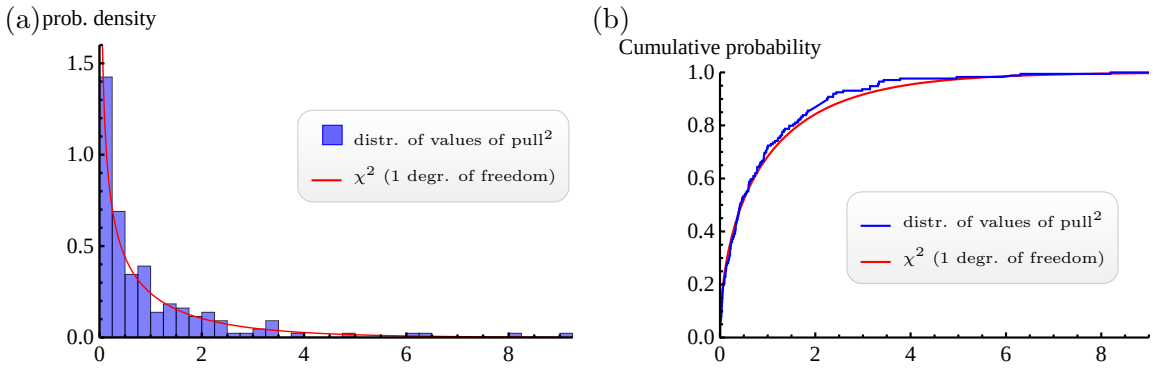

Figure 9.4: Probability density (a) and cumulative probability function (b) for all squared values of the pull for the process $GG \to t\bar{t}\gamma$. For comparison the corresponding function for the χ^2-distribution with one degree of freedom is indicated (red line).

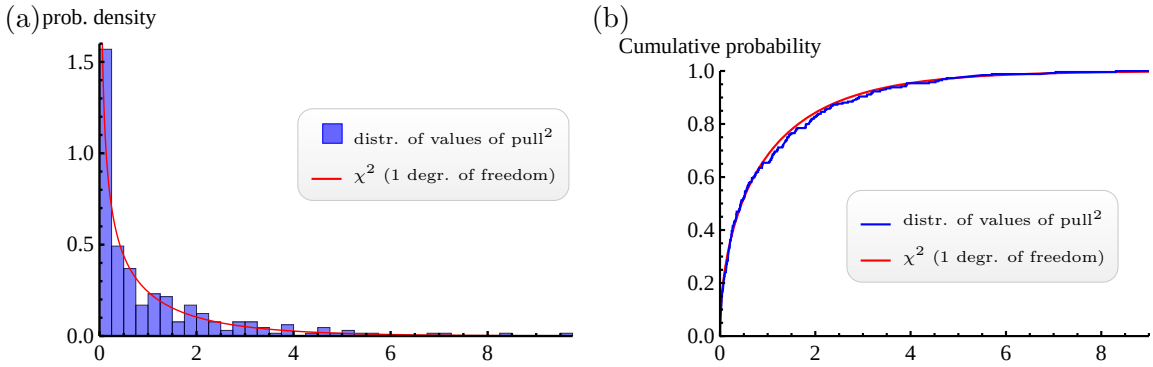

Figure 9.5: Probability density (a) and cumulative probability function (b) for all squared values of the pull for the process $GG \to t\bar{t}\gamma$. For comparison the corresponding function for the χ^2-distribution with one degree of freedom is indicated (red line).

yield compatible results for the cross-section for the process $GG \to t\bar{t}\gamma$ can not be rejected on a significant level.

9.3 Analysis of the distribution of the pull for the process $GG \to t\bar{t}Z$

Analogously to the previous section, the distribution of the values for the pull for the process $GG \to t\bar{t}Z$ is analyzed for a more quantitative comparison of the results of `WHIZARD` with the semi-analytical approach. All values for the pull are recalculated providing a fudge factor of 2 for the estimated error of the computation of `WHIZARD`. The statistics sample involves all values for the pull discussed in chapter 8 for the SM and the vertex with anomalous couplings. Including those values shown in appendix C the sample contains all in all 260 values. Looking at the resulting probability density (figure 9.5(a)) and the cumulative distribution function (see figure 9.5(b)) the accordance with the χ^2-distribution with one degree of freedom is apparent. Hence, also for the process $GG \to t\bar{t}Z$ a disagreement between the results of `WHIZARD` and those of the semi-analytical approach cannot be established.

10 Conclusion

In this thesis the γtt and Ztt vertices including anomalous couplings generated by dimension-six gauge invariant operators were analyzed. For this purpose, the two processes $GG \to t\bar{t}\gamma$ and $GG \to t\bar{t}Z$ were considered, which required the use of a three-particle phase space parameterization for massive particles. The problematic structure of the propagators involved in the Feynman amplitudes for these processes entailed the use of multi-channel Monte Carlo integration techniques to overcome the slow convergence for the integral of the differential cross-section.

One of the main issues of this thesis dealt with the question whether the unknown anomalous top quark photon and top quark Z-boson coupling parameters could be extracted from experimental measurements at the LHC. Apart from the coupling $f_{\mathrm{V}}^{\mathrm{A}}$, which just implies a global rescaling of the total reaction cross-section, the general γtt vertex comes with two anomalous couplings $d_{\mathrm{V}}^{\mathrm{A}}$ and $d_{\mathrm{A}}^{\mathrm{A}}$. As their effect on the total reaction cross-section depends on the partonic center-of-mass energy, a strategy to distinguish these two couplings in a fictitious experimental measurement on parton level could be formulated. However, the relative deviation of the cross-section including anomalous couplings to the SM cross-section was too small to be still extractable after convoluting the hard scattering cross-section with the PDFs. Hence, the presented approach does not allow for a determination of the anomalous γtt couplings by means of the analysis of total reaction cross-section for the process $GG \to t\bar{t}\gamma$ at the LHC at a center-of-mass energy of $\sqrt{s} = 7$ TeV. Hence, future studies of promising differential cross-sections are required to search for appropriate observables.
For the general Ztt vertex there are four anomalous coupling parameters to be considered. While two of them (couplings $X_{\mathrm{L}}^{\mathrm{Z}}$ and $X_{\mathrm{R}}^{\mathrm{Z}}$) just induce a global rescaling of the total reaction cross-section independent of the center-of-mass energy $\sqrt{s}$ of the process and the angular distribution of the final state particles, a significant dependence on $\sqrt{s}$ and on the cosine of the angle between the three-momentum of the top quark and the one of the Z-boson ($\cos\theta'$) was observed for the couplings $d_{\mathrm{V}}^{\mathrm{Z}}$ and $d_{\mathrm{A}}^{\mathrm{Z}}$. This allowed to formulate two independent strategies to determine these two couplings through a fictitious experiment on parton level. The first approach involves the measurement of the cross-section at different center-of-mass energies, whereas the second one employs the dependence of the cross-section on $\cos\theta'$. Since the impact of the anomalous couplings is considerably larger for the Ztt vertex than for the γtt vertex, after convoluting the hard scattering cross-section with the PDFs, analogous strategies still seemed promising. Yet, a precise determination of the anomalous Ztt-couplings did not seem realistic at the current center-of-mass energy at the LHC due to the rather large expected experimental error for the measurement of $t\bar{t}$ cross-sections.

Moreover, another main goal of this work was the comparison of the results of the semi-analytical calculation with the ones of `WHIZARD` [19], the generic Monte Carlo integration and event generation package for multi-particle processes. Values of both calculation approaches for the total reaction hard scattering cross-section as a function of the center-of-mass energy, $\cos\theta'$ and the top quark mass were compared with each other for the

processes $GG \to t\bar{t}\gamma$ and $GG \to t\bar{t}Z$ for SM top quark couplings both with and without consideration of the top quark width and, additionally, for anomalous couplings neglecting the top quark width. For each pair of values the pull was computed, i. e. the quantity $(\sigma_{\mathrm{sa}}-\sigma_{\mathrm{Wh}})/(\sqrt{s_{\mathrm{sa}}^2 + s_{\mathrm{Wh}}^2})$, where σ_{sa} and σ_{Wh} are the estimated values for the cross-section and s_{sa} and s_{Wh} the estimated error for the semi-analytical calculation and `WHIZARD`, respectively. Since all values for the pull were found to be in the order of one having estimated relative errors for the cross-section of approximately 10^{-4}, a good qualitative accordance of both calculation methods was established. Additionally, for a quantitative comparison of the results, the cross-section was computed 1000 times each for the same definite parameters using the semi-analytical approach and `WHIZARD`, which was accomplished for two different computational accuracies. By virtue of the large statistics of the samples, the analysis came to the following conclusions: Firstly, a slight convergence problem of the semi-analytical calculation was disclosed. As a consequence, a rigorous z-test suggested a significant deviation of the mean of the semi-analytical approach from the one of `WHIZARD`, since, instead of the standard deviation, the standard error is involved by the z-test, which becomes small for a large sample size. Secondly, the error due to numerical integration is underestimated by a factor of around 2 by `WHIZARD`. The latter was taken into account by a corresponding fudge factor for the analysis of the distribution of all obtained values for the pull. This distribution turned out to be fully in accordance with the χ^2-distribution with one degree of freedom, which would be expected in case of consistent results of both calculation approaches.

Since the reliability of the results of `WHIZARD` for cross-sections of processes with a three-particle final state including anomalous top quark couplings has significantly been established by comparison with a semi-analytical approach in this thesis, the `WHIZARD` program package is predestined for future top quark studies. Thus, analyzes of events generated by `WHIZARD` can facilitate the investigation of top quark anomalous couplings. This is of particular interest for the study of the general γtt vertex, where the analysis of differential cross-sections is favorable. In conclusion, the `WHIZARD` program package is a recommendable tool for the fully automated calculation and generation of multi-particle events, such as for processes involving top quark anomalous couplings.

A Calculation of the color factors

In this section the calculation of the color factors of all involved combinations of amplitudes of the process $GG \to t\bar{t}$ (see figure 7.1) is presented. The corresponding factor for the matrix element $|\mathcal{M}_A|^2$ was already given in section 7.1. The ghost graphs **D** and **E** having the same color structure, their color factor is identical to the one of graph **A**.

- Color factor for $|\mathcal{M}_B|^2$ and $|\mathcal{M}_C|^2$

$$\sum_{a,b,e,f} (t^a)_{ec}(t^b)_{cf}(t^b)_{f\tilde{c}}(t^a)_{\tilde{c}e} = \sum_{a,b} \mathrm{Tr}[t^a t^b t^b t^a] = \left(\frac{4}{3}\right)^2 \mathrm{Tr}[\mathbb{1}] = \frac{16}{3} \tag{A.1}$$

- Color factor for $\mathcal{M}_A\mathcal{M}_B^\dagger$

$$\begin{aligned}
\sum_{a,b,e,f} (t^c)_{ef} f^{abc} (t^b)_{f\tilde{c}}(t^a)_{\tilde{c}e} &= \sum_{a,b} f^{abc}\,\mathrm{Tr}[t^c t^b t^a] = \\
&= \sum_{a,b} f^{abc}\left(\mathrm{Tr}[t^c t^a t^b] + \mathrm{Tr}[t^c [t^b, t^a]]\right) = \\
&= \sum_{a,b} f^{abc}\,\mathrm{Tr}[t^c t^a t^b] + \sum_{a,b} f^{abc} f^{bad}\,\mathrm{Tr}[t^c t^d] = \\
&= \sum_{a,b} f^{bac}\,\mathrm{Tr}[t^c t^b t^a] - \mathrm{i}C_2(G)\,\mathrm{Tr}[t^c t^c] = \\
&= -\sum_{a,b} f^{abc}\,\mathrm{Tr}[t^c t^b t^a] - \mathrm{i}C_2(G)C_2(r=3)\,\mathrm{Tr}[\mathbb{1}] \\
\Rightarrow \sum_{a,b,e,f} (t^c)_{ef} f^{abc} (t^b)_{f\tilde{c}}(t^a)_{\tilde{c}e} &= -\frac{1}{2}\mathrm{i}C_2(G)C_2(r=3)\,\mathrm{Tr}[\mathbb{1}] = -6\mathrm{i}
\end{aligned} \tag{A.2}$$

- Color factor for $\mathcal{M}_A\mathcal{M}_C^\dagger$

$$\sum_{a,b,e,f} (t^c)_{ef} f^{abc} (t^a)_{f\tilde{c}}(t^b)_{\tilde{c}e} = -\sum_{a,b,e,f} (t^c)_{ef} f^{abc} (t^b)_{f\tilde{c}}(t^a)_{\tilde{c}e} = 6\mathrm{i} \tag{A.3}$$

- Color factor for $\mathcal{M}_B\mathcal{M}_C^\dagger$

$$\sum_{a,b,e,f} (t^a)_{ec}(t^b)_{cf}(t^a)_{f\tilde{c}}(t^b)_{\tilde{c}e} = \mathrm{Tr}[t^a t^b t^a t^b] = \underbrace{\mathrm{Tr}[t^a t^b t^b t^a]}_{=\frac{16}{3}} + \mathrm{i}\underbrace{f^{abc}\,\mathrm{Tr}[t^a t^b t^c]}_{=6\mathrm{i}} = -\frac{2}{3} \tag{A.4}$$

B Feynman amplitudes

B.1 Feynman amplitudes for the processes $GG \to t\bar{t}\gamma$ and $GG \to t\bar{t}Z$

Process $GG \to t\bar{t}\gamma$

The corresponding Feynman amplitudes for the Feynman graphs shown in figure 7.3 of section 7.2 for the process $GG \to t\bar{t}\gamma$ read as follows:

$$\mathcal{M}_{A1} = \overline{u}_r(\mathbf{p}_\mathrm{t}) \left(-\mathrm{i}\frac{2}{3}e\right) \Gamma^\lambda \mathrm{i}\frac{\mathbf{p}_\mathrm{t} + \mathbf{k} + m_\mathrm{t}}{2\mathbf{p}_\mathrm{t}\cdot\mathbf{k}} \tilde{\mathcal{M}}_A v_s(\mathbf{p}_{\bar{\mathrm{t}}}) \epsilon^*_\lambda(\mathbf{k}) \tag{B.1a}$$

$$\mathcal{M}_{A2} = \overline{u}_r(\mathbf{p}_\mathrm{t}) \tilde{\mathcal{M}}_A \mathrm{i}\frac{-\mathbf{p}_\mathrm{t} - \mathbf{k} + m_\mathrm{t}}{2\mathbf{p}_{\bar{\mathrm{t}}}\cdot\mathbf{k}} \left(-\mathrm{i}\frac{2}{3}e\right) \Gamma^\lambda v_s(\mathbf{p}_{\bar{\mathrm{t}}}) \epsilon^*_\lambda(\mathbf{k}) \tag{B.1b}$$

$$\mathcal{M}_{B1} = \overline{u}_r(\mathbf{p}_\mathrm{t}) \left(-\mathrm{i}\frac{2}{3}e\right) \Gamma^\lambda \mathrm{i}\frac{\mathbf{p}_\mathrm{t} + \mathbf{k} + m_\mathrm{t}}{2\mathbf{p}_\mathrm{t}\cdot\mathbf{k}} \tilde{\mathcal{M}}_B(\mathbf{q}'_t) v_s(\mathbf{p}_{\bar{\mathrm{t}}}) \epsilon^*_\lambda(\mathbf{k}) \tag{B.1c}$$

$$\mathcal{M}_{B2} = \overline{u}_r(\mathbf{p}_\mathrm{t}) \tilde{\mathcal{M}}_B(\mathbf{q}_t) \mathrm{i}\frac{-\mathbf{p}_\mathrm{t} - \mathbf{k} + m_\mathrm{t}}{2\mathbf{p}_\mathrm{t}\cdot\mathbf{k}} \left(-\mathrm{i}\frac{2}{3}e\right) \Gamma^\lambda v_s(\mathbf{p}_{\bar{\mathrm{t}}}) \epsilon^*_\lambda(\mathbf{k}) \tag{B.1d}$$

$$\mathcal{M}_{B3} = \overline{u}_r(\mathbf{p}_\mathrm{t}) \mathrm{i}g_s \gamma^\mu (t^a)_{ec} \mathrm{i}\frac{\not{\mathbf{q}}_t + m_\mathrm{t}}{\mathbf{q}_t^2 - m_\mathrm{t}^2} \left(-\mathrm{i}\frac{2}{3}e\right) \Gamma^\lambda \mathrm{i}\frac{\not{\mathbf{q}}'_t + m_\mathrm{t}}{\mathbf{q}_t'^2 - m_\mathrm{t}^2} \mathrm{i}g_s \gamma^\nu (t^b)_{\bar{c}f} v_s(\mathbf{p}_{\bar{\mathrm{t}}}) \epsilon_{\mu,x}(\mathbf{p}_1) \epsilon_{\nu,y}(\mathbf{p}_2) \epsilon^*_\lambda(\mathbf{k}) \tag{B.1e}$$

$$\mathcal{M}_{C1} = \overline{u}_r(\mathbf{p}_\mathrm{t}) \left(-\mathrm{i}\frac{2}{3}e\right) \Gamma^\lambda \mathrm{i}\frac{\mathbf{p}_\mathrm{t} + \mathbf{k} + m_\mathrm{t}}{2\mathbf{p}_\mathrm{t}\cdot\mathbf{k}} \tilde{\mathcal{M}}_C(\mathbf{q}'_u) v_s(\mathbf{p}_{\bar{\mathrm{t}}}) \epsilon^*_\lambda(\mathbf{k}) \tag{B.1f}$$

$$\mathcal{M}_{C2} = \overline{u}_r(\mathbf{p}_\mathrm{t}) \tilde{\mathcal{M}}_C(\mathbf{q}_u) \mathrm{i}\frac{-\mathbf{p}_\mathrm{t} - \mathbf{k} + m_\mathrm{t}}{2\mathbf{p}_\mathrm{t}\cdot\mathbf{k}} \left(-\mathrm{i}\frac{2}{3}e\right) \Gamma^\lambda v_s(\mathbf{p}_{\bar{\mathrm{t}}}) \epsilon^*_\lambda(\mathbf{k}) \tag{B.1g}$$

$$\mathcal{M}_{C3} = \overline{u}_r(\mathbf{p}_\mathrm{t}) \mathrm{i}g_s \gamma^\nu (t^a)_{ec} \mathrm{i}\frac{\not{\mathbf{q}}_u + m_\mathrm{t}}{\mathbf{q}_u^2 - m_\mathrm{t}^2} \left(-\mathrm{i}\frac{2}{3}e\right) \Gamma^\lambda \mathrm{i}\frac{\not{\mathbf{q}}'_u + m_\mathrm{t}}{\mathbf{q}_u'^2 - m_\mathrm{t}^2} \mathrm{i}g_s \gamma^\mu (t^b)_{\bar{c}f} v_s(\mathbf{p}_{\bar{\mathrm{t}}}) \epsilon_{\mu,x}(\mathbf{p}_1) \epsilon_{\nu,y}(\mathbf{p}_2) \epsilon^*_\lambda(\mathbf{k}) \tag{B.1h}$$

$$\mathcal{M}_{D1/E1} = \overline{u}_r(\mathbf{p}_\mathrm{t}) \left(-\mathrm{i}\frac{2}{3}e\right) \Gamma^\lambda \mathrm{i}\frac{\mathbf{p}_\mathrm{t} + \mathbf{k} + m_\mathrm{t}}{2\mathbf{p}_\mathrm{t}\cdot\mathbf{k}} \tilde{\mathcal{M}}_{D/E} v_s(\mathbf{p}_{\bar{\mathrm{t}}}) \epsilon^*_\lambda(\mathbf{k}) \tag{B.1i}$$

$$\mathcal{M}_{D2/E2} = \overline{u}_r(\mathbf{p}_\mathrm{t}) \tilde{\mathcal{M}}_{D/E} \mathrm{i}\frac{-\mathbf{p}_\mathrm{t} - \mathbf{k} + m_\mathrm{t}}{2\mathbf{p}_\mathrm{t}\cdot\mathbf{k}} \left(-\mathrm{i}\frac{2}{3}e\right) \Gamma^\lambda v_s(\mathbf{p}_{\bar{\mathrm{t}}}) \epsilon^*_\lambda(\mathbf{k}) \tag{B.1j}$$

The abbreviations involved in the formulas above take the form:

$$\tilde{\mathcal{M}}_A = \mathrm{i}g_s\gamma^\kappa(t^{\tilde{c}})_{ef}g_s f^{abc}\left[g^{\mu\nu}(\mathbf{p}_1-\mathbf{p}_2)^\rho + g^{\nu\rho}(\mathbf{p}_2+\mathbf{q}_s)^\mu + g^{\rho\mu}(-\mathbf{q}_s-\mathbf{p}_1)^\nu\right] \mathrm{i}D_{\mathrm{F},\rho\kappa}(\mathbf{q}_s)\delta_{c,\tilde{c}}\epsilon_{\mu,x}(\mathbf{p}_1)\epsilon_{\nu,y}(\mathbf{p}_2) \tag{B.2a}$$

$$\tilde{\mathcal{M}}_B(\mathbf{q}) = \mathrm{i}g_s\gamma^\mu(t^a)_{ec}\mathrm{i}S_F(\mathbf{q})\delta_{c,\tilde{c}}\mathrm{i}g_s\gamma^\nu(t^b)_{\tilde{c}f}\epsilon_{\mu,x}(\mathbf{p}_1)\epsilon_{\nu,y}(\mathbf{p}_2) \tag{B.2b}$$

$$\tilde{\mathcal{M}}_C(\mathbf{q}) = \mathrm{i}g_s\gamma^\nu(t^b)_{ec}\mathrm{i}S_F(\mathbf{q}_u)\delta_{c,\tilde{c}}\mathrm{i}g\gamma^\mu(t^a)_{\tilde{c}f}\epsilon_{\mu,x}(\mathbf{p}_1)\epsilon_{\nu,y}(\mathbf{p}_2) \tag{B.2c}$$

$$\tilde{\mathcal{M}}_D = \mathrm{i}g_s\gamma^\nu(t^c)_{ef}\left(-g_s f^{abc}\mathbf{p}_1^\mu\right)\left(-\mathrm{i}\frac{g_{\mu\nu}}{\mathbf{q}_s^2}\delta_{c\tilde{c}}\right) \tag{B.2d}$$

$$\tilde{\mathcal{M}}_E = \mathrm{i}g_s\gamma^\nu(t^c)_{ef}\left(-g_s f^{abc}\mathbf{p}_2^\mu\right)\left(-\mathrm{i}\frac{g_{\mu\nu}}{\mathbf{q}_s^2}\delta_{c\tilde{c}}\right) \tag{B.2e}$$

Process $GG \to t\bar{t}Z$

The Feynman amplitudes for the process $GG \to t\bar{t}Z$ are similar to the ones for the process $GG \to t\bar{t}A$ except of two changes: The vertex prefactor $(-\mathrm{i}2/3e)$ is replaced in favor of $\mathrm{i}g/(2\cos\theta_\mathrm{W})$ and the term m_Z^2 is added in the denominator of the propagators $(\mathbf{p}_\mathrm{t}+\mathbf{k}+m_\mathrm{t})/(2\mathbf{p}_\mathrm{t}\cdot\mathbf{k})$ and $(-\mathbf{p}_\mathrm{t}-\mathbf{k}+m_\mathrm{t})/(2\mathbf{p}_{\bar{\mathrm{t}}}\cdot\mathbf{k})$.

C Further figures to chapter 8

C.1 Further figures to section 8.2

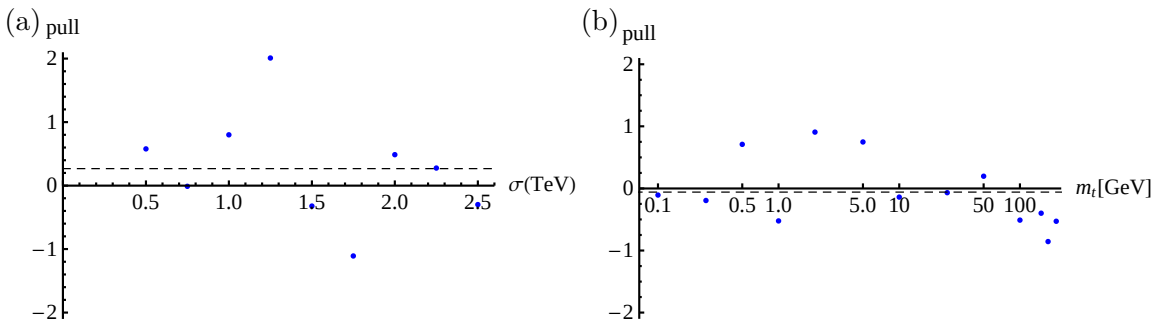

Figure C.1: Pull between the results of the semi-analytical calculation and the ones of WHIZARD for the cross-section for the process $GG \to t\bar{t}Z$ including a top quark width of $\Gamma_t = 1.523$ GeV. The physical polarization sum is used. Figure (a) shows the pull as a function of the center-of-mass energy $\sqrt{s}$ ($m_t = 172$ GeV), figure (b) as a function of the top quark mass m_t ($\sqrt{s} = 1.0$ TeV) . The straight dashed line indicates the mean in each plot.

C.2 Further figures to section 8.3

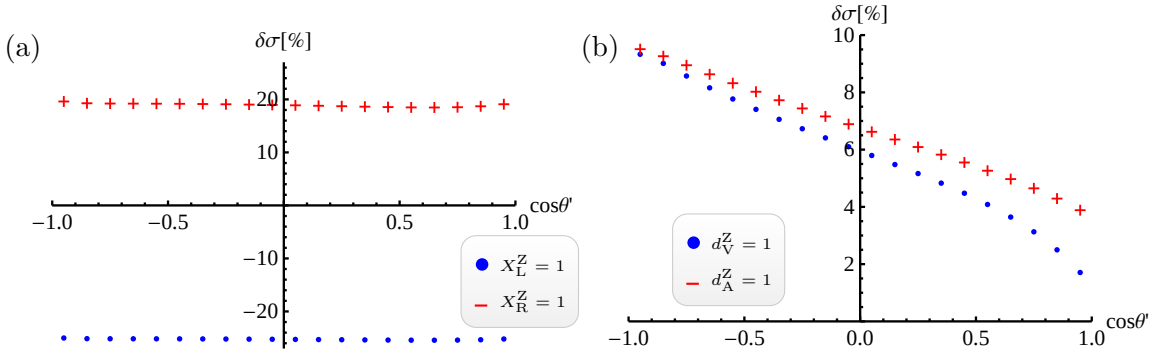

Figure C.2: Normalized deviation $\delta\sigma = (\sigma_{\text{anom.}} - \sigma_{\text{SM}})/\sigma_{\text{SM}}$ of the cross-section with anomalous couplings $\sigma_{\text{anom.}}$ from the SM cross-section σ_{SM} as a function of $\cos\theta'$ ($\sqrt{s} = 1.0$ TeV; $m_t = 172$ GeV). In figure (a) the results are shown for $X_L^Z = 1$ and $X_R^Z = 1$, in figure (b) for $d_V^Z = 1$ and $d_A^Z = 1$. The remaining parameters are set to their SM value.

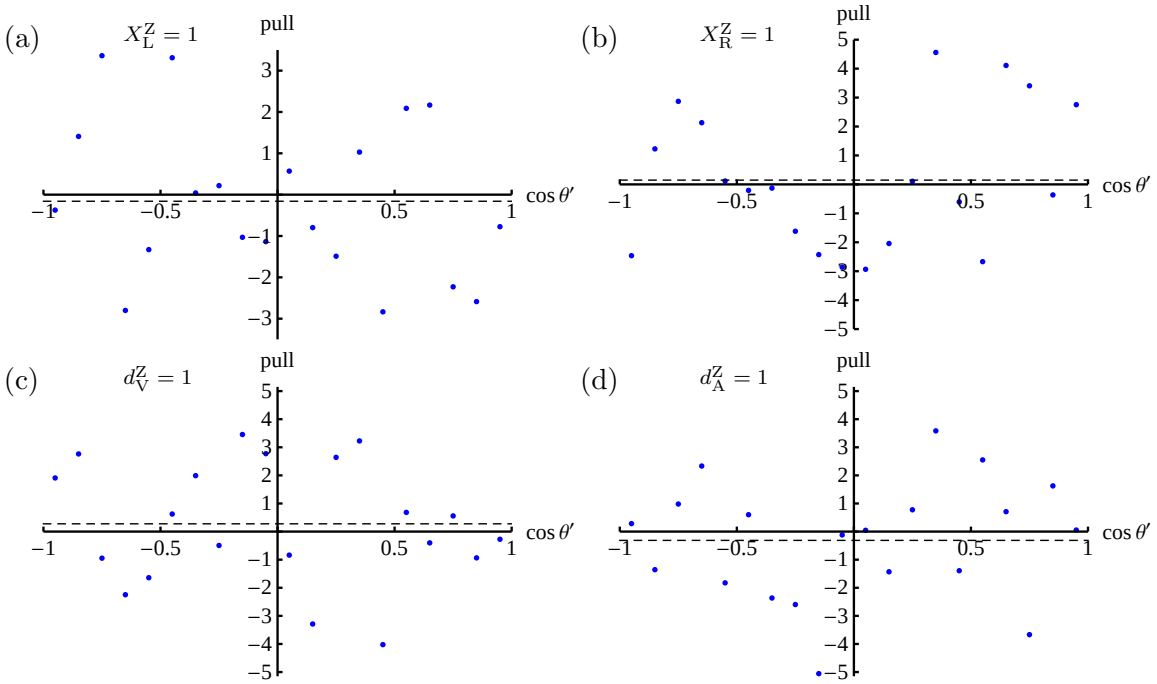

Figure C.3: Pull between the results of the semi-analytical calculation and the ones of WHIZARD for the cross-section as a function of $\cos\theta'$ for the process $GG \to t\bar{t}Z$ ($\sqrt{s} = 1.0$ TeV). Figure (a) shows the pull for $X_{\mathrm{L}}^{\mathrm{Z}} = 1$, figure (b) for $X_{\mathrm{R}}^{\mathrm{Z}} = 1$, figure (c) for $d_{\mathrm{V}}^{\mathrm{Z}} = 1$ and figure (d) for $d_{\mathrm{A}}^{\mathrm{Z}} = 1$ the remaining anomalous couplings vanishing. The straight dashed line indicates the mean in each plot.

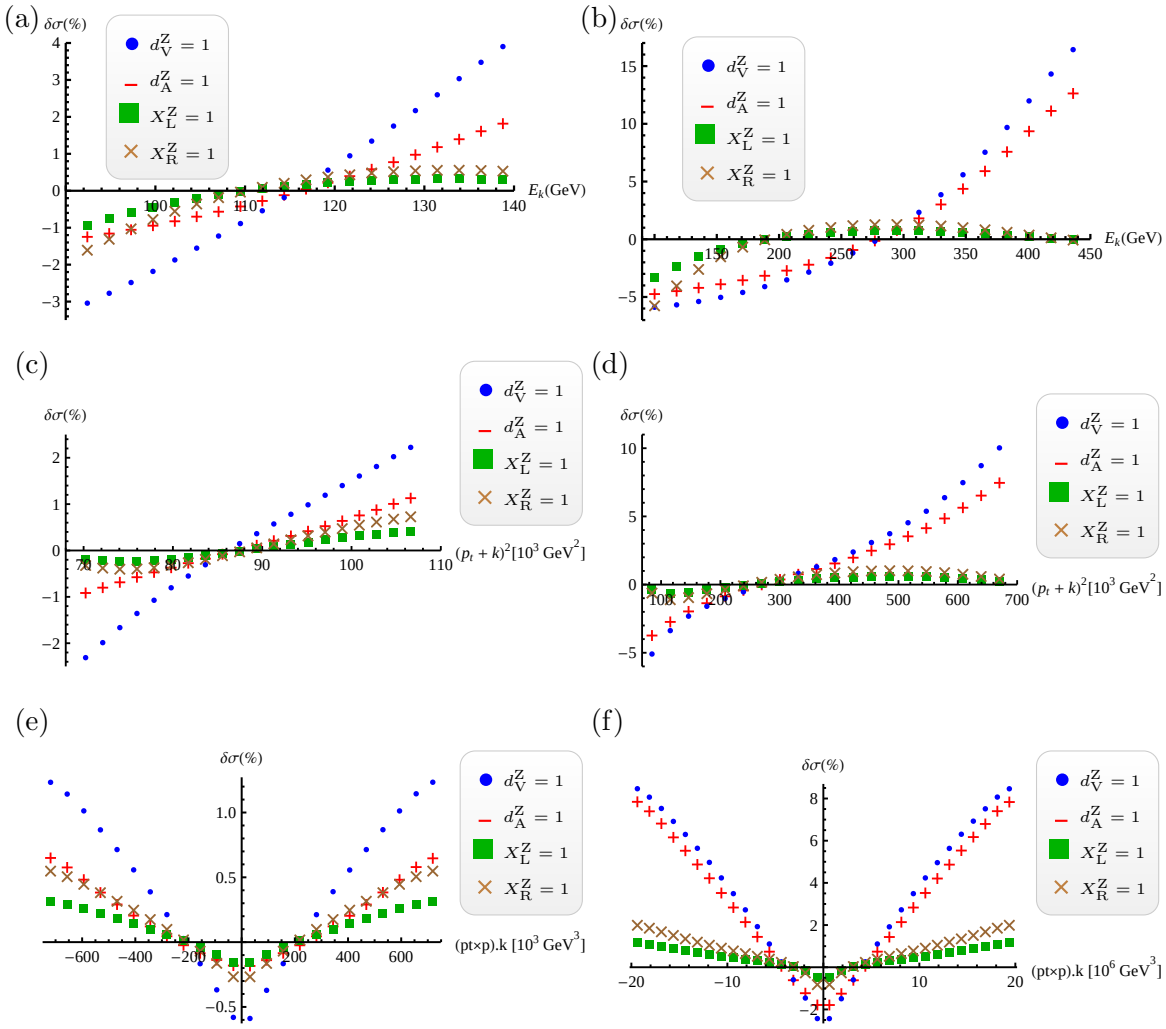

Figure C.4: Normalized deviation $\delta\sigma := (\sigma_{\text{anom.}} - \sigma_{\text{SM}})/\sigma_{\text{SM}}$ of the differential cross-section with anomalous couplings $\sigma_{\text{anom.}}$ from the SM differential cross-section σ_{SM}. Figures (a) and (b) show the dependence on the energy of the Z-boson E_{k}, figures (c) and (d) on the squared invariant mass $(\mathbf{p}_{\text{t}} + \mathbf{k})^2$ of the top quark and the Z-boson and figures (e) and (f) on value of the scalar triple product $(\mathbf{p}_{\text{t}} \times \mathbf{p}) \cdot \mathbf{k}$. For the figures on the left a center-of-mass energy of $\sqrt{s} = 0.5$ TeV is set, for the ones on the right a center-of-mass energy of $\sqrt{s} = 1.0$ TeV.

C.3 Further figures to section 8.4

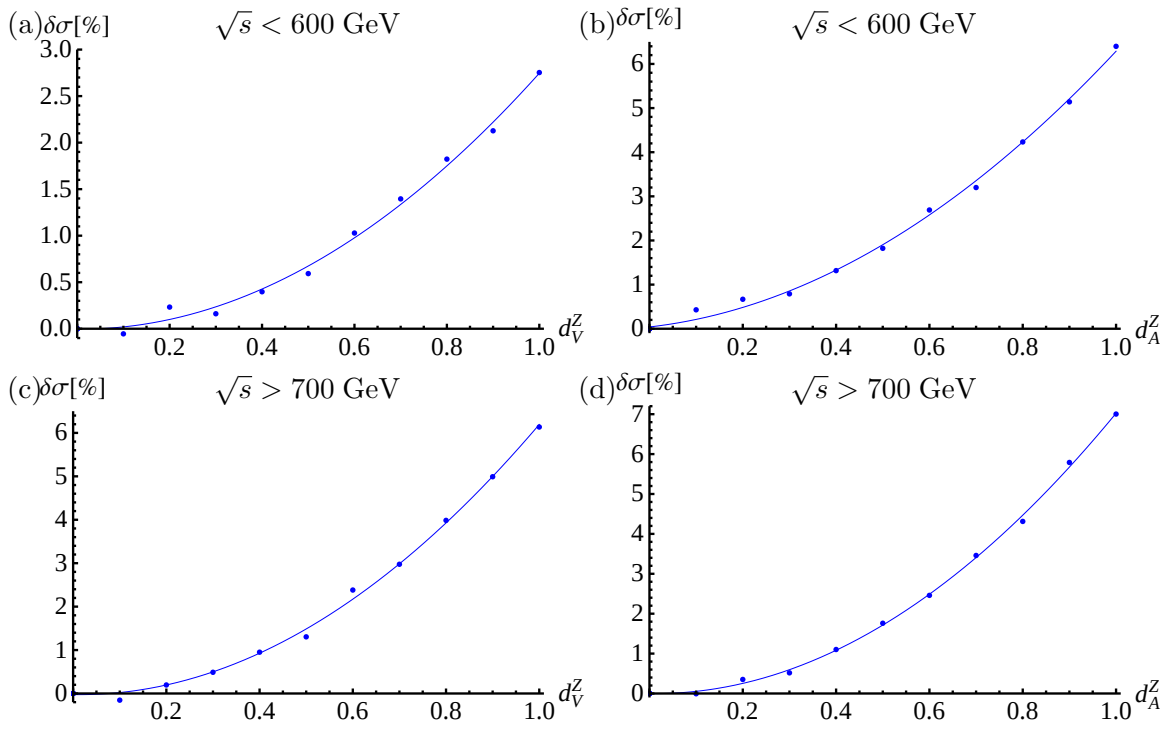

Figure C.5: Dependence of the normalized deviation $\delta\sigma = (\sigma_{\text{anom.}} - \sigma_{\text{SM}})/\sigma_{\text{SM}}$ on the anomalous couplings d_{V}^{Z} (on the left) and d_{A}^{Z} (on the right) ($\sqrt{\hat{s}}$ = 7.0 TeV; m_{t} = 172 GeV). Figures (a) and (b) show $\delta\sigma$ for the events with an invariant mass of the two top quarks and the Z-boson below 600 GeV, figures (c) and (d) for events with an invariant mass above 700 GeV. The points indicate the values obtained from the analysis of the Monte Carlo event samples, whereas the lines are fitted functions of the form $a\,(d_{\text{V/A}}^{\text{Z}})^2 + b\,d_{\text{V/A}}^{\text{Z}} + c$. The values of the fit parameters are: (a) (a = 2.78719; b = -0.0370364; c = -0.00448161), (b) (a = 5.04276; b = 1.20547; c = 0.0401432), (c) (a = 6.39835; b = -0.178967; c = -0.024608), (d) (a = 7.19022; b = -0.164657; c = -0.00173849)

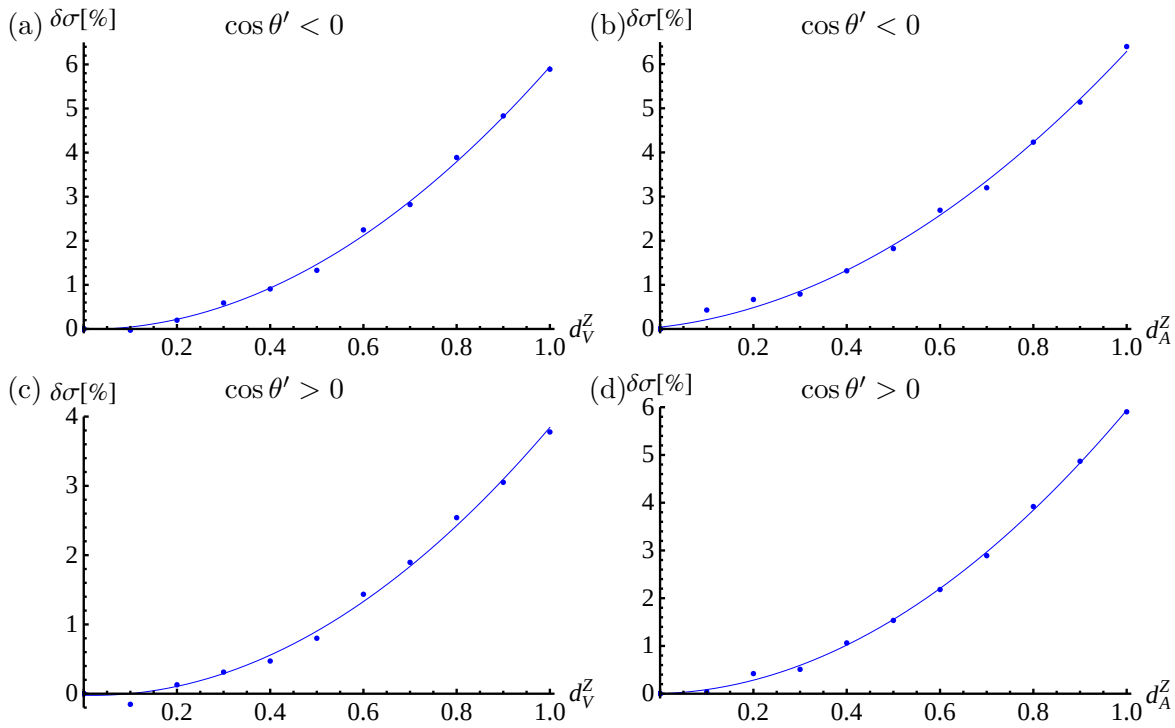

Figure C.6: Dependence of the normalized deviation $\delta\sigma = (\sigma_{\text{anom.}} - \sigma_{\text{SM}})/\sigma_{\text{SM}}$ on the anomalous couplings d_{V}^{Z} (on the left) and d_{A}^{Z} (on the right) ($\sqrt{\hat{s}}$ = 7.0 TeV; m_{t} = 172 GeV). Figures (a) and (b) show $\delta\sigma$ for the events with $\cos\theta' < 0$, figures (c) and (d) for events with $\cos\theta' > 0$. The points indicate the values obtained from the analysis of the Monte Carlo event samples, whereas the lines are fitted functions of the form $a\, {d_{\text{V/A}}^{\text{Z}}}^2 + b\, d_{\text{V/A}}^{\text{Z}} + c$. The values of the fit parameters are: (a) (a = 6.02063; b = -0.0633946; c = -0.0096642), (b) (a = 7.13633; b = 0.0606893; c = 0.00827197); (c) (a = 4.03352; b = -0.167153; c = -0.0217955), (d) (a = 5.65709; b = 0.27627; c = 0.00206206)

Bibliography

[1] CERN Press Office. The LHC is back, November 2009. Press release. Available from: http://press.web.cern.ch/press/PressReleases/Releases2009/PR16.09E.html.

[2] K. Aamodt et al. First proton-proton collisions at the LHC as observed with the ALICE detector: measurement of the charged-particle pseudorapidity density at $\sqrt{s} =$ 900 GeV. *The European Physical Journal C - Particles and Fields*, 65:111–125, 2010. arXiv:0911.5430v2, doi:10.1140/epjc/s10052-009-1227-4.

[3] CERN Press Office. LHC sets new record - accelerates beams to 3.5 TeV, March 2010. Press release. Available from: http://press.web.cern.ch/press/PressReleases/Releases2010/PR05.10E.html.

[4] The ATLAS Collaboration. ATLAS detector and physics performance: Technical Design Report, 2. Technical Report ATLAS TDR 15, CERN/LHCC 99-15, Geneva, 1999. Available from: http://cdsweb.cern.ch/record/391177.

[5] The ATLAS Collaboration, G. Aad, et al. Expected Performance of the ATLAS Experiment - Detector, Trigger and Physics. 2009. arXiv:0901.0512.

[6] The CMS Collaboration. CMS Physics Technical Design Report, Volume II: Physics Performance. *Journal of Physics G: Nuclear and Particle Physics*, 34(6):995, 2007. Available from: http://stacks.iop.org/0954-3899/34/i=6/a=S01.

[7] M. M. Najafabadi. Probing of Wtb anomalous couplings via the tW channel of single top production. *Journal of High Energy Physics*, 2008(03):024, 2008. arXiv:0801.1939, doi:10.1088/1126-6708/2008/03/024.

[8] S. Tsuno, I. Nakano, R. Tanaka, and Y. Sumino. Search for anomalous couplings in top decay at hadron colliders. *Phys. Rev. D*, 73(5):054011, Mar 2006. arXiv:hep-ex/0512037, doi:10.1103/PhysRevD.73.054011.

[9] V. M. Abazov et al. Search for Anomalous Top-Quark Couplings with the D0 Detector. *Phys. Rev. Lett.*, 102(9):092002, Mar 2009. arXiv:0901.0151, doi:10.1103/PhysRevLett.102.092002.

[10] E. Devetak and A. Nomerotski. Top quark anomalous couplings at the International Linear Collider. 2010. arXiv:1005.1756.

[11] T. G. Rizzo. Constraints on Anomalous Top Quark Couplings at the LHC. 1996. SLAC-PUB-7294. arXiv:hep-ph/9609311.

[12] Z. Hioki and K. Ohkuma. Search for anomalous top-gluon couplings at LHC revisited. *The European Physical Journal C - Particles and Fields*, 65:127–135, 2010. arXiv:0910.3049, doi:10.1140/epjc/s10052-009-1204-y.

[13] T. Sjöstrand, S. Mrenna, and P. Skands. PYTHIA 6.4 physics and manual. *Journal of High Energy Physics*, 2006(05):026, 2006. arXiv:hep-ph/0603175, doi:10.1088/1126-6708/2006/05/026.

[14] G. Corcella et al. HERWIG 6: an event generator for hadron emission reactions with interfering gluons (including supersymmetric processes). *Journal of High Energy Physics*, 2001(01):010, 2001. arXiv:hep-ph/0011363v3.

[15] J. Alwall et al. MadGraph/MadEvent v4: the new web generation. *Journal of High Energy Physics*, 2007(09):028, 2007. arXiv:0706.2334, doi:10.1088/1126-6708/2007/09/028.

[16] E. Boos et al. CompHEP 4.4–automatic computations from Lagrangians to events. *Nuclear Instruments and Methods in Physics Research Section A*, 534(1-2):250 – 259, 2004. arXiv:hep-ph/0403113, doi:10.1016/j.nima.2004.07.096.

[17] A. Pukhov. CalcHEP 2.3: MSSM, structure functions, event generation, batchs, and generation of matrix elements for other packages. 2004. arXiv:hep-ph/0412191.

[18] T. Gleisberg et al. SHERPA 1.α, a proof-of-concept version. *Journal of High Energy Physics*, 2004(02):056, 2004. arXiv:hep-ph/0311263, doi:10.1088/1126-6708/2004/02/056.

[19] W. Kilian, T. Ohl, and J. Reuter. WHIZARD: Simulating Multi-Particle Processes at LHC and ILC. 2007. Available from: http://projects.hepforge.org/whizard/, arXiv:0708.4233.

[20] F. Abe et al. Observation of Top Quark Production in $p\bar{p}$ Collisions with the Collider Detector at Fermilab. *Phys. Rev. Lett.*, 74(14):2626–2631, Apr 1995. arXiv:hep-ex/9503002v2, doi:10.1103/PhysRevLett.74.2626.

[21] S. Abachi et al. Search for High Mass Top Quark Production in $p\bar{p}$ Collisions at $\sqrt{s} =$ 1.8 TeV. *Phys. Rev. Lett.*, 74(13):2422–2426, Mar 1995. arXiv:hep-ex/9411001v1, doi:10.1103/PhysRevLett.74.2422.

[22] K. Nakamura and Particle Data Group. Review of Particle Physics. *Journal of Physics G: Nuclear and Particle Physics*, 37(7A):075021, 2010. Available from: http://stacks.iop.org/0954-3899/37/i=7A/a=075021.

[23] A. Strässner. Status of ATLAS and Expectations for First Physics At The LHC. Technical Report ATL-GEN-PROC-2009-001. ATL-COM-GEN-2008-016, CERN, Geneva, Dec 2008. Available from: http://cdsweb.cern.ch/record/1144067.

[24] D. Chang, We-Fu Chang, and E. Ma. Alternative interpretation of the Fermilab Tevatron top events. *Phys. Rev. D*, 59(9):091503, Apr 1999. arXiv:hep-ph/9810531v2, doi:10.1103/PhysRevD.59.091503.

[25] CDF Collaboration, editor. *Exclusion of Exotic Top-like Quark with -4/3 Electric Charge Using Soft Lepton Tags*, number 9939, 2010. CDF note 9939. Available from: http://www-cdf.fnal.gov/physics/new/top/confNotes/cdf9939_topq_public.pdf.

[26] V. M. Abazov et al. Experimental Discrimination between Charge $2e/3$ Top Quark and Charge $4e/3$ Exotic Quark Production Scenarios. *Phys. Rev. Lett.*, 98(4):041801, Jan 2007. FERMILAB-PUB-06/278-E. arXiv:hep-ex/0608044v2, doi:10.1103/PhysRevLett.98.041801.

[27] W. Bernreuther. Top-quark physics at the LHC. *Journal of Physics G: Nuclear and Particle Physics*, 35(8):083001, 2008. arXiv:0805.1333v1, doi:10.1088/0954-3899/35/8/083001.

[28] R. Bonciani, S. Catani, M. L. Mangano, and P. Nason. NLL resummation of the heavy-quark hadroproduction cross-section. *Nuclear Physics B*, 529(1-2):424 – 450, 1998. arXiv:hep-ph/9801375v2, doi:10.1016/S0550-3213(98)00335-6.

[29] W. Buchmüller and D. Wyler. Effective lagrangian analysis of new interactions and flavour conservation. *Nuclear Physics B*, 268(3-4):621 – 653, 1986. doi:10.1016/0550-3213(86)90262-2.

[30] H. Georgi. On-shell effective field theory. *Nuclear Physics B*, 361(2):339 – 350, 1991. doi:10.1016/0550-3213(91)90244-R.

[31] J.A. Aguilar-Saavedra. A minimal set of top anomalous couplings. *Nuclear Physics B*, 812(1-2):181 – 204, 2009. arXiv:0811.3842, doi:10.1016/j.nuclphysb.2008.12.012.

[32] C. Arzt. Reduced effective lagrangians. *Physics Letters B*, 342(1-4):189 – 195, 1995. arXiv:hep-ph/9304230, doi:10.1016/0370-2693(94)01419-D.

[33] A. Salam and J. Strathdee. Equivalent Formulations of Massive Vector Field Theories. *Phys. Rev. D*, 2(12):2869–2876, Dec 1970. doi:10.1103/PhysRevD.2.2869.

[34] T. Ohl. O'Mega: An optimizing matrix element generator. *AIP Conference Proceedings*, 583(1):173–175, 2001. arXiv:hep-ph/0011243v1, doi:10.1063/1.1405295.

[35] T. Ohl. Vegas revisited: Adaptive Monte Carlo integration beyond factorization. *Computer Physics Communications*, 120(1):13 – 19, 1999. arXiv:hep-ph/9806432, doi:10.1016/S0010-4655(99)00209-X.

[36] M. R. Whalley, D. Bourilkov, and R. C. Group. The Les Houches Accord PDFs (LHAPDF) and Lhaglue. 2005. arXiv:hep-ph/0508110.

[37] T. Ohl. CIRCE Version 1.0: Beam Spectra for Linear Collider Physics. *Computer Physics Communications*, 101(3):269 – 288, 1997. arXiv:hep-ph/9607454, doi:10.1016/S0010-4655(96)00167-1.

[38] G. P. Lepage. A new algorithm for adaptive multidimensional integration. *Journal of Computational Physics*, 27(2):192 – 203, 1978. doi:10.1016/0021-9991(78)90004-9.

[39] G. P. Lepage. VEGAS: An Adaptive Multidimensional Integration Program. *Cornell preprint*. CLNS-80/447.

[40] J. H. Friedman and M. H. Wright. A Nested Partitioning Procedure for Numerical Multiple Integration. *ACM Trans. Math. Softw.*, 7(1):76–92, 1981. doi:10.1145/355934.355939.

[41] T. Hahn. Cuba–a library for multidimensional numerical integration. *Computer Physics Communications*, 168(2):78 – 95, 2005. arXiv:hep-ph/0404043, doi:10.1016/j.cpc.2005.01.010.

[42] R. Kleiss and R. Pittau. Weight optimization in multichannel Monte Carlo. *Computer Physics Communications*, 83(2-3):141 – 146, 1994. arXiv:hep-ph/9405257, doi:10.1016/0010-4655(94)90043-4.

[43] J. C. Collins, D. E. Soper, and G. F. Sterman. Factorization of Hard Processes in QCD. *Adv. Ser. Direct. High Energy Phys.*, 5:1–91, 1988. arXiv:hep-ph/0409313.

[44] M. E. Peskin and D. V. Schroeder. *An Introduction to Quantum Field Theory*. Westview Press, 1995.

[45] C.-H. Chou, H.-H. Shih, S.-C. Lee, and H.-nan Li. $\Lambda_b \to \Lambda J/\psi$ decay in perturbative QCD. *Phys. Rev. D*, 65(7):074030, Apr 2002. arXiv:hep-ph/0112145v1, doi:10.1103/PhysRevD.65.074030.

[46] W. Wagner. Top quark physics in hadron collisions. *Reports on Progress in Physics*, 68(10):2409, 2005. arXiv:hep-ph/0507207v2.

[47] R. Mertig, M. Böhm, and A. Denner. Feyn Calc - Computer-algebraic calculation of Feynman amplitudes. *Computer Physics Communications*, 64(3):345 – 359, 1991. doi:10.1016/0010-4655(91)90130-D.

[48] S. Wolfram. *Mathematica - A System for Doing Mathematics by Computer*. Addison-Wesley, Reading, MA, 1988.

[49] J. C. Ward. An identity in quantum electrodynamics. *Phys. Rev.*, 78(2):182, Apr 1950. doi:10.1103/PhysRev.78.182.

[50] E. Byckling and K. Kajantie. *Particle Kinematics*. Wiley, London, 1973.

[51] J. Pumplin et al. New Generation of Parton Distributions with Uncertainties from Global QCD Analysis. *Journal of High Energy Physics*, 2002(07):012, 2002. arXiv:hep-ph/0201195, doi:10.1088/1126-6708/2002/07/012.

[52] W. Mendenhall and R. J. Beaver. *Introduction to probability and statistics*. PWS-Kent Publ., Boston, Mass., 8th edition, 1991.

[53] J. Hartung, B. Elpelt, and K.-H. Klösener. *Statistik*. Oldenbourg, München, 14th edition, 2005.

[54] R. Mohr. *Statistik für Ingenieure und Naturwissenschaftler*. expert-Verlag, Renningen, 2nd edition, 2008.

Acknowledgments

I would like to thank ...

- Prof. Dr. Thorsten Ohl for the opportunity to write my thesis on an interesting topic in his group. I am deeply grateful for helpful discussions and support both regarding physics topics and the application process for my PhD position.
- Prof. Dr. Reinhold Rückl for the opportunity to write my thesis in the TPII department.
- the members of my work group Dominika Konikowska, Alexander Schenkel, Christoph Uhlemann, Felix Keller, Fabian Bach and Christian Speckner for standing my concerns in the group meetings and helpful discussions.
- my office colleagues ...
  ... Lisa Edelhäuser por hacer compañía amable y encantarme con conversaciones divertidas tanto en alemán como español. ¡Que tengas un tiempo estupendo!
  ... Daniel Gerstenlauer for bearing nice company and amusing conversations. Remember that, if we should not become successful scientists, we could always find a job as germanists ;-)
  ... Christian Speckner for helping me with computer issues in the early stage of my thesis.
- my fellow students, especially Martin Krauß and Rolf Reinthaler, for nice company, diverting afternoon breaks and the weekly (at least for one of the two ;-)) swimming.
- my parents for their unlimited support during my studies. Special thanks are also addressed at my sisters (Best wishes to you, little Stefan!).

Eidesstattliche Erklärung

Gemäß §21 Absatz 10 der allgemeinen Studien- und Prüfungsordung für die Bachelor- und Masterstudiengänge an der Julius-Maximilians-Universität Würzburg erkläre ich hiermit, dass ich diese Arbeit selbstständig verfasst, keine anderen als die angegebenen Quellen und Hilfsmittel benutzt habe und die Arbeit bisher oder gleichzeitig keiner anderen Prüfungsbehörde unter Erlangung eines akademischen Grades vorgelegt habe.

Würzburg, den 13. Oktober 2010

Klaus Klopfer